Mitotic CDK Promotes Replisome Disassembly, Fork Breakage, and Complex DNA Rearrangements

Deng, Lin; Wu, R. Alex; Sonneville, Remi; Kochenova, Olga V.; Labib, Karim; Pellman, David

Published in:
Molecular Cell

DOI:
10.1016/j.molcel.2018.12.021

Publication date:
2019

Mitotic CDK promotes replisome disassembly, fork breakage, and complex DNA rearrangements

Lin Deng[1,2,3], R. Alex. Wu[3], Remi Sonneville[4], Olga V. Kochenova[3], Karim Labib[4], David Pellman[1,2,5,6,7], and Johannes C. Walter[3,6,7,8]

[1]Department of Pediatric Oncology, Dana-Farber Cancer Institute, Boston, MA 02215, USA

[2]Department of Cell Biology, Harvard Medical School, Boston, MA 02115, USA

[3]Department of Biological Chemistry and Molecular Pharmacology, Harvard Medical School, Boston, MA 02115, USA

[4]MRC Protein Phosphorylation and Ubiquitylation Unit, Sir James Black Centre, School of Life Sciences, University of Dundee, Dow Street, Dundee DD1 5EH, UK

[5]Broad Institute of MIT and Harvard, Cambridge, MA 02142, USA

[6]Howard Hughes Medical Institute, Boston, MA 02115, USA

[7]These authors contributed equally to this work

[8]Lead Contact

*Correspondence: David_Pellman@dfci.harvard.edu (D.P.), Johannes_Walter@hms.harvard.edu (J.C.W.)

Summary

DNA replication errors generate complex chromosomal rearrangements and thereby contribute to tumorigenesis and other human diseases. One mechanism that triggers these errors is mitotic entry before the completion of DNA replication. To address how mitosis impacts DNA replication, we used *Xenopus* egg extracts. When mitotic CDK (Cyclin B1-CDK1) is used to drive these extracts into a mitotic state, the replicative CMG (CDC45/MCM2-7/GINS) helicase undergoes ubiquitylation on its MCM7 subunit, dependent on the E3 ubiquitin ligase TRAIP. Whether replisomes have stalled or undergone termination, CMG ubiquitylation is followed by its extraction from chromatin by the CDC48/p97 ATPase. TRAIP-dependent CMG unloading during mitosis is also seen in *C. elegans* early embryos. At stalled forks, CMG removal results in fork breakage and end joining events involving deletions and templated insertions. Our results identify a novel pathway of global replisome disassembly in mitosis that can trigger replication fork collapse and DNA rearrangements.

HIGHLIGHTS

1. Replication fork collapse is triggered by mitotic CDK-dependent CMG unloading
2. Unloading of CMGs in mitosis involves the E3 ubiquitin ligase TRAIP and the p97 ATPase
3. New model for the mitotic processing of stalled forks that enables high-fidelity chromosome segregation
4. New model for the generation of complex chromosome rearrangements

INTRODUCTION

Genome evolution occurs through the gradual accrual of genetic changes or in a saltatory manner, with bursts of chromosomal alterations originating from single catastrophic events (Holland and Cleveland, 2012; Leibowitz et al., 2015; Liu et al., 2011; Stephens et al., 2011). Many chromosomal alterations can be traced to DNA breaks that arise during DNA replication (Hills and Diffley, 2014; Mankouri et al., 2013; Techer et al., 2017). However, there is an ongoing debate about when and how replication fork breakage is triggered (Toledo et al., 2017).

In normal cells, multiple cell cycle regulatory controls and error correction mechanisms prevent DNA replication errors (Hills and Diffley, 2014). Cells prepare for DNA replication in the G1 phase of the cell cycle, when pairs of MCM2-7 ATPases are recruited to each origin ("licensing"). In S phase, cyclin-dependent kinase (CDK) promotes the association of CDC45 and GINS with MCM2-7, leading to formation of the replicative CMG helicase complex (CDC45-MCM2-7-GINS) ("initiation"). CMG unwinding of the origin nucleates the assembly of two DNA replication forks that travel away from the origin, copying DNA as they go ("elongation"). When converging forks from adjacent origins meet, the replisome is disassembled ("termination"). Replisome disassembly during S phase in metazoa requires the E3 ubiquitin ligase, $CRL2^{Lrr1}$, which ubiquitylates the MCM7 subunit of CMG, leading to CMG's extraction from chromatin by the p97 ATPase (Dewar et al., 2017; Sonneville et al., 2017). In the absence of $CRL2^{Lrr1}$, CMGs persist on chromatin until mitosis, but are then removed by a secondary, p97-dependent pathway that is controlled by an unknown E3 ubiquitin ligase (Sonneville et al., 2017). Re-replication is inhibited because *de novo* licensing of origins is suppressed in the S and G2 phases of the cell cycle. Thus, faithful DNA

replication requires the seamless integration of replication licensing, initiation, elongation, and termination. Errors in the process are detected by the DNA damage response, which activates repair mechanisms and prevents entry into mitosis in the setting of incomplete or abnormal replication.

DNA replication forks become stressed in a variety of circumstances, including the activation of oncogenes, collision with DNA lesions and other obstacles, and nucleotide starvation (Cortez, 2015; Hills and Diffley, 2014; Saldivar et al., 2017). Replication stress, especially when combined with inhibition of checkpoint kinases, can cause replication fork “collapse”, an irreversible state from which replication cannot be restarted (Cortez, 2015; Hills and Diffley, 2014; Pasero and Vindigni, 2017; Saldivar et al., 2017; Toledo et al., 2017). Despite its central importance to the maintenance of genome stability, much remains to be learned about the mechanisms leading to replication fork collapse and the relationship between fork collapse and breakage. Whether “fork collapse” occurs through multiple independent mechanisms or whether different insults converge on a single irreversible event is not clear. Numerous experiments indicated that fork collapse involves replisome disassembly—an appealing mechanism to explain the irreversibility of “collapse” (Cortez, 2015). However, these studies did not establish a causal relationship between replisome disassembly and collapse. Moreover, some experiments suggest that fork collapse may not involve replisome disassembly (De Piccoli et al., 2012; Dungrawala et al., 2015).

Replication fork collapse is strongly enhanced by inhibition of the checkpoint kinase ataxia telangiectasia and RAD3 related (ATR), a phenomenon for which there are multiple proposed mechanisms (Toledo et al., 2017). ATR may stabilize stressed

93 forks through the phosphorylation of specific proteins at the fork (e.g. SMARCAL1,
94 WRN). However, the available evidence suggests that these phosphorylation events are
95 not sufficient to explain ATR-mediated fork stabilization (Ammazzalorso et al., 2010;
96 Couch et al., 2013). A further possibility is that excessive origin firing upon ATR
97 inhibition leads to exhaustion of the nuclear pool of RPA, followed by fork breakage and
98 replisome collapse (Toledo et al., 2013). Finally, ATR might prevent fork collapse by
99 restraining the activation of mitotic kinases such as CDK1 and PLK1 until the
100 completion of replication (Ragland et al., 2013; Saldivar et al., 2018). Mitotic kinases
101 induce fork breakage by promoting the assembly of a MUS81-containing nuclease
102 complex (Duda et al., 2016) or by triggering nuclear envelope breakdown, exposes
103 replication forks to the normally cytoplasmic GEN1 nuclease (West and Chan, 2018). A
104 key role for ATR in restraining mitotic kinases is underscored by recent studies. First,
105 the lethality of ATR inhibition in mammals can be overcome by suppressing Cyclin B-
106 CDK1 activity (Ruiz et al., 2016). Second, even in the absence of exogenous stress,
107 ATR suppresses genome instability by preventing premature accumulation of Cyclin B-
108 CDK1 activity in S phase (Saldivar et al., 2018). Despite this progress, the molecular
109 basis of replication fork collapse and how this process is regulated by ATR remain
110 incompletely understood.

111 Although replication fork breakage is generally viewed as a source of gross
112 chromosomal rearrangements, there are circumstances in which breakage may
113 preserve genome integrity (Bhowmick and Hickson, 2017). A prominent example
114 involves common fragile sites (CFS), which are among the most frequently rearranged
115 genomic loci in cancer genomes (Glover et al., 2017). CFS are difficult to replicate

because they either contain large genes with long transcripts and/or have few origins of replication (Glover et al., 2017). Common fragile site “expression,” the appearance of cytologically visible breaks and gaps, is promoted by low doses of aphidicolin because this drug delays duplication of these already late-replicating loci. Unreplicated DNA at CFS forms ultrafine DNA bridges between anaphase chromosomes (Baumann et al., 2007; Chan et al., 2007), and severance of these bridges by MUS81 is thought to allow chromosome segregation. Aberrant processing of expressed CFS leads to the formation of “53BP1 bodies” (Naim et al., 2013; Ying et al., 2013), structures thought to protect damaged DNA in the next interphase (Harrigan et al., 2011; Lukas et al., 2011). Collectively, the data suggest that when cells enter mitosis with incompletely replicated DNA, MUS81 breakage of stalled replication forks enables chromosome segregation. However, random breakage of the fork would yield deleterious outcomes such as the generation of acentric or iso-chromosomes. So far, no mechanism has emerged that explains how such outcomes are avoided.

Although breakage of a few stressed forks may be be beneficial, concurrent breakage of many forks generates catastrophic chromosomal rearrangements. Several lines of evidence implicate mitotic entry as one potential cause of extensive fork breakage. Cell fusion experiments (Johnson and Rao, 1970) and experiments on cells with micronuclei (Kato and Sandberg, 1968) showed that S phase chromosomes undergo “pulverization” upon exposure to mitotic cytoplasm. Although there was early disagreement about whether chromosome pulverization reflects discontinuous condensation or actual DNA breakage (Rao et al., 1982), recent work indicates that fragmentation does occur. First, premature mitotic entry triggered by inhibition of the

WEE1 kinase causes extensive fork breakage in a manner that depends on the formation of an active MUS81 complex (Dominguez-Kelly et al., 2011; Duda et al., 2016). Second, chromothripsis, a mutational process involving extensive chromosome fragmentation and rearrangement, may involve entry into mitosis of micronuclei undergoing DNA replication (Crasta et al., 2012; Leibowitz et al., 2015). Extensive fork breakage during mitosis is especially problematic as both homologous recombination and classical non-homologous end joining are suppressed at this stage of the cell cycle (Hustedt and Durocher, 2016). In summary, it has become apparent that genome instability in a variety of contexts is linked to mitotic replication fork breakage. However, why forks are so fragile in mitosis is incompletely understood.

Here, we used *Xenopus* egg extracts to explore the relationship between DNA replication and mitosis. We find that in egg extracts supplemented with the mitotic kinase Cyclin B1-CDK1, the CMG helicase is ubiquitylated on its MCM7 subunit. Ubiquitylation requires the RING E3 ubiquitin ligase TRAIP, which is mutated in primordial dwarfism. Ubiquitylated CMG is subsequently extracted from chromatin by the CDC48/p97 ATPase. TRAIP-dependent CMG ubiquitylation and unloading is observed at stalled replisomes and replisomes that have undergone termination, indicating that TRAIP removes all CMGs from chromatin, regardless of their configuration on DNA. At stalled forks, CMG unloading leads to fork breakage and end joining events that likely involve DNA polymerase θ (Polθ). Unlike Cyclin B1-CDK1 treatment, ATR inhibition does not lead to fork breakage. Together, our results identify TRAIP-dependent replisome disassembly as a crucial step in mitotic replication fork collapse and breakage. We propose that breakage of a few converging forks (e.g. at

CFS) that have failed to complete DNA synthesis before mitosis helps to maintain chromosome integrity whereas breakage of many forks (e.g. in micronuclei) leads to catastrophic genomic instability.

RESULTS

Mitotic CDK triggers aberrant processing of stressed DNA replication forks

To examine the effect of mitotic CDK on DNA replication and fork stability, we used *Xenopus* egg extracts, which can recapitulate S phase or mitosis. For S phase, plasmid DNA was first incubated in a high-speed supernatant (HSS) of *Xenopus* egg lysate. HSS promotes the assembly onto DNA of pre-replication complexes (pre-RCs) containing double hexamers of the MCM2-7 ATPase (Figure 1A). The subsequent addition of a nucleoplasmic extract (NPE) leads to the association of CDC45 and GINS with each MCM2-7 hexamer to form two active CMG DNA helicases, which unwind DNA, promoting a single, complete round of DNA replication, manifested as the appearance of supercoiled (SC) daughter molecules (Figure 1B, lanes 1-6) (Walter et al., 1998). To achieve replication in a mitotic state, we added Cyclin B1-CDK1 (B1-CDK1) after pre-RC formation because this kinase inhibits licensing (Hendrickson et al., 1996; Prokhorova et al., 2003)(Figure 1A). We confirmed that B1-CDK1 induced chromosome condensation (Figures S1A-S1C) and condensin recruitment (Figures S1D-E). As we showed previously (Prokhorova et al., 2003), B1-CDK1 increased the rate of DNA replication in NPE (Figure 1B, compare lanes 1-6 and 13-18), due in part to increased origin firing (Figure S1F). However, in the absence of other perturbations, all

replication products were open circular or supercoiled species (Figure 1B, lanes 13-18), indicating that B1-CDK1-induced chromatin condensation does not cause aberrant DNA replication.

Given the evidence that stressed DNA replication forks undergo breakage during mitosis (e.g. at common fragile sites, see introduction), we added a low concentration of the replicative DNA polymerase inhibitor aphidicolin (APH; 2.2 μM) to slow fork progression (Figure 1B, lanes 7-12). Interestingly, the combination of B1-CDK1 and APH (Figure 1B, lanes 19-24) led to the appearance of a new replication product that migrated at the very top of the gel. This aberrant replication product (ARP) comprised ~6% of total replication for a 3 kb plasmid and up to 30% for a 9 kb plasmid (data not shown), presumably because the larger plasmid hosts more replication forks. ARPs recovered from extract were not resolved by Topoisomerase I or Topoisomerase II treatment, indicating they are not plasmid topoisomers (data not shown). Thus, in the presence of replication stress, mitotic CDK induces aberrant DNA replication.

To examine the effect of B1-CDK1 on replication forks that have stalled at a defined location, we replicated a plasmid containing an array of 48 *lacO* sites (p[$lacO_{48}$]) bound by the *lac* repressor (LacR) (Figure 1C). As expected (Dewar et al., 2015), replication forks stalled at the outer edges of the LacR array, generating a “theta” (θ) structure (Figures 1C and 1D, lanes 11-15). In the presence of B1-CDK1, the theta molecules disappeared and ARPs accumulated (Figure 1D, lanes 16-20). ARPs were not generated when LacR-mediated fork stalling was prevented with IPTG (Figure 1E), or in the presence of the CDK1 inhibitor (CDK1-i) RO-3306 (Figure S1G). Furthermore, addition of Cyclin E-CDK2 or Cyclin A2 (which preferentially associates with

endogenous CDK1; (Strausfeld et al., 1996)), did not strongly induce ARPs, although their addition accelerated DNA replication as expected (Figure S1H). Second, we induced replication fork stalling with covalent DNA-protein crosslinks (DPCs). We replicated a plasmid substrate (pDPC), which contains two site-specific DPCs on each leading strand template (Figure 1F). As expected (Duxin et al., 2014), in the absence of B1-CDK1, replication of pDPC first yielded theta structures when forks transiently paused at the DPC. Plasmids then resolved into open circular (OC) species that persisted due to slow translesion synthesis past the peptide adduct generated by DPC proteolysis (Figure 1F, upper arrow and Figure 1G, lanes 13-18). In the presence of B1-CDK1, we again observed a substantial accumulation of ARPs (Figure 1G, lanes 19-24). In summary, mitotic CDK caused aberrant processing of replication forks stalled by aphidicolin, non-covalent nucleoprotein complexes, and DPCs.

Mitotic processing of stalled replication forks leads to complex chromosomal rearrangements

To determine the structure of mitotic ARPs, we replicated the 4.6 kb LacR plasmid in the presence and absence of B1-CDK1 and digested the replication products with AlwNI and AflII, which cuts the plasmid into a 1.9 kb fragment and a 2.7 kb fragment encompassing the *lacO* repeats (Figure 2A). In the absence of B1-CDK1, fully replicated 1.9 kb fragments quickly accumulated, whereas the rest of the plasmid migrated as a double-Y structure that gradually increased in size due to slow progression of forks through the LacR array (Figure 2B, middle panel, lanes 1-7 and Figure 2C, “Buffer”; (Dewar et al., 2015)). In the presence of B1-CDK1, the 1.9 kb

fragment again accumulated quickly and persisted, demonstrating that this *lacO*-free region was replicated efficiently (Figure 2B, middle panel, lanes 8-14). However, the double-Y structure containing the *lacO* array rapidly disappeared. Thus, in the presence of B1-CDK1, aberrant DNA processing occurs specifically on molecules containing stalled forks.

When the replication products were digested only with AlwNI, we observed B1-CDK1-dependent disappearance of the now larger double-Y structure (Figure 2B, bottom panel, lanes 8-14). In addition, we detected a new series of species migrating between ~3 and ~4 kb (Figure 2B, bottom panel; smear). We hypothesized that when replication forks enter the array and slow down or stall, B1-CDK1 promotes their collapse and breakage. The resulting double-strand breaks (DSBs) subsequently undergo joining with DSBs from broken forks on other plasmids, generating ARPs (Figures 2C, “B1-CDK1” and S2A). If replication forks collapse at the outer edges of the array, the size of the end joining product after AlwNI digestion is close to 3.1 kb because most of the 1.5 kb *lacO* array is lost; collapse further into to the array generates larger products, accounting for the 3-4 kb range of products observed (Figure S2B). To test this hypothesis, the 3-4 kb species were cloned and sequenced using primers immediately flanking the *lacO* array (Figure S2C). In contrast to control clones (generated from replication in the absence of LacR), all of which contained 48 *lacO* repeats, the 24 clones from the 3-4 kb smear contained fewer than 48 *lacO* repeats (Figure 2D, products a-n). This result confirms that replication forks collapsed within the *lacO* array and then underwent end joining with loss of *lacO* repeats. Seventeen of these products (a-g) involved only deletions of the *lacO* repeats. This suggests that the

deletions might occur via single strand annealing (SSA) (Bhargava et al., 2016), which generates deletions between homologous sequences. The remaining 7 clones contained complex rearrangements, with microhomogy at the junction or insertions that likely arose from replication template-switching events (Figure 2D; product h-n). For example, product h appears to have arisen from fork collapse at the 5th repeat, followed by two successive microhomology-mediated strand invasion and copying events, followed by joining to a second fork that broke at the 15th repeat (Figure 2E). Together, the sequencing data strongly suggest that stressed replication forks collapse in the presence of B1-CDK1, generating DSBs that subsequently undergo end joining (Figures 2C and S2A), sometimes after repeated template-switching (Figure 2E).

Immunodepletion of DNA Polθ reduces mitotic ARPs

We next addressed the mechanism of end joining after mitotic CDK-induced fork collapse. As expected (Peterson et al., 2011), RAD51, which is essential for homologous recombination (HR), did not bind chromatin in the presence of B1-CDK1 (Figure S3A). Accordingly, immunodepletion of RAD51 from egg extracts had no effect on B1-CDK1-induced ARP formation (Figures S3B and S3C), nor did inhibition of RAD51 with a BRC peptide derived from BRCA2 (Figure S3D) (Long et al., 2011). Further, classical non-homologous end joining (NHEJ), which is also normally inhibited during mitosis (Hustedt and Durocher, 2016), was not required for ARP formation (Figure S3E). The structures of the mitotic ARPs (Figures 2C-E) suggested that MMEJ (microhomology-mediated end joining, also called alternative end joining) and/or SSA might be responsible for mitotic DSB repair. Indeed, immunodepletion of DNA

277 polymerase Polθ (Figure 3A), a major mediator of MMEJ known to make errors due to
278 replicative template-switching (Wyatt et al., 2016), decreased ARPs during replication of
279 LacR plasmid (Figures 3B and S3F) and pDPC (Figures 3C and S3G). Additionally,
280 Polθ depletion resulted in overall lower amounts of replication products (Figures S3F-
281 G), probably due to resection of unligated nascent strands. Moreover, Polθ depletion
282 virtually eliminated ARPs containing complex rearrangements (Figures 3D-3E). Thus, in
283 mitotic extracts where HR and NHEJ are inactive, MMEJ appears to become a major
284 pathway that mediates joining of DNA ends after fork breakage.

285

286 **Condensin is dispensible for mitotic CDK-induced fork instability**

287 Chromatin condensation, a central event in mitosis, has long been proposed to cause
288 DNA damage in under-replicated regions (El Achkar et al., 2005; Lukas et al., 2011).
289 We therefore investigated the role of chromatin condensation on mitotic fork collapse in
290 egg extracts. Although immunodepletion of the condensin subunit SMC2 inhibited B1-
291 CDK1-induced chromosome condensation (Figures S4A-B), it did not affect the
292 formation of ARPs (Figures S4C-D). These results are consistent with our finding that
293 condensin recruitment did not induce DNA damage in the absence of replication stress
294 (Figures 1B, 1D, 1G and S1C-S1E). Therefore, chromatin condensation, *per se*, is
295 neither necessary nor sufficient for fork instability in mitotic egg extracts.

296

297 **CMG unloading at stalled forks initiates mitotic fork breakage**

When replication forks stall on either side of a DNA inter-strand crosslink (ICL) in interphase egg extracts, CMGs are ubiquitylated and unloaded from chromatin by the CDC48/p97 ATPase (Fullbright et al., 2016; Semlow et al., 2016). The loss of CMGs from the stalled forks enables XPF-dependent ICL incision (Klein Douwel et al., 2014), which unhooks the lesion, leading to the formation of a double-stranded DNA break that is subsequently repaired via homologous recombination (Long et al., 2014). Inspired by this mechanism, we asked whether B1-CDK1-induced fork breakage at single stalled forks is caused by CMG unloading.

As shown previously (Dewar et al., 2015), CMGs that stalled at a LacR array did not dissociate from chromatin in interphase extracts (Figure 4A, lane 1). In contrast, in the presence of B1-CDK1, CMGs were unloaded efficiently (Figure 4A, lane 5). Addition of the p97 inhibitor NMS-873 (p97-i) prevented B1-CDK1-triggered CMG unloading and revealed a ladder of MCM7 species (Figure 4A, lane 7, red bracket) that was collapsed by USP21, a non-specific deubiquitylating enzyme (Figure 4A, lane 8). Therefore, B1-CDK1 induces MCM7 ubiquitylation and CMG unloading at single stalled forks, demonstrating that in mitotic conditions, fork convergence is not required for CMG unloading. Strikingly, p97-i suppressed the formation of ARPs on the LacR plasmid (Figure 4B), strongly suggesting that B1-CDK1-induced CMG unloading triggers replication fork breakage. Consistent with this interpretation, CMG unloading normally preceded replication fork breakage (Figure S4E). Interestingly, in the presence of p97-i, theta structures were converted to mature replication products (OC and SC) more efficiently in the presence of B1-CDK1 than in its absence (Figure 4B, compare lanes 16-20 and 6-10), suggesting that B1-CDK1 may promote fork progression through the

array when CMG unloading is prevented. Treatment with p97-i also reduced the mitotic CDK-induced γ-H2AX signal, consistent with inhibition of DSB formation (Figure S4F, compare lanes 13-18 and 19-24). As seen for LacR plasmid, p97-i also prevented ARP formation on pDPC (Figures 4C and S4G). Our data demonstrate that breakage of stalled forks in the presence of mitotic CDK requires p97 activity.

B1-CDK1-induced fork breakage requires PLK1 and AURKA, but not inhibition of ATR signaling

In dividing mammalian cells, inhibition of ATR signalling leads to fork breakage and chromosomal fragmentation that depends on the protein kinases CDK1, PLK1, and AURKA (Aurora kinase A) (Brown and Baltimore, 2000; Ragland et al., 2013). We therefore examined how these kinases affect fork breakage in egg extracts. As shown in Figure 4D, a potent ATR inhibitor (ATR-i, ETP-46464) did not induce breakage of forks stalled at a LacR array in the absence of B1-CDK1 (measured by ARP formation), even though the ATR-i abolished p-CHK1 (S345) and H2AX phosphorylation (lanes 7-12). Conversely, the fork breakage observed in the presence of B1-CDK1 occurred even though ATR signaling was active, as seen from p-CHK1 (Figure 4D, lanes 13-18), and ATR-i did not further enhance breakage in this setting (Figure 4D, lanes 19-24). Therefore, in interphase egg extract, ATR inhibition is insufficient to cause fork breakage, and in mitotic extract, B1-CDK1 induces fork breakage even in the presence of ATR activity. Strikingly, B1-CDK1-induced CMG ubiquitylation, CMG unloading, and fork breakage were all suppressed by selective inhibitors of PLK1 or AURKA (Figures 4E-G). We conclude that in egg extracts that are arrested in a mitotic state, ATR is

unable to suppress fork breakage, whereas breakage depends on PLK1 and AURKA, consistent with findings in mammalian cells (Ragland et al., 2013).

B1-CDK1 induces replication fork collapse

Replication fork collapse is defined as a state from which replication cannot restart, and we wanted to determine whether B1-CDK1 induces such a state in egg extracts. As we showed previously (Dewar et al., 2015), replication forks stalled at a LacR array are able to resume synthesis upon addition of IPTG, leading to mature, supercoiled replication products (Figure S4H, lanes 7-12). In the presence of B1-CDK1, IPTG did not generate mature replication products (Figure S4H, lanes 19-24), presumably because forks broke and underwent end-joining. However, when p97i was included with B1-CDK1, mature replication products were fully recovered after IPTG addition (Figure S4H, lanes 31-36). Thus, B1-CDK1 induces collapse of stalled replication forks and inhibition of p97-dependent CMG unloading is sufficient to prevent this collapse.

TRAIP promotes B1-CDK1-induced CMG unloading at stalled forks

We next sought to identify the E3 ubiquitin ligase responsible for B1-CDK1-dependent CMG unloading. $CRL2^{Lrr1}$ promotes CMG unloading during replication termination (Dewar et al., 2017), and it was possible that B1-CDK1 might target $CRL2^{Lrr1}$ to stalled CMGs. However, while the Cullin inhibitor MLN-4924 (Cul-i) blocked CMG unloading during replication termination in interphase (Figure S5A, compare lanes 1 and 4) (Dewar et al., 2017), it had almost no effect on mitotic CMG unloading from stalled forks

(Figure S5A, compare lanes 3 and 6), indicating the latter process does not involve $CRL2^{Lrr1}$. Therefore, a Cullin-independent E3 ubiquitin ligase is responsible for MCM7 ubiquitylation upon premature mitotic entry.

The E3 ubiquitin ligase TRAIP counteracts replication stress to maintain genome integrity (Feng et al., 2016; Harley et al., 2016; Hoffmann et al., 2016; Soo Lee et al., 2016), and we recently found that it is bound to replication forks that have stalled at a LacR array (Dewar et al., 2017). Strikingly, immunodepletion of TRAIP from egg extract (Figure 5A) prevented B1-CDK1-induced CMG unloading at stalled forks (Figure 5B, compare lanes 2 and 6), and it eliminated the polyubiquitylation of MCM7 detected in the presence of p97-i (Figure 5B, compare lanes 4 and 8). Furthermore, TRAIP depletion abolished the formation of ARPs during replication of LacR plasmid (Figure 5C, compare lanes 7-12 and 19-24) and pDPC (Figure S5B). Re-addition of recombinant wild TRAIP ($TRAIP^{WT}$) purified from bacteria (Wu et al., in revision, manuscript enclosed) to TRAIP-depleted egg extracts rescued the formation of mitotic ARPs (Figure 5D; and Figures S5C-S5E). We also added back $rTRAIP^{R18C}$, a point mutant of TRAIP that was identified in a human patient with primordial dwarfism (Harley et al., 2016) and that exhibits severely reduced E3 ligase activity (Wu et al., in revision, manuscript enclosed). Unlike $rTRAIP^{WT}$, $rTRAIP^{R18C}$ supported only low levels of ARP formation on LacR plasmid (Figure 5D, compare lanes 19-24 and 13-18). $rTRAIP^{\Delta PIP}$ lacking its C-terminal PCNA interaction motif (PIP box, amino acid 460-469) induced mitotic ARPs as efficiently as $rTRAIP^{WT}$ (Figure S5F), indicating that TRAIP's interation with PCNA is dispensible for CMG unloading. Accordingly, TRAIP's PIP box is not essential for the suppression of genome instability phenotypes in mammalian cells

(Hoffmann et al., 2016). We conclude that in the context of stalled forks, TRAIP is essential for mitotic CDK-induced CMG unloading and fork collapse.

Chromatin recruitment of TRAIP is not regulated by B1-CDK1

To understand how TRAIP is regulated, we monitored its binding to chromatin. As we showed previously (Dewar et al., 2017), in interphase egg extract TRAIP is associated with replisomes that have stalled at a LacR array (Figure 5B, lane 1). Therefore, TRAIP is present at forks before they are exposed to B1-CDK1. Upon addition of B1-CDK1, TRAIP was lost from the chromatin, but not when CMG unloading was inhibited with p97-i (Figure 5B, compare lanes 2 and 4). Interestingly, chromatin-bound TRAIP did not increase in the presence of B1-CDK1 and p97-i compared to the level observed before B1-CDK1 addition (Figure 5B, compare lanes 1 and 4). These data suggest that mitotic CDK activates TRAIP in a manner that does not involve its *de novo* recruitment to the fork.

Fork breakage in mitotic extracts is distinct from programmed incisions during ICL repair

The breakage of single stalled forks in mitotic egg extracts shown here is remeniscent of breakage at forks that have converged on cisplatin ICLs in interphase egg extracts in that both events require TRAIP-dependent CMG unloading (Figure 5 and Wu *et al*., in revision). We therefore asked whether B1-CDK-induced breakage at single forks also requires FANCI-FANCD2, XPF-ERCC1, or SLX1-SLX4, which promote DNA incisions

411 during ICL repair. Immunodepletion of FANCI-FANCD2 did not prevent mitotic ARP
412 formation on LacR plasmid (Figures S5G-H), nor did depletion of SLX4, XPF, or MUS81
413 (data not shown). We speculate that there might be redundancy among SLX1, XPF, and
414 MUS81 for mitotic fork breakage, or that other nucleases are involved. Our results
415 indicate that while ICL incisions and B1-CDK1-dependent replication fork collapse both
416 require TRAIP-dependent CMG unloading, these processes are otherwise
417 mechanistically distinct.

418

419 **TRAIP promotes CMG unloading from terminated replisomes in mitosis**

420 In *C. elegans* early embryos lacking $CUL2^{LRR-1}$, CMGs persist on chromatin until late
421 prophase, when they are unloaded from chromatin by p97 (Sonneville et al., 2017). This
422 observation indicated that an alternative ubiquitylation pathway acts to unload
423 terminated CMGs in mitosis, but the relevant E3 ubiquitin ligase has not been identified.
424 To determine whether TRAIP is involved in this pathway, we first addressed whether
425 *Xenopus* egg extracts recapitulate mitotic unloading of CMGs that have undergone
426 replication termination. To this end, we replicated a plasmid in interphase egg extracts
427 in the presence of Cul-i. In this condition, DNA synthesis went to completion (Figure
428 S6A), but CMG unloading was blocked due to inhibition of $CRL2^{Lrr1}$ (Figure 6A, compare
429 lanes 1 and 2; (Dewar et al., 2017)). Importantly, upon addition of B1-CDK1, CMG was
430 unloaded despite the presence of Cul-i (Figure 6A, lane 6), and this unloading was
431 blocked by p97-i (Figure 6A, lane 8). Therefore, as seen in worms, mitotic frog egg
432 extracts support $CRL2^{Lrr1}$-independent unloading of terminated CMGs. Interestingly, in
433 the presence of p97-i, MCM7 was ubiquitylated even more extensively than in

interphase extract (Figure 6A, compare lanes 7-8 and 3-4 and Figure S6B, compare lanes 5-6 and 1-2). This hyper-ubiquitylation was unaffected by Cul-i (Figure 6A, lane 8), indicating that it is $CRL2^{Lrr1}$-independent. Importantly, TRAIP depletion inhibited B1-CDK1-induced CMG unloading from terminated forks (Figure 6B, compare lanes 1 and 4, and Figure S6C, compare lanes 1 and 4) and MCM7 hyper-ubiquitylation in the presence of p97-i (Figure 6B, compare lanes 2 and 5 as well as lanes 3 and 6). These defects were reversed by $rTRAIP^{WT}$ but not $rTRAIP^{R18C}$ (Figures 6B and S6C). Therefore, in the absence of $CRL2^{Lrr1}$ activity, TRAIP promotes an alternative pathway to unload terminated CMGs in mitotic egg extract.

We next asked whether the *C. elegans* orthologue of TRAIP, which we called TRUL-1 (Traip Ubiquitin Ligase 1, encoded by the previously uncharacterised *C. elegans* gene B0432.13), controls removal of CMG from chromatin in mitosis of the first embryonic cell cycle (Figure 6C). On its own, RNAi depletion of TRUL-1 had no impact on CMG disassembly. However, simultaneous depletion of TRUL-1 and LRR-1 led to the persistence of the PSF-1 and CDC-45 subunits of CMG on mitotic chromatin (Figures 6D and S6D), indicating that *C. elegans* TRAIP is required for the removal of CMG from mitotic chromatin in animals. Moreover, compared to single depletion of TRUL-1 or LRR-1, double depletion led to the accumulation of CMG complexes containing unmodified MCM7 (Figure 6E, lane 7). This contrasts with the persistence of ubiquitylated CMGs observed upon depletion of p97's cofactor NPL-4 (Figures 6E and 6F, lane 8) (Sonneville et al., 2017). Thus, unloading of terminated CMGs in mitosis is a conserved function of TRAIP in metazoans. Moreover, our results suggest that in mitosis, TRAIP removes all forms of CMG from chromatin, whether they have

457 terminated or stalled (Figure S6E). In the latter case, CMG unloading triggers fork
458 breakage and complex end joining events (Figure 7).
459

DISCUSSION

When cells enter mitosis before DNA replication is complete, replication forks break. However, the molecular events underlying breakage and how breakage affects genome stability have remained unclear. Here, we show that in mitotic egg extracts, the E3 ubiquitin ligase TRAIP promotes p97-dependent replisome disassembly, followed by replication fork breakage and end joining events involving SSA and MMEJ. As discussed below, we propose that TRAIP-dependent fork breakage can be beneficial or detrimental, primarily depending on the burden of stressed forks at mitotic entry.

TRAIP's regulation of CMG ubiquitylation is critically dependent on cell-cycle status. In the presence of B1-CDK1, TRAIP targets stalled CMGs, which encircle ssDNA, and terminated CMGs, which probably encircle dsDNA (Figure S6Ei and ii; (Dewar et al., 2015)). In contrast, TRAIP's action in interphase extracts is more selective. In this setting, TRAIP promotes the ubiquitylation of CMGs that have converged on an ICL, leading to activation of two distinct mechanisms of ICL repair (Wu et al., in revision; Figure S6Eiii). However, it does not target terminated CMGs, a function performed by $CRL2^{Lrr1}$ in S phase (Figure S6Div; (Dewar et al., 2017; Sonneville et al., 2017)), nor does TRAIP appear to target CMG at single moving or stalled forks, which would cause premature fork collapse. In summary, TRAIP is specific for converged CMGs in interphase whereas in the presence of B1-CDK1, it appears to target any CMG, regardless of its configuration on DNA. Future work will be required to understand how TRAIP's selectivity is modulated by phosphorylation.

It has been widely proposed that replisome disassembly causes fork collapse (Cortez, 2015; Toledo et al., 2017), but in the absence of a mechanism for disassembly,

testing this idea has been impossible. Here, we identify such a mechanism. We show that B1-CDK1 induces TRAIP-dependent CMG ubiquitylation, p97-dependent CMG unloading, fork breakage, and fork collapse. This cascade is inhibited via multiple independent manipulations (CDK1-i, PLK1-i, p97-i, TRAIP depletion) that all target the replisome disassembly step. Thus, our data establish a firm relationship between replisome disassembly, fork breakage, and collapse. Whether the inability to restart the fork (collapse) results from replisome disassembly *per se* or a downstream event such as fork breakage is presently unclear. Moreover, without active recombinant MCM2-7, we cannot make ubiquityltion site mutations that would directly test whether CMG is the relevant TRAIP substrate responsible for fork breakage. Nevertheless, multiple lines of evidence point to CMG as the most likely target. First, TRAIP associates with stalled and terminated replication forks (Dewar et al., 2017; Hoffmann et al., 2016), ideally positioning TRAIP for CMG ubiquitylation. Second, prior to fork collapse, B1-CDK1 induces rapid and quantitative ubiquitylation of MCM7, the same protein that is ubiquitylated when CMG is unloaded during replication termination. Finally, CMG is unique among replisome components in that it cannot be reloaded *de novo* in S phase (Deegan and Diffley, 2016). Thus, loss of CMG provides a simple explanation for the irreversibility of fork collapse. It will be interesting to determine how this pathway relates to the depletion of RPA at the fork, which has also been proposed to trigger fork collapse and breakage (Toledo et al., 2013).

After stressed forks undergo breakage in mitotic extracts, the newly formed DNA breaks undergo two classes of joining events, as revealed by DNA sequencing. The first class involves deletions of *lacO* repeats. These products are most readily explained by

single-strand annealing, and they are probably favored by the highly repetitive nature of the *lacO* array. SSA is usually RAD52 dependent (Bhargava et al., 2016), and RAD52 has recently been shown to mediate DNA repair synthesis during mitosis (Bhowmick et al., 2016). However, we have not been able to test the involvement of RAD52 due to an inability to raise antibodies against *Xenopus* RAD52. The second class of end joining products is mediated by micro-homology, sometimes with multiple template-switching events, indicative of DNA Pol theta (Polθ)-mediated end joining (MMEJ, (Wyatt et al., 2016)). Consistent with this idea, aberrant replication products were reduced and complex rearrangements were eliminated in Polθ-depleted extracts. Our observation that broken forks appear to be processed primarily by SSA and MMEJ is consistent with the findings that HR and NHEJ are inhibited in mitosis (Figure S3A and (Hustedt and Durocher, 2016; Ochs et al., 2016; Peterson et al., 2011)) and that inhibition of these processes had no effect on the formation of aberrant replication products (Figures S3B-S3E). Notably, we detected only short-tract template switches typical of MMEJ. If template-switching events mediated by Polθ or other factors were followed by more processive DNA synthesis that is templated near the break, duplications could result that resemble copy number alterations observed in human cancer and congenital disease (Carvalho and Lupski, 2016; Leibowitz et al., 2015).

We envision at least two beneficial effects of TRAIP-dependent replisome disassembly in mitosis. One arises when converging forks are unable to complete DNA replication by anaphase, as seen at common fragile sites (CFS) (West and Chan, 2018). We propose that TRAIP-dependent CMG unloading leads to preferential breakage on the two leading strand templates because these are normally protected by

529 CMG (Fu et al., 2011) and therefore exposed after CMG dissociation (Figure S7). In this
530 scenario, one intact daughter chromosome would immediately be restored by gap filling,
531 and the other could be regenerated via joining of the two broken ends, albeit with sister
532 chromatid exchange and at the cost of of a deletion (Figure S7, left branch). Importantly,
533 this mechanism avoids the formation of acentric and dicentric chromosomes that would
534 result if the forks underwent random breakage (Figure S7, right branch) and thus biases
535 breakage at CFS towards more beneficial outcomes. Strikingly, CFS expression
536 induces chromosomal alterations that exhibit key features expected of our model,
537 including submicroscopic deletions covering the CFS locus, microhomologies at the
538 breakpoint junctions, and a very high frequency of sister chromatid exchanges (Glover
539 et al., 2017) (Figure S7, left branch). Unlike our biased breakage and end joining model,
540 break-induced replication models of CFS expression (Bhowmick et al., 2016;
541 Minocherhomji et al., 2015) do not readily account for the high incidence of sister
542 chromatid exchanges at CFS, and they would not be beneficial at CFS located distant
543 from chromosome ends.

544 A second possible benefit of TRAIP activity in mitosis is to disassemble
545 terminated CMGs that evaded the action of $CRL2^{Lrr1}$ in the previous S phase. In
546 principle, such CMGs might interfere with transcription or replication in the next cell
547 cycle. However, MCM2-7 complexes that are newly-loaded during mitotic exit, which
548 also encircle dsDNA, do not appear to interfere with these processes. Therefore, a
549 negative impact on transcription or replication would have to be specific to the full CMG
550 complex. In the absence of an obvious mechanism that explains strong detrimental
551 effects of residual CMGs, we favor the idea that TRAIP's primary function in mitosis is to

552 resolve unreplicated loci.

553 In addition to its beneficial effects, we propose that TRAIP-dependent CMG
554 unloading contributes to various genome instability phenomena that were previously
555 linked to mitotic DNA replication. These include: chromosome breakage that occurs
556 when S and M phase cells are fused (Duelli et al., 2007; Johnson and Rao, 1970; Rao
557 et al., 1982) or when mitotic CDK is prematurely activated in S phase by WEE1
558 inhibition (Dominguez-Kelly et al., 2011; Duda et al., 2016); and chromothripsis in
559 micronuclei that are still engaged in replication when they enter mitosis (Crasta et al.,
560 2012; Leibowitz et al., 2015; Ly et al., 2017). In these cases, massive chromosomal
561 breakage leads to genome instability or cell death. Notably, chromosome fragmentation
562 in the presence of WEE1 inhibitor and common fragile site expression are both MUS81-
563 dependent (Dominguez-Kelly et al., 2011; Duda et al., 2016; Naim et al., 2013; Ying et
564 al., 2013). In contrast, fork breakage in our experiments was not inhibited by MUS81
565 depletion. Whether this reflects a real difference in these processes, incomplete MUS81
566 depletion in extracts, or greater redundancy with other nucleases in extracts remains to
567 be determined. In the future, it will be interesting to determine whether TRAIP underlies
568 different genome instability phenomena caused by premature mitotic entry.

569 Much work towards understanding fork collapse focuses on its regulation by ATR.
570 While ATR-dependent phosphorylation of SMARCAL1 and WRN regulates fork stability,
571 these ATR substrates do not appear to account for ATR's essential role in preventing
572 fork collapse (Cortez, 2015; Pasero and Vindigni, 2017; Saldivar et al., 2017). Instead, a
573 growing body of evidence suggests that ATR affects fork stability indirectly (Toledo et al.,
574 2017). For example, ATR inhibition of late origin firing prevents exhaustion of the

nuclear RPA pool, causing fork deprotection and breakage (Toledo et al., 2013). However, given the concentration of RPA in egg extracts (~10 μM; (Walter et al., 1998; Wuhr et al., 2015)), and the concentration of DNA in our experiments, RPA cannot be exhausted in our experiments. Another hypothesis to explain the effect of ATR on fork stability involves the suppression of mitotic kinases. In cells treated with Aphidicolin and ATRi, replication fork collapse depends on B1-CDK1, AURKA, and PLK1 (Eykelenboom et al., 2013; Ragland et al., 2013; Ruiz et al., 2016). Even in the absence of exogenous replication stress, ATR prevents the premature accumulation of Cyclin B and PLK1 in S phase, which is critical to suppress replication fork collapse and genome instability (Ruiz et al., 2016; Saldivar et al., 2018). Thus, replication fork collapse in interphase can be due to premature activation of mitotic kinases. Consistent with the central importance of ATR in restraining B-CDK1, ATR is not required to stabilize stalled DNA replication forks in egg extracts that are permanently arrested in interphase (Figure 4D; (Luciani et al., 2004)). Conversely, when stressed forks are exposed to B1-CDK1, forks break, even in the presence of ATR activity. Based on these observations, we propose that in many studies where ATR suppresses replication fork collapse, this is due to suppression of B1-CDK1 activity and the prevention of TRAIP-dependent replisome disassembly.

In summary, our data suggest that when TRAIP is activated by mitotic CDK, a short temporal window opens in which replication forks can finish replication and terminate. The window closes when CMGs are ubiquitylated and extracted from chromatin. In the presence of a few unreplicated loci (e.g. fragile sites), CMG unloading and fork breakage promotes chromosome segregation and genome integrity, but when many forks are present (e.g. micronuclei, premature CDK1 activation in S phase),

massive DNA fragmentation results, leading to cell death or transformation. Whether the dwarfism phenotype observed in patients with TRAIP mutations results from defects in the resolution of unreplicated loci, persistence of terminated CMGs, defective ICL repair (Wu et al., in revision), or defects in other TRAIP-dependent processes remains to be established.

ACKNOWLEDGMENTS

We thank James Dewar, Emily Low, Justin Sparks, Kyle Vrtis, Daniel Finley, Puck Knipscheer, and Jan-Michael Peters for experimental protocols or reagents. We thank Alan D'Andrea, Randy King, Ralph Scully, and members of the Pellman and Walter laboratories for helpful discussion and critical reading of the manuscript. R.A.W. was supported by postdoctoral fellowship 131415-PF-17-168-01-DMC from the American Cancer Society. D.P. was supported by NIH grant CA213404. J.C.W. was supported by NIH grants GM080676 and HL098316. D.P. and J.C.W. are investigators of the Howard Hughes Medical Institute.

AUTHOR CONTRIBUTIONS

D.P. initiated the project. L.D., D.P., and J.C.W. designed the experiments, interpreted the results, and prepared the manuscript. R.A.W. contributed recombinant TRAIP proteins and obtained initial evidence that TRAIP is required for CMG unloading. R.S performed and K.L. directed experiments in worms (Figures 6C-6F and S6D). O.V.K.

620 contributed Figures 6A-B and S6A-C; L.D. designed and performed all other
621 experiments.
622
623 **DECLARATION OF INTERESTS**
624 The authors declare no competing interests.

REFERENCES

Ammazzalorso, F., Pirzio, L.M., Bignami, M., Franchitto, A., and Pichierri, P. (2010). ATR and ATM differently regulate WRN to prevent DSBs at stalled replication forks and promote replication fork recovery. EMBO J *29*, 3156-3169.

Baumann, C., Korner, R., Hofmann, K., and Nigg, E.A. (2007). PICH, a centromere-associated SNF2 family ATPase, is regulated by Plk1 and required for the spindle checkpoint. Cell *128*, 101-114.

Bhargava, R., Onyango, D.O., and Stark, J.M. (2016). Regulation of Single-Strand Annealing and its Role in Genome Maintenance. Trends Genet *32*, 566-575.

Bhowmick, R., and Hickson, I.D. (2017). The "enemies within": regions of the genome that are inherently difficult to replicate. F1000Res *6*, 666.

Bhowmick, R., Minocherhomji, S., and Hickson, I.D. (2016). RAD52 Facilitates Mitotic DNA Synthesis Following Replication Stress. Mol Cell *64*, 1117-1126.

Blow, J.J., and Laskey, R.A. (1986). Initiation of DNA replication in nuclei and purified DNA by a cell-free extract of Xenopus eggs. Cell *47*, 577-587.

Brenner, S. (1974). The genetics of Caenorhabditis elegans. Genetics *77*, 71-94.

Brown, E.J., and Baltimore, D. (2000). ATR disruption leads to chromosomal fragmentation and early embryonic lethality. Genes Dev *14*, 397-402.

Budzowska, M., Graham, T.G., Sobeck, A., Waga, S., and Walter, J.C. (2015). Regulation of the Rev1-pol zeta complex during bypass of a DNA interstrand cross-link. EMBO J *34*, 1971-1985.

Carvalho, C.M., and Lupski, J.R. (2016). Mechanisms underlying structural variant formation in genomic disorders. Nat Rev Genet *17*, 224-238.

Chan, K.L., North, P.S., and Hickson, I.D. (2007). BLM is required for faithful chromosome segregation and its localization defines a class of ultrafine anaphase bridges. EMBO J *26*, 3397-3409.

Cortez, D. (2015). Preventing replication fork collapse to maintain genome integrity. DNA Repair (Amst) *32*, 149-157.

Couch, F.B., Bansbach, C.E., Driscoll, R., Luzwick, J.W., Glick, G.G., Betous, R., Carroll, C.M., Jung, S.Y., Qin, J., Cimprich, K.A*., et al.* (2013). ATR phosphorylates SMARCAL1 to prevent replication fork collapse. Genes Dev *27*, 1610-1623.

Crasta, K., Ganem, N.J., Dagher, R., Lantermann, A.B., Ivanova, E.V., Pan, Y., Nezi, L., Protopopov, A., Chowdhury, D., and Pellman, D. (2012). DNA breaks and chromosome pulverization from errors in mitosis. Nature *482*, 53-58.

De Piccoli, G., Katou, Y., Itoh, T., Nakato, R., Shirahige, K., and Labib, K. (2012). Replisome stability at defective DNA replication forks is independent of S phase checkpoint kinases. Mol Cell *45*, 696-704.

Deegan, T.D., and Diffley, J.F. (2016). MCM: one ring to rule them all. Curr Opin Struct Biol *37*, 145-151.

Dewar, J.M., Budzowska, M., and Walter, J.C. (2015). The mechanism of DNA replication termination in vertebrates. Nature *525*, 345-350.

Dewar, J.M., Low, E., Mann, M., Raschle, M., and Walter, J.C. (2017). CRL2Lrr1 promotes unloading of the vertebrate replisome from chromatin during replication termination. Genes Dev *31*, 275-290.

Dominguez-Kelly, R., Martin, Y., Koundrioukoff, S., Tanenbaum, M.E., Smits, V.A., Medema, R.H., Debatisse, M., and Freire, R. (2011). Wee1 controls genomic stability during replication by regulating the Mus81-Eme1 endonuclease. J Cell Biol *194*, 567-579.

Duda, H., Arter, M., Gloggnitzer, J., Teloni, F., Wild, P., Blanco, M.G., Altmeyer, M., and Matos, J. (2016). A Mechanism for Controlled Breakage of Under-replicated Chromosomes during Mitosis. Dev Cell *39*, 740-755.

Duelli, D.M., Padilla-Nash, H.M., Berman, D., Murphy, K.M., Ried, T., and Lazebnik, Y. (2007). A virus causes cancer by inducing massive chromosomal instability through cell fusion. Curr Biol *17*, 431-437.

Dungrawala, H., Rose, K.L., Bhat, K.P., Mohni, K.N., Glick, G.G., Couch, F.B., and Cortez, D. (2015). The Replication Checkpoint Prevents Two Types of Fork Collapse without Regulating Replisome Stability. Mol Cell *59*, 998-1010.

Duxin, J.P., Dewar, J.M., Yardimci, H., and Walter, J.C. (2014). Repair of a DNA-protein crosslink by replication-coupled proteolysis. Cell *159*, 346-357.

El Achkar, E., Gerbault-Seureau, M., Muleris, M., Dutrillaux, B., and Debatisse, M. (2005). Premature condensation induces breaks at the interface of early and late replicating chromosome bands bearing common fragile sites. Proc Natl Acad Sci U S A *102*, 18069-18074.

678 Eykelenboom, J.K., Harte, E.C., Canavan, L., Pastor-Peidro, A., Calvo-Asensio, I., Llorens-Agost, M., and Lowndes,
679 N.F. (2013). ATR activates the S-M checkpoint during unperturbed growth to ensure sufficient replication prior to
680 mitotic onset. Cell Rep *5*, 1095-1107.
681 Feng, W., Guo, Y., Huang, J., Deng, Y., Zang, J., and Huen, M.S. (2016). TRAIP regulates replication fork recovery
682 and progression via PCNA. Cell Discov *2*, 16016.
683 Fu, Y.V., Yardimci, H., Long, D.T., Ho, T.V., Guainazzi, A., Bermudez, V.P., Hurwitz, J., van Oijen, A., Scharer,
684 O.D., and Walter, J.C. (2011). Selective bypass of a lagging strand roadblock by the eukaryotic replicative DNA
685 helicase. Cell *146*, 931-941.
686 Fullbright, G., Rycenga, H.B., Gruber, J.D., and Long, D.T. (2016). p97 Promotes a Conserved Mechanism of
687 Helicase Unloading during DNA Cross-Link Repair. Mol Cell Biol *36*, 2983-2994.
688 Glover, T.W., Wilson, T.E., and Arlt, M.F. (2017). Fragile sites in cancer: more than meets the eye. Nat Rev Cancer
689 *17*, 489-501.
690 Harley, M.E., Murina, O., Leitch, A., Higgs, M.R., Bicknell, L.S., Yigit, G., Blackford, A.N., Zlatanou, A.,
691 Mackenzie, K.J., Reddy, K.*, et al.* (2016). TRAIP promotes DNA damage response during genome replication and is
692 mutated in primordial dwarfism. Nat Genet *48*, 36-43.
693 Harrigan, J.A., Belotserkovskaya, R., Coates, J., Dimitrova, D.S., Polo, S.E., Bradshaw, C.R., Fraser, P., and
694 Jackson, S.P. (2011). Replication stress induces 53BP1-containing OPT domains in G1 cells. J Cell Biol *193*, 97-
695 108.
696 Hendrickson, M., Madine, M., Dalton, S., and Gautier, J. (1996). Phosphorylation of MCM4 by cdc2 protein kinase
697 inhibits the activity of the minichromosome maintenance complex. Proc Natl Acad Sci U S A *93*, 12223-12228.
698 Hills, S.A., and Diffley, J.F. (2014). DNA replication and oncogene-induced replicative stress. Curr Biol *24*, R435-
699 444.
700 Hoffmann, S., Smedegaard, S., Nakamura, K., Mortuza, G.B., Raschle, M., Ibanez de Opakua, A., Oka, Y., Feng, Y.,
701 Blanco, F.J., Mann, M.*, et al.* (2016). TRAIP is a PCNA-binding ubiquitin ligase that protects genome stability after
702 replication stress. J Cell Biol *212*, 63-75.
703 Holland, A.J., and Cleveland, D.W. (2012). Chromoanagenesis and cancer: mechanisms and consequences of
704 localized, complex chromosomal rearrangements. Nat Med *18*, 1630-1638.
705 Hustedt, N., and Durocher, D. (2016). The control of DNA repair by the cell cycle. Nat Cell Biol *19*, 1-9.
706 Johnson, R.T., and Rao, P.N. (1970). Mammalian cell fusion: induction of premature chromosome condensation in
707 interphase nuclei. Nature *226*, 717-722.
708 Kato, H., and Sandberg, A.A. (1968). Chromosome pulverization in human cells with micronuclei. J Natl Cancer
709 Inst *40*, 165-179.
710 Klein Douwel, D., Boonen, R.A., Long, D.T., Szypowska, A.A., Raschle, M., Walter, J.C., and Knipscheer, P.
711 (2014). XPF-ERCC1 acts in Unhooking DNA interstrand crosslinks in cooperation with FANCD2 and
712 FANCP/SLX4. Mol Cell *54*, 460-471.
713 Knipscheer, P., Raschle, M., Smogorzewska, A., Enoiu, M., Ho, T.V., Scharer, O.D., Elledge, S.J., and Walter, J.C.
714 (2009). The Fanconi anemia pathway promotes replication-dependent DNA interstrand cross-link repair. Science
715 *326*, 1698-1701.
716 Lebofsky, R., Takahashi, T., and Walter, J.C. (2009). DNA replication in nucleus-free Xenopus egg extracts.
717 Methods Mol Biol *521*, 229-252.
718 Leibowitz, M.L., Zhang, C.Z., and Pellman, D. (2015). Chromothripsis: A New Mechanism for Rapid Karyotype
719 Evolution. Annu Rev Genet *49*, 183-211.
720 Liu, P., Erez, A., Nagamani, S.C., Dhar, S.U., Kolodziejska, K.E., Dharmadhikari, A.V., Cooper, M.L.,
721 Wiszniewska, J., Zhang, F., Withers, M.A.*, et al.* (2011). Chromosome catastrophes involve replication mechanisms
722 generating complex genomic rearrangements. Cell *146*, 889-903.
723 Long, D.T., Joukov, V., Budzowska, M., and Walter, J.C. (2014). BRCA1 promotes unloading of the CMG helicase
724 from a stalled DNA replication fork. Mol Cell *56*, 174-185.
725 Long, D.T., Raschle, M., Joukov, V., and Walter, J.C. (2011). Mechanism of RAD51-dependent DNA interstrand
726 cross-link repair. Science *333*, 84-87.
727 Luciani, M.G., Oehlmann, M., and Blow, J.J. (2004). Characterization of a novel ATR-dependent, Chk1-
728 independent, intra-S-phase checkpoint that suppresses initiation of replication in Xenopus. J Cell Sci *117*, 6019-
729 6030.
730 Lukas, C., Savic, V., Bekker-Jensen, S., Doil, C., Neumann, B., Pedersen, R.S., Grofte, M., Chan, K.L., Hickson,
731 I.D., Bartek, J.*, et al.* (2011). 53BP1 nuclear bodies form around DNA lesions generated by mitotic transmission of
732 chromosomes under replication stress. Nat Cell Biol *13*, 243-253.

Ly, P., Teitz, L.S., Kim, D.H., Shoshani, O., Skaletsky, H., Fachinetti, D., Page, D.C., and Cleveland, D.W. (2017). Selective Y centromere inactivation triggers chromosome shattering in micronuclei and repair by non-homologous end joining. Nat Cell Biol *19*, 68-75.
Mankouri, H.W., Huttner, D., and Hickson, I.D. (2013). How unfinished business from S-phase affects mitosis and beyond. EMBO J *32*, 2661-2671.
Minocherhomji, S., Ying, S., Bjerregaard, V.A., Bursomanno, S., Aleliunaite, A., Wu, W., Mankouri, H.W., Shen, H., Liu, Y., and Hickson, I.D. (2015). Replication stress activates DNA repair synthesis in mitosis. Nature.
Naim, V., Wilhelm, T., Debatisse, M., and Rosselli, F. (2013). ERCC1 and MUS81-EME1 promote sister chromatid separation by processing late replication intermediates at common fragile sites during mitosis. Nat Cell Biol *15*, 1008-1015.
Ochs, F., Somyajit, K., Altmeyer, M., Rask, M.B., Lukas, J., and Lukas, C. (2016). 53BP1 fosters fidelity of homology-directed DNA repair. Nat Struct Mol Biol *23*, 714-721.
Pasero, P., and Vindigni, A. (2017). Nucleases Acting at Stalled Forks: How to Reboot the Replication Program with a Few Shortcuts. Annu Rev Genet *51*, 477-499.
Peterson, S.E., Li, Y., Chait, B.T., Gottesman, M.E., Baer, R., and Gautier, J. (2011). Cdk1 uncouples CtIP-dependent resection and Rad51 filament formation during M-phase double-strand break repair. J Cell Biol *194*, 705-720.
Prokhorova, T.A., Mowrer, K., Gilbert, C.H., and Walter, J.C. (2003). DNA replication of mitotic chromatin in Xenopus egg extracts. Proc Natl Acad Sci U S A *100*, 13241-13246.
Ragland, R.L., Patel, S., Rivard, R.S., Smith, K., Peters, A.A., Bielinsky, A.K., and Brown, E.J. (2013). RNF4 and PLK1 are required for replication fork collapse in ATR-deficient cells. Genes Dev *27*, 2259-2273.
Rao, P.N., Johnson, R.T., and Sperling, K. (1982). Premature Chromosome Condensation: Application in Basic,Clinical, and Mutation Research (New York: Academic Press).
Raschle, M., Knipscheer, P., Enoiu, M., Angelov, T., Sun, J., Griffith, J.D., Ellenberger, T.E., Scharer, O.D., and Walter, J.C. (2008). Mechanism of replication-coupled DNA interstrand crosslink repair. Cell *134*, 969-980.
Raschle, M., Smeenk, G., Hansen, R.K., Temu, T., Oka, Y., Hein, M.Y., Nagaraj, N., Long, D.T., Walter, J.C., Hofmann, K.*, et al.* (2015). DNA repair. Proteomics reveals dynamic assembly of repair complexes during bypass of DNA cross-links. Science *348*, 1253671.
Ruiz, S., Mayor-Ruiz, C., Lafarga, V., Murga, M., Vega-Sendino, M., Ortega, S., and Fernandez-Capetillo, O. (2016). A Genome-wide CRISPR Screen Identifies CDC25A as a Determinant of Sensitivity to ATR Inhibitors. Mol Cell *62*, 307-313.
Saldivar, J.C., Cortez, D., and Cimprich, K.A. (2017). The essential kinase ATR: ensuring faithful duplication of a challenging genome. Nat Rev Mol Cell Biol *18*, 622-636.
Saldivar, J.C., Hamperl, S., Bocek, M.J., Chung, M., Bass, T.E., Cisneros-Soberanis, F., Samejima, K., Xie, L., Paulson, J.R., Earnshaw, W.C.*, et al.* (2018). An intrinsic S/G2 checkpoint enforced by ATR. Science *361*, 806-810.
Semlow, D.R., Zhang, J., Budzowska, M., Drohat, A.C., and Walter, J.C. (2016). Replication-Dependent Unhooking of DNA Interstrand Cross-Links by the NEIL3 Glycosylase. Cell *167*, 498-511 e414.
Sonneville, R., Moreno, S.P., Knebel, A., Johnson, C., Hastie, C.J., Gartner, A., Gambus, A., and Labib, K. (2017). CUL-2LRR-1 and UBXN-3 drive replisome disassembly during DNA replication termination and mitosis. Nat Cell Biol *19*, 468-479.
Soo Lee, N., Jin Chung, H., Kim, H.J., Yun Lee, S., Ji, J.H., Seo, Y., Hun Han, S., Choi, M., Yun, M., Lee, S.G.*, et al.* (2016). TRAIP/RNF206 is required for recruitment of RAP80 to sites of DNA damage. Nat Commun *7*, 10463.
Stephens, P.J., Greenman, C.D., Fu, B., Yang, F., Bignell, G.R., Mudie, L.J., Pleasance, E.D., Lau, K.W., Beare, D., Stebbings, L.A.*, et al.* (2011). Massive genomic rearrangement acquired in a single catastrophic event during cancer development. Cell *144*, 27-40.
Strausfeld, U.P., Howell, M., Descombes, P., Chevalier, S., Rempel, R.E., Adamczewski, J., Maller, J.L., Hunt, T., and Blow, J.J. (1996). Both cyclin A and cyclin E have S-phase promoting (SPF) activity in Xenopus egg extracts. J Cell Sci *109*, 1555-1563.
Techer, H., Koundrioukoff, S., Nicolas, A., and Debatisse, M. (2017). The impact of replication stress on replication dynamics and DNA damage in vertebrate cells. Nat Rev Genet *18*, 535-550.
Timmons, L., and Fire, A. (1998). Specific interference by ingested dsRNA. Nature *395*, 854.
Toledo, L., Neelsen, K.J., and Lukas, J. (2017). Replication Catastrophe: When a Checkpoint Fails because of Exhaustion. Mol Cell *66*, 735-749.
Toledo, L.I., Altmeyer, M., Rask, M.B., Lukas, C., Larsen, D.H., Povlsen, L.K., Bekker-Jensen, S., Mailand, N., Bartek, J., and Lukas, J. (2013). ATR prohibits replication catastrophe by preventing global exhaustion of RPA. Cell *155*, 1088-1103.

789 Walter, J., and Newport, J. (2000). Initiation of eukaryotic DNA replication: origin unwinding and sequential
790 chromatin association of Cdc45, RPA, and DNA polymerase alpha. Mol Cell *5*, 617-627.
791 Walter, J., Sun, L., and Newport, J. (1998). Regulated chromosomal DNA replication in the absence of a nucleus.
792 Mol Cell *1*, 519-529.
793 West, S.C., and Chan, Y.W. (2018). Genome Instability as a Consequence of Defects in the Resolution of
794 Recombination Intermediates. Cold Spring Harb Symp Quant Biol.
795 Wuhr, M., Guttler, T., Peshkin, L., McAlister, G.C., Sonnett, M., Ishihara, K., Groen, A.C., Presler, M., Erickson,
796 B.K., Mitchison, T.J.*, et al.* (2015). The Nuclear Proteome of a Vertebrate. Curr Biol *25*, 2663-2671.
797 Wyatt, D.W., Feng, W., Conlin, M.P., Yousefzadeh, M.J., Roberts, S.A., Mieczkowski, P., Wood, R.D., Gupta, G.P.,
798 and Ramsden, D.A. (2016). Essential Roles for Polymerase theta-Mediated End Joining in the Repair of
799 Chromosome Breaks. Mol Cell *63*, 662-673.
800 Ying, S., Minocherhomji, S., Chan, K.L., Palmai-Pallag, T., Chu, W.K., Wass, T., Mankouri, H.W., Liu, Y., and
801 Hickson, I.D. (2013). MUS81 promotes common fragile site expression. Nat Cell Biol *15*, 1001-1007.

802

FIGURE LEGENDS

Figure 1. Mitotic CDK triggers aberrant processing of stalled DNA replication forks in *Xenopus* egg extracts

(**A**) Schematic of experimental approach to test effect of B1-CDK1 on DNA replication. APH, DNA polymerase inhibitor aphidicolin.

(**B**) A 3 kb pBlueScript plasmid was replicated according to (A) and products were separated on a native agarose gel followed by autoradiography. Unless stated otherwise, the '0 minute' time point refers to NPE addition.

(**C**) Schematic of DNA replication for LacR-bound p[*lacO*$_{48}$] plasmid.

(**D**) p[*lacO*$_{48}$] was replicated according to (C) under the indicated conditions.

(**E**) p[*lacO*$_{48}$] was replicated according to (C) in the absence or presence of LacR and IPTG (10 mM, 15 min incubation in NPE before mixing with "licensing" mixture), as indicated.

(**F**) Schematic of replication for pDPC, containing four 46 kDa M.HpaII DNA methyltransferases at the indicated positions. Products formed in the presence and absence of B1-CDK1 are indicated.

(**G**) pControl or pDPC was replicated according to (F) using the indicated conditions. From (A) to (G), B1-CDK1 was added to "licensing" mixture at a concentration of 50 ng/μL and its final concentration in the overall reaction is 16.7 ng/μL (see method). RI, replication intermediate; OC, open circle; SC: supercoil; θ, theta structure; ARP, aberrant replication product.

See also **Figure S1**.

Figure 2. Mitotic processing of stalled replication forks leads to complex DNA rearrangements

(**A**) Structure of the 4.6 kb p[*lacO*$_{48}$] plasmid. Numbers mark the length of the indicated DNA segments in kilo-basepairs (kb).

(**B**) p[*lacO*$_{48}$] was replicated in the presence of Buffer or B1-CDK1. At the indicated time points, replication products were isolated and digested with AlwNI and AflII, or AlwNI, as indicated. Numbers label the size of linear fragments in kb; Y, double-Y or single-Y structure (see panel C).

(**C**) Model explaining the restriction products observed in (B). Although the model favors fork breakage on the leading strand, the possibility of fork breakage on the lagging strand has not been excluded. A more detailed model is presented in Figure S2A.

(**D**) The smear of ~3-4 kb mitotic DNA replication products generated after AlwNI digestion in (B) was self-ligated, cloned and sequenced. The controls are replication products of the same plasmid from a mitotic reaction lacking LacR. The *lacO* repeats, shown as white boxes, are separated by four unique spacers shown in different colors. Inset, DNA sequences of the *lacO* repeat and four spacers. The detailed structure of the entire *lacO* array is shown in Figure S2C.

(**E**) A model for the generation of product h in (D) from multiple template-switching events.

See also **Figure S2**.

Figure 3. Depletion of DNA polymerase θ disrupts the generation of aberrant replication product in the presence of mitotic CDK

(**A**) Mock-depleted and Polθ-depleted *Xenopus* egg extracts were blotted for Polθ and MCM7, alongside a serial dilution of mock-depleted extracts. Asterisk, background band.

(**B**) LacR-bound p[*lacO*$_{48}$] was replicated in mock-depleted or Polθ-depleted extracts with or without B1-CDK1 treatment. Total DNA replication and ARP were quantified in Figure S3F.

(**C**) pDPC was replicated in mock-depleted or Polθ-depleted egg extracts with or without B1-CDK1 treatment. Total DNA replication and ARP were quantified in Figure S3G.

(**D**) Structure of clones derived from mitotic ARPs in mock- or Polθ-depleted extracts. LacR-bound p[*lacO*$_{48}$] was replicated in mock- or Polθ-depleted extracts with B1-CDK1 treatment. The smear of ~3-4 kb mitotic DNA replication products generated after AlwNI digestion was self-ligated, cloned and sequenced. Elements in the box at the bottom show the sequences of *lacO* and spacers.

(**E**) Comparison of mitotic ARP-derived clones in the presence or absence of Polθ. Mock depletion (Figure 2D) and Polθ depletion (Figure S3H) in experiment 1 (Exp. 1) were performed independently whereas they were performed side by side (Figure 3D) in experiment 2 (Exp. 2). The shown *p*-value was from unpaired two-tailed Student's *t*-test.

In (B) and (C), OC, open circle; SC, supercoil; θ, theta structure; ARP, aberrant replication product.

See also **Figure S3**.

Figure 4. Mitotic CDK-induced fork collapse requires p97-dependent CMG unloading

(**A**) LacR-bound p[*lacO*$_{48}$] plasmid was replicated and treated as schemed. Chromatin-bound proteins were recovered and blotted with the indicated antibodies. Red bracket, ubiquitylated MCM7. Histone H3 served as loading control. Note that the MCM7 antibody cross-reacts with USP21.

(**B**) LacR-bound p[*lacO*$_{48}$] was replicated in the presence or absence of p97-i and B1-CDK1, as indicated. OC, open circle; SC: supercoil; θ, theta structure; ARP, aberrant replication product.

(**C**) pDPC was replicated in the presence or absence of p97-i and B1-CDK1, as indicated. ARP, OC+SC and overall DNA replication were quantified in Figure S4G.

(**D**) Effect of ATR inhibition on stalled replication forks. LacR-bound p[*lacO*$_{48}$] plasmid was replicated as schemed. Final concentration of ATR inhibitor (ATR-i; ETP-46464) in the reactions was 200 μM. Extracts with [α-^{32}P]-dATP were sampled to track DNA replication while extracts without [α-^{32}P]-dATP were sampled in parallel to track CHK1-S345 phosphorylation (CHK1-pS345), γ-H2AX. Histon H3 was included as loading control.

(**E**) LacR-bound p[*lacO*$_{48}$] plasmid was replicated and treated as in (A). The final concentrations of PLK1 inhibitor (PLK1-i, BI-2536) and Aurora kinase A inhibitor (AURKA-i, MLN-8237) were 50 μM and 10 μM, respectively. DMSO and p97-i treatments were included as controls. Chromatin-bound proteins were recovered and blotted with the indicated antibodies.

(**F**) LacR-bound p[*lacO*$_{48}$] was replicated as schemed. PLK1-i was added 10 minutes before B1-CDK1 treatment, with a final concentration of 50 μM in the overall reaction.

(**G**) LacR-bound p[*lacO*$_{48}$] was replicated in the presence of PLK1-i or AURKA-i, as schemed in (F). The final concentrations of PLK1-i and AURKA-i were 50 μM and 10 μM, respectively.

See also **Figure S4**.

Figure 5. E3 ubiquitin ligase TRAIP promotes mitotic CMG unloading from a stalled replication fork

(**A**) Mock-depleted and TRAIP-depleted egg extracts were blotted for TRAIP and MCM7 alongside a serial dilution of mock-depleted extracts.

(**B**) LacR-bound p[*lacO*$_{48}$] plasmid was replicated in mock-depleted or TRAIP-depleted egg extracts and treated as schemed. Chromatin-bound proteins were recovered and blotted with the indicated antibodies.

(**C**) LacR-bound p[*lacO*$_{48}$] was replicated in mock-depleted or TRAIP-depleted extracts with or without B1-CDK1 treatment.

(**D**) LacR-bound p[*lacO*$_{48}$] was replicated in mitotic mock-depleted or TRAIP-depleted egg extracts with or without recombinant wildtype TRAIP (rTRAIP^{WT}) or R18C mutant (rTRAIP^{R18C}), as indicated. rTRAIP^{WT} and rTRAIP^{R18C} were added to NPE at a concentration of 21 ng/μL (~7-fold over endogenous TRAIP, see quantification in Figure S5C). Matched buffer without recombinant protein was added to control reactions. Addition of rTRAIP^{WT} at endogenous level (S5C) into TRAIP-depleted extracts also led to substantial rescue of mitotic ARPs (Figures S5D and S5E).

See also **Figure S5**.

Figure 6. TRAIP mediates unloading of terminated CMGs in mitosis

(**A**) p[*lacO*$_{48}$] plasmid, in the absence of LacR, was replicated and treated as schemed. Chromatin-bound proteins were recovered and blotted with the indicated antibodies. Red brackets indicate the levels of MCM7 ubiquitylation.

(**B**) p[*lacO*$_{48}$] plasmid, in the absence of LacR, was replicated in mock-depleted or TRAIP-depleted egg extracts supplemented with or without rTRAIP^{WT} (~4-fold of endogenous TRAIP), or rTRAIP^{R18C} (~9-fold of endogenous TRAIP), followed by indicated treatments. Chromatin-bound proteins were recovered and blotted with the indicated antibodies.

(**C**) Illustration of the first cell cycle of the *C. elegans* embryo. Following S-phase, the female and male pronuclei migrate towards each other and chromosomes condense during prophase. Subsequently, the two sets of chromosomes intermingle during metaphase.

(**D**) Timelapse video microscopy of the first embryonic mitosis, in embryos exposed to the indicated RNAi and expressing GFP-PSF-1 and mCherry-HistoneH2B. The female pronucleus is shown during early prophase, before convergence with the male pronucleus (mid and late prophase). The arrows indicate examples of persistence of GFP-PSF-1 on condensed chromatin during mitosis. Scale bar, 5 μm.

(**E-F**) Worms in which the PSF-1 subunit of the CMG helicase was tagged with GFP were subjected to the indicated RNAi treatment. GFP-PSF-1 was recovered by immunoprecipitation, and the association of the indicated proteins was then monitored by immunoblotting against the indicated proteins (E) or ubiquitin (F).

See also **Figure S6**.

Figure 7. Model of CMG unloading, fork breakage and complex DNA rearrangements upon premature mitotic entry

When a replication fork encounters a replication barrier (indicated as a red hexagonal STOP sign), the replisome containing CMG and TRAIP is stably stalled during interphase. With the increase of mitotic CDK activity, E3 ubiquitin ligase TRAIP is activated (directly or indirectly) to cause CMG ubiquitylation on MCM7 subunit, which in turn triggers CMG unloading from chromatin by CDC48/p97 ATPase. Loss of CMG leads to incision by so far unknown DNA nuclease(s), followed by error-prone double-strand repair by MMEJ and/or SSA, which results in DNA rearrangements such as deletions and insertions from template-switching events.

See also **Figure S7**.

METHODS

No statistical methods were used to predetermine sample size. All experiments were performed at least twice independently using separate preparations of *Xenopus* egg extracts. A representative result is shown.

Protein purification. To purify biotinylated LacR, the LacR-Avi expressing plasmid pET11a[LacR-Avi] (Avidity, Denver, CO) and biotin ligase expressing plasmid pBirAcm (Avidity, Denver, CO) were co-transformed into T7 Express cells (New England Biolabs). Cultures were supplemented with 50 mM biotin (Research Organics, Cleveland, OH). Expression of LacR-Avi and the biotin ligase was induced by addition of IPTG **(**Isopropyl β-D-thiogalactoside, Sigma, St. Louis, MO) to a final concentration of 1 mM. Biotinylated LacR-Avi was then purified as described (Dewar et al., 2015). BRC (a ~35 amino acid peptide derived from BRCA2 that binds RAD51) and BRC*** (BRC peptide with mutations at RAD51 binding sites), a gift of K. Vrtis, were purified as reported (Long et al., 2011). rTRAIP and rTRAIP-R18C were expressed from a 6xHis-SUMO plasmid in bacteria and purified as described (Wu et al. in revision). Other proteins used in this study were Cyclin B1-CDK1 (Life Technologies Cat #PR4768C and EMD Millipore Cat #14-450M), Cyclin A2 (Creative Biomart, Cat #CCNA2-6798H) and Cyclin E-CDK2 (EMD Millipore Cat #14-475). USP21 was a gift from D. Finley.

DNA constructs. The 4.6 kb p[$lacO_{48}$] plasmid (a generous gift of K. Vrtis) contains an array of 48 *lacO* sites which can be bound by the *lac* repressor (LacR) to form replication barriers. The pDPC plasmid (4.3 kb), a generous gift of J. Sparks, was

975 constructed based on a previous protocol (Duxin et al., 2014). Control plasmid (pControl)
976 used in Figure 1G has the same DNA sequence as pDPC, but lacks crosslinks.
977
978 ***Xenopus* egg extracts and DNA replication.** Egg extracts were prepared using
979 *Xenopus laevis* (Nasco Cat #LM0053MX). All experiments involving animals were
980 approved by the Harvard Medical School Institutional Animal Care and use Committee
981 (IACUC) and conform to relevant regulatory standards. *Xenopus* egg extracts including
982 Low Speed Supernatant (LSS), High Speed Supernatant (HSS), and Nucleoplasmic
983 egg extract (NPE) were prepared as described (Blow and Laskey, 1986; Lebofsky et al.,
984 2009).
985 To assess the effects of mitotic cyclins, demembranated sperm chromatin from
986 *Xenopus laevis* males was incubated in LSS (4,000 sperms/μL LSS) for 40 minutes at
987 room temperature to form nuclei. The reactions were subsequently incubated with a
988 range of concentrations of mitotic B1-CDK1. Nuclear envelope integrity and chromatin
989 condensation were monitored by microscopy after Hoechst staining (see below). The
990 concentration (50 ng/μL) that triggered nuclear envelopment breakdown and
991 chromosome condensation was chosen to trigger mitotic entry in subsequent
992 experiments.
993 For interphase DNA replication, sperm chromatin or plasmid DNA was first
994 incubated in HSS (final concentration of 7.5-15.0 ng DNA/μL HSS) for 30 minutes at
995 room temperature to license the DNA for replication (“licensing”), followed by the
996 addition of 2 volumes of NPE to initiate CDK2-dependent replication. To radiolabel the
997 nascent strands during replication, NPE was supplemented with trace amounts of [α-

998 ^{32}P]-dATP. Mitotic DNA replication was performed essentially as described (Prokhorova
999 et al., 2003). Briefly, after 30 minutes, 0.9 volumes of licensing reaction was incubated
1000 with 0.1 volumes of mitotic B1-CDK1 for 30 minutes at room temperature, followed by
1001 addition of 2 volumes of NPE. In the “licensing” mixture, the concentration of B1-CDK1
1002 was 50 ng/μL, and its concentration in the final replication reaction was 16.7 ng/μL.
1003 Unless stated otherwise, the ‘0 minute’ time point refers to the moment of NPE addition.
1004 2 μL aliquots of replication reaction were stopped with 5 μl of stop solution A (5% SDS,
1005 80 mM Tris pH8.0, 0.13% phosphoric acid, 10% Ficoll) supplemented with 1 μl 20
1006 mg/ml Proteinase K (Roche, Nutley, NJ). Samples were incubated for 1 hour at 37°C
1007 prior to electrophoresis on a 0.9% native agarose gel. Gels were dried and radioactivity
1008 was detected using a phosphorimager (Lebofsky et al., 2009).

1009 To induce replication fork stalling using LacR, one volume of p[*lacO*$_{48}$] (200
1010 ng/μL) was incubated with one volume of recombinant LacR (36 μM) for 45-60 minutes
1011 at room temperature. Next, 0.1 volumes of the mixture was combined with 0.9 volumes
1012 of HSS for licensing, followed by addition of 2 volumes of NPE for initiation of
1013 replication. To inhibit the binding of LacR to the *lacO* array, IPTG was added to NPE to
1014 a final concentration of 10 mM and incubated for 15 minutes prior to use in replication
1015 (Figure 1E) or added into replication reactions after fork stalling (Figures S4H and S6C)
1016 at the indicated time.

1017 For replication assays with inhibitors, NPE was supplemented with inhibitors for
1018 15 minutes at room temperature before addition to the licensing mixture. Inhibitors were
1019 used at the following final concentrations in replication reaction: Aphidicolin (Sigma Cat
1020 #A0781-5MG), 2.2 μM or 0.97 μM, as indicated; CDC7 inhibitor PHA-767491 (Sigma

Cat #PZ0178), 266 μM; p97 inhibitor NMS-873 (Sigma Cat #SML1128-5MG), 266 μM; DNA-PKcs inhibitor NU-7441, 133 μM; BRC or BRC***, 1 μg/μL; Cullin inhibitor MLN-4924 (Active Biochem Cat #A-1139), 266 μM; PLK1 kinase inhibitor BI-2536 (Adooq Cat # A10134, 50 μM; Aurora A kinase inhibitor MK-5108 (Selleck Cat #S2770), 10 μM and ATR inhibitor (ETP-46464; Sigma Cat #SML1321) , 200 μM. For the CDK1 inhibition assay in Figure S1G, CDK1 inhibitor RO-3306 (EMD Millipore Cat #217699-5MG) was incubated with the replication reaction containing stalled replication forks for 5 minutes before the addition of B1-CDK1.

Immunodepletion and Western blotting. Immunodepletions using antibodies against *Xenopus laevis* FANCD2 (Knipscheer et al., 2009), FANCI (Duxin et al., 2014), SMC2 (antigen: Ac-CSKTKERRNRMEVDK-OH, New England Peptide), TRAIP (antigen: Ac-CTSSLANQPRLEDFLK-OH, New England Peptide), Polθ (antigen: residues 1212 to 1506, Abgent), and RAD51 (Long et al., 2011) were performed as described previously (Budzowska et al., 2015). Briefly, Protein A Sepharose Fast Flow beads (GE Healthcare) were incubated with antibodies at 4°C overnight. For mock depletion, an equivalent quantity of nonspecific rabbit IgGs was used. Five volumes of pre-cleared HSS or NPE were then mixed with one volume of the antibody-bound sepharose beads. For FANCI-D2 depletion of HSS and NPE, two rounds of depletion using both FANCI and FANCD2 antibodies were performed at room temperature for 20 minutes each. Depletions for other proteins were performed at 4°C, with two rounds for HSS and three rounds for NPE. For each round, a mixture of antibody-bound beads and egg extract was rotated on a wheel for 40 minutes. Immunodepleted extracts were collected and

used immediately for DNA replication. Depletion efficiency was assessed by Western blotting. Western blots from depletion or plasmid/sperm chromatin pull-downs were probed using antibodies against SMC2, TRAIP, FANCI (Duxin et al., 2014), FANCD2 (Knipscheer et al., 2009), MCM7 (Dewar et al., 2017), MCM6 (Dewar et al., 2017), RAD51 (Long et al., 2011), ORC2 (Dewar et al., 2017), CDC45 (Walter and Newport, 2000), SLD5 (Dewar et al., 2017), CHK1-pS345 (Cell Signaling Technology Cat #2348S), γ-H2AX (Cell Signaling Technology Cat #2577S) and Histone H3 (Cell Signaling Technology Cat #9715S).

Sperm chromatin spin-down assay. Sperm chromatin spin-down was performed as previously described (Raschle et al., 2015). Briefly, chromatin and associated proteins were isolated by centrifugation through a sucrose cushion, washed three times, resuspended in 2x SDS sample buffer (100 mM Tris pH 6.8, 4% SDS, 0.2% bromophenol blue, 20% glycerol, 10% β-mercaptoethanol) and boiled at 95°C for 3-5 minutes. In Figure S3A, chromatin was spun down 20 minutes after NPE addition for the Buffer control and at 9 minutes after NPE addition for the B1-CDK1 treatment (final concentration, 16.7 ng/μL), at which point replication was ~50% complete for both reactions. In Figure S1D, chromatin and associated proteins were isolated from HSS.

Plasmid pull-down assay. Plasmid pull-down assays were performed as described (Budzowska et al., 2015). Briefly, streptavidin-coupled magnetic beads (Dynabeads M-280, Invitrogen; 6 μl beads slurry per pull-down) were washed three times with wash buffer 1 (50 mM Tris pH 7.5, 150 mM NaCl, 1 mM EDTA pH 8, 0.02% Tween-20).

Biotinylated LacR was incubated with the beads (12 pmol per 6 µL beads) at room temperature for 40 min. The beads were then washed four times with pull-down buffer 1 (10 mM Hepes pH 7.7, 50 mM KCl, 2.5 mM MgCl2, 250 mM sucrose, 0.25 mg/mL BSA, 0.02% Tween-20) and resuspended in 40 µL of the same buffer. At the indicated times, 4 µL samples of the replication reaction were withdrawn and gently mixed with Biotin-LacR-coated beads. The suspension was immediately placed on a rotating wheel and incubated for 30-60 minutes at 4°C. The beads were washed three times with wash buffer 2 (10 mM Hepes pH 7.7, 50 mM KCl, 2.5 mM $MgCl_2$, 0.25 mg/mL BSA, 0.03% Tween-20). The beads were resuspended in 40 µL of 2× SDS sample buffer and boiled at 95°C for 3-5 minutes. Chromatin-bound proteins were separated by SDS-PAGE and analyzed by Western blotting.

De-ubiquitination assay Plasmid pull-downs were performed as described above, except that after the wash steps with wash buffer 2, chromatin-bound proteins were resuspended in 20 µL of USP21 buffer (150 mM NaCl, 10 mM DTT, 50mM Tris pH 7.5) and split into two 10 µL aliquots. Each aliquot was incubated with the non-specific deubiquitinase USP21 or buffer at 37ºC for 60 minutes. The reactions were stopped by addition of 2x SDS sample buffer and boiled at 95°C for 3-5 minutes.

Restriction digestion. 2 µL aliquots of replication reactions were stopped in 20 µL of stop solution B (50 mM Tris pH 7.5, 0.5% SDS, 25 mM EDTA), and replication products were purified as previously described (Raschle et al., 2008). Purified products were digested with restriction enzymes as *per* the manufacturer's instructions. Digestion

reactions were stopped in 0.5 volumes of stop solution C (5% SDS, 4 mg/mL Proteinase K) and incubated for 60 minutes at room temperature. Digested products were separated on a 1% native agarose gel and visualized by autoradiography.

Sequencing. LacR-bound p[*lacO*$_{48}$] plasmid was replicated in the presence of mitotic B1-CDK1 for 120 minutes. Replication products were purified and digested with AlwNI (single cut on the parental DNA) for 60 minutes at 37°C, as described above. After separation on a 0.9% native agarose gel, bands smaller than the 4.6 kb full-length linear fragment were extracted and self-ligated with T4 DNA ligase. The ligation products were transformed into *E.coli* DH5α or XL1-Gold. As a control, p[*lacO*$_{48}$] was replicated without LacR for 120 minutes in the presence of B1-CDK1. Replication products (containing only open circular and supercoiled species) were processed as above, and the only band (4.6 kb) after AlwNI restriction was purified for cloning. Clones from both treatments were sequenced by Sanger method with Forward primer: 5'-AAGGCGATTAAGTTGGGTAA-3' and Reverse primer: 5'-CATGTTCTTTCCTGCGTTATCCCCTGA-3'.

***C. elegans* maintenance**. The *C. elegans* strains were maintained according to standard procedures (Brenner, 1974) and were grown on 'Nematode Growth Medium' (NGM: 3 g/l NaCl; 2.5 g/l peptone; 20 g/l agar; 5 mg/l cholesterol; 1 mM $CaCl_2$; 1 mM $MgSO_4$; 2.7 g/l KH_2PO_4; 0.89 g/l K_2HPO_4). The following worm strains were used:

KAL1: *psf-1(lab1[gfp::TEV::S-tag::psf-1 + loxP unc-119(+) loxP])*

KAL3: *psf-1(lab1); ltIs37[pie-1p::mCherry::his-58 + unc-119(+)]*

TG1754: *unc-119(ed3) III; gtIs65[pie-1p::gfp::cdc-45 + unc-119(+)]; ltIs37*

***RNA* interference.** RNAi was performed by feeding worms with RNAse III-deficient HT115 bacteria transformed with an L4440-derived plasmid that express double-stranded RNA (Timmons and Fire, 1998). For microscopy experiments, bacterial culture grown to OD600=1 was supplemented with 1mM IPTG to express dsRNA. 400 ml of bacteria were loaded onto a 6cm RNAi plates (3 g/l NaCl, 20 g/l agarose, 5 mg/l cholesterol, 1 mM $CaCl_2$, 1 mM $MgSO_4$, 2.7 g/l KH_2PO_4, 0.89 g/l K_2HPO_4, 1 mM IPTG and 100 mg/l Ampicillin) and the plate was incubated overnight at room temperature. For each immunoprecipitation, 0.5 ml of bacterial pre-culture grown overnight was used to inoculate a 400 ml culture in 'Terrific Broth' (12 g l−1 tryptone, 24 g l−1 yeast extract, 9.4 g l−1 K2HPO4, 2.2 g l−1 KH2PO4, adjusted to pH 7). After 7 h of growth in a baffled flask at 37 °C with agitation, expression of dsRNA was induced overnight at 20 °C by addition of 3 mM IPTG and the bacteria were pelleted. 8 g of bacterial pellet was resuspended with 2 ml buffer (M9 medium supplemented with 75 mg l−1 cholesterol; 100 mg l−1 ampicillin; 50 mg l−1 tetracycline; 12.5 mg l−1 amphotericin B; 3 mM IPTG) and spread on a 15cm plate containing NGM supplemented with 1 mM IPTG and 100 mg l−1 ampicillin.

The plasmids expressing dsRNA were made by cloning PCR products amplified from cDNA into the vector L4440. *lrr-1* fragment was obtained with the primers ATGCGATTACCATGTGAAGTGG and CCTCGTGTGTGTATTCGATATTATC; *npl-4* fragment with GTCCAAAAGGGCCCAACTGTC and CCAGCAGGAACATCCACCAGC; *B0432.13* (*trul-1*) with ATGACGTCACAGCCCACGTCATC and CGTATTCCGTAAGATTCGACGTA. To target *lrr-1* and *B0432.13* simultaneously, DNA

fragments from each gene were cloned contigously into a single L4440 plasmid. The empty L4440 plasmid was used as control.

Microscopy. Worms at the larval L4 stage were incubated on 6 cm RNAi feeding plates for 30-34 hours at 25°C. Embryos were dissected in M9 medium (6 g/l Na_2HPO_4, 3 g/l KH_2PO_4, 5 g/l NaCl, 0.25 g/l $MgSO_4$) and mounted on a 2% agarose pad. Time lapse images were then recorded at 23–24°C using an Olympus IX81 microscope (MAG Biosystems) with a CSU-X1 spinning-disk confocal imager (Yokogawa Electric Corporation), a Cascade II camera (Photometrics) and a 60X/1.40 Plan Apochromat oil immersion lens (Olympus). Images were captured every 10 seconds using MetaMorph software (Molecular Devices) and processed with ImageJ software (National Institutes of Health) as previously described (Sonneville et al., 2017).

Extracts of worm embryos and immunoprecipitation of protein complexes. Preparation of worm extracts and immunoprecipitation of GFP-PSF-1 was performed as previously described (Sonneville et al., 2017). Briefly, 1 ml of a synchronized population of L4 worms expressing GFP-PSF-1 were fed for 50 h at 20 °C on a 15 cm RNAi plate, supplemented with 8 g of bacterial pellet (see above). After feeding, the worms were washed in M9 medium and then disrupted in 'bleaching solution' (for 100 ml: 36.5 ml H2O, 45.5 ml 2 N NaOH and 18 ml ClNaO 4%), before washing of the resulting embryo preparation in M9 medium.

At 4 °C, embryos were washed twice with lysis buffer (100 mM HEPES-KOH pH 7.9, 50 mM potassium acetate, 10 mM magnesium acetate, 2 mM EDTA), and then resuspended in three volumes of lysis buffer that was supplemented with 2 mM sodium

fluoride, 2 mM sodium β-glycerophosphate pentahydrate, 1 mM dithiothreitol (DTT), 1% Protease Inhibitor Cocktail (P8215, Sigma-Aldrich), and 1× 'Complete Protease Inhibitor Cocktail' (05056489001, Roche). The washed embryo suspension was then snap frozen drop-wise in liquid nitrogen and stored at −80 °C. Subsequently, ~2.5 g of frozen embryos was ground in a SPEX SamplePrep 6780 Freezer/Mill. After thawing, we added a one-quarter volume of 'glycerol-mix' buffer (lysis buffer supplemented with 50% glycerol, 300 mM potassium acetate, 0.5% detergent IGEPAL CA-630, protease inhibitors, and DTT at the concentrations mentioned above). De-ubiquitylase enzymes were inhibited by addition of 5 µM propargylated ubiquitin (Ubi-PrG; MRC PPU, Dundee), and chromosomal DNA was digested with 1,600 U of Pierce Universal Nuclease (123991963, Fisher) for 30 min at 4 °C. Extracts were centrifuged at 25,000 x *g* for 30 min and then for 100,000 x *g* for 1 h, before pre-incubation with agarose beads (0.4 ml slurry) for 45 min. Samples of each extract were taken and combined with Laemmli buffer, before storage at −80 °C. The remainder was then incubated for 90 min with 40 µl of GFP-Trap_A beads (Chromotek). The beads were washed four times with 1 ml of wash buffer (100 mM HEPES-KOH pH 7.9, 100 mM potassium acetate, 10 mM magnesium acetate, 2 mM EDTA, 0.1% IGEPAL CA-630, 2 mM sodium fluoride, 2 mM sodium β-glycerophosphate pentahydrate, plus protease inhibitors as above). Finally, the bound proteins were eluted at 95 °C for 5 min in 100 µl of 1× Laemmli buffer and stored at −80 °C.

Data quantification. Autoradiographs and Western blots were quantified using ImageJ 1.48v (National Institute of Health). The quantification methods for individual results are described in the figure legends.

1184

SUPPLEMENTAL FIGURE LEGENDS

Figure S1, related to Figure 1.

(**A**) To determine the concentration of mitotic B1-CDK1 that efficiently induces nuclear envelope breakdown and chromatin condensation, de-membranated *Xenopus* sperm chromatin was incubated in LSS (low speed supernatant) for 40 minutes to allow the formation of pseudo nuclei. The indicated final concentrations of B1-CDK1 were then added into the reactions for 30 minutes before Hoechst staining and imaging. 50 ng/μL of B1-CDK1 was sufficient to induce nuclear envelope breakdown and chromatin condensation and it was used for subsequent experiments unless otherwise indicated. Scale bar, 10 μm.

(**B**) Percentage of intact nuclei remaining at the indicated time points after treatment with the indicated concentration of B1-CDK1 (n>1,000). The '0 minute' time point refers to Buffer or B1-CDK1 addition. The value at each time point was normalized to the value at 0 minute in each treatment.

(**C**) Chromatin condensation assay in membrane-free HSS. Sperm chromatin was incubated in HSS for 30 minutes, and then treated with 50 ng/μL of B1-CDK1 for 30 minutes followed by Hoechst staining and imaging. Scale bar, 10 μm.

(**D**) Sperm chromatin spin-down assays in HSS. Sperm chromatin was incubated with HSS for 30 minutes and treated with Buffer or 50 ng/μL of B1-CDK1 for another 30 minutes. Chromatin DNA was recovered and chromatin-bound proteins were blotted with indicated antibodies. Unrelated lanes were cropped as indicated by the gap.

(**E**) Plasmid pull-down assays in HSS. pBlueScript (3 kb) was incubated with HSS at a concentration of 7.5 ng/μL for 30 minutes and treated with Buffer or 50 ng/μL of B1-

CDK1 for another 30 minutes. Plasmid was recovered and chromatin-bound proteins were blotted with indicated antibodies. Unrelated lanes were cropped as indicated by the gap.

(**F**) Plasmid pull-down assay to assess origin firing. pBlueScript was incubated with HSS for 30 minutes and treated with buffer or 50 ng/μL of B1-CDK1 for another 30 minutes before addition of NPE. The p97 inhibitor NMS-873 (p97-i) was added into NPE (final concentration, 266 μM) and incubated for 15 minutes. Treatment of p97-i blocked the unloading of CMG helicases from chromatin and trapped ubiquitylated MCM7 on chromatin, seen as a smear. Right panel shows the quantification of the CDC45 and Histone H3 signals. Increased CDC45 loading with B1-CDK1 treatment suggested more origin firing.

(**G**) LacR-bound p[*lacO*$_{48}$] was replicated in interphase egg extracts for 60 minutes and then treated with DMSO or CDK1 kinase inhibitor (CDK1-i, 333 μM RO-3306) for 5 minutes before the addition of Buffer or 50 ng/μL of B1-CDK1. At the indicated times, samples were withdrawn and replication products were tracked by electrophoresis and autoradiography. ARP, aberrant replication product; θ, theta structure.

(**H**) LacR-bound p[*lacO*$_{48}$] was replicated in the presence of B1-CDK1, Cyclin A2 and cyclin E-CDK2, with a final concentration of 50 ng/μL, respectively. OC, open circle; SC, supercoil; θ, theta structure; ARP, aberrant replication product.

Figure S2, related to Figure 2.

(**A**) Model for mitotic processing of replication forks stalled by *lacO*-LacR barriers, explaining the restriction analysis (Figure 2B) and sequencing data (Figure 2D). After

replication fork stalling, B1-CDK1 induces fork collapse and double-strand breaks (DSBs) at the edges of the *lacO* array. The broken DNA ends, with certain number of *lacO* repeats or microhomology, lead to either intra- or inter-molecular end joining. Inter-molecular end joining generates the aberrant replication products (ARPs). The initial end joining products can also be subject to cycles of fork collapse and end joining. Outcomes other than those illustrated here are possible but may not be detected because our sequencing strategy depends on the ability to recover plasmids by cloning. Although it has not been addressed whether the leading or lagging strand templates break, the results on CMG unloading (see below and text for details) favor leading strand breakage.

(**B**) Schematic of B1-CDK1-induced fork breakage at different locations in the *lacO* array. Breakage at the outer edges (left) and joining of the resulting one-ended breaks creates large deletions of the array, whereas breakage closer to the midpoint of the array causes smaller deletions (right).

(**C**) Sequence and structure of the 48 *lacO* repeats in p[$lacO_{48}$]. Each *lacO* repeat is in italic. Unique spacer sequences between *lacO* repeats are labeled in red, green, purple and blue, respectively, as depicted in Figures 2D and 2E. The sequence in grey indicates a unique spacer in the middle of the *lacO* array. Sequencing primers used in Figure 2D are indicated.

Figure S3, related to Figure 3.

(**A**) B1-CDK1 treatment inhibits chromatin-loading of RAD51. Sperm chromatin was replicated in egg extracts and sampled when 50% replication was completed (20

minutes for Buffer and 9 minutes for B1-CDK1). To inhibit DNA replication, CDC7 inhibitor (CDC7-i, 399 μM of PHA-767491) was added to NPE and incubated for 15 minutes. Chromatin-bound proteins were recovered by chromatin spin-down and detected by blotting with indicated antibodies.

(**B**) Mock-depleted and RAD51-depleted egg extracts were blotted with RAD51 and MCM7 antibodies. Serial dilutions of mock-depletion were used to assess the level of RAD51 depletion. Arrowhead indicates RAD51.

(**C**) LacR-bound p[*lacO*$_{48}$] was replicated in mock-depleted or RAD51-depleted egg extracts in the absence or presence of B1-CDK1.

(**D**) pBlueScript was replicated in egg extracts with the indicated treatments. BRC peptide binds and blocks RAD51's interaction with BRCA2, which prevents HR-mediated DSB repair. BRC*** peptide harbors three mutations at RAD51 binding sites and is unable to inhibit RAD51 (Long et al., 2011).

(**E**) LacR-bound p[*lacO*$_{48}$] was replicated with the indicated treatments. To inhibit NHEJ, a DNA-PK inhibitor (DNA-PK-i, 133 μM NU-7441) was added to NPE.

(**F**) Quantification of overall DNA replication and ARP for Figure 3B.

(**G**) Quantification of overall DNA replication and ARP for Figure 3C.

(**H**) Structures of clones derived from mitotic ARPs in Polθ-depleted egg extracts (Exp. 1 in Figure 3E).

In (C-E), ARP, aberrant replication product; θ, theta structure; OC, open circle; SC, supercoil; RI, replication intermediate.

Figure S4, related to Figure 4.

(**A**) Mock-depleted and SMC2-depleted *Xenopus* egg extracts were blotted for SMC2 and MCM7 alongside a serial dilution of mock-depleted extracts.

(**B**) Effect of SMC2 depletion on B1-CDK1-induced chromatin condensation in HSS. Sperm chromatin was incubated in mock-depleted or SMC2-depleted HSS with Buffer or B1-CDK1 for 30 minutes prior to Hoechst staining and imaging. Regions with boxes were magnified on the right. Note the condensed chromosome in mock-depleted HSS with B1-CDK1 treatment (upper right image). Scale bar, 10 μm.

(**C**) LacR-bound p[*lacO*$_{48}$] was replicated in mock-depleted or condensin SMC2-depleted extracts with or without B1-CDK1 treatment.

(**D**) pBlueScript was replicated in mock-depleted or SMC2-depleted egg extracts with a low dose of aphidicolin in the absence or presence of B1-CDK1. The absence of SMC2 had no effect on mitotic ARP formation.

(**E**) A time course to relate the timing of CMG unloading to replication fork collapse and ARP formation during replication with B1-CDK1. LacR-bound p[*lacO*$_{48}$] was replicated in egg extracts for 30 minutes before the addition of Buffer or B1-CDK1. Plasmid pull-downs were performed from “cold” reactions lacking radio-labeled nucleotides in parallel with “hot” reactions containing [α-^{32}P]-dATP. Plasmid pull-down samples were blotted for indicated proteins. Replication products were detected by autoradiography after gel electrophoresis. The red bracket indicates ubiquitylated MCM7, which is detectable before the appearance of the ARP. The black bracket marks potential collapsed replication forks with the B1-CDK1 treatment.

(**F**) Effect of p97 inhibition on stalled replication forks in the presence or absence of B1-CDK1. LacR-bound p[*lacO*$_{48}$] plasmid was replicated in “hot” extracts with [α-^{32}P]-dATP

to track DNA replication products and in “cold” extracts without [α-^{32}P]-dATP for plasmid pull-down to track CHK1-S345 phosphorylation (CHK1-pS345), γ-H2AX. Histon H3 was included as loading control. The final concentration of p97-i was 266 μM.

(**G**) Quantification of ARP, OC+SC, and overall DNA replication during replication of pDPC in Figure 4C.

(**H**) Fork restart assay using IPTG to release LacR replication barrier. LacR-bound p[*lacO*$_{48}$] was replicated as schemed. The final concentration of IPTG was 10 mM. Note that IPTG had no effect on the B1-CDK1-induced ARP in the presence of DMSO (lanes 13-24), whereas it almost fully restarted DNA synthesis in the presence of p97-i (compare lanes 31-35 with 25-30, and 19-24).

In (C) (D), (F) and (H), RI, replication intermediate; ARP, aberrant replication product; OC, open circle; SC, supercoil; θ, theta structure.

Figure S5, related to Figure 5.

(**A**) LacR-bound p[*lacO*$_{48}$] was replicated and treated as schemed. Chromatin-bound proteins were recovered and blotted with the indicated antibodies. IPTG was used to release LacR from *lacO* array therefore induce replication termination. Cul-i was used to inhibit CRL2^{Lrr1}-dependent CMG ubiquitylation during interphase replication termination.

(**B**) pDPC was replicated in mock-depleted or TRAIP-depleted egg extracts in the presence or absence of B1-CDK1.

(**C**) Serial dilutions of NPE and rTRAIP^{WT} purified from *E. coli* were blotted with TRAIP and MCM7 antibodies. Arrowhead marks TRAIP signal and asterisk indicates a background band in NPE. The concentration of TRAIP in NPE is 3.0-4.5 ng/μL.

(**D-E**) LacR-bound p[*lacO*$_{48}$] (D) and pDPC (E) were replicated in mitotic mock-depleted or TRAIP-depleted egg extracts with or without rTRAIP^{WT} as indicated. rTRAIP^{WT} was added to NPE at endogenous level (3.6 ng/μL). Matched buffer was added to reactions without rTRAIP^{WT}.

(**F**) LacR-bound p[*lacO*$_{48}$] was replicated in TRAIP-depleted extracts supplemented with 6xHis-SUMO tagged rTRAIP of wildtype (WT) or truncation of PIP box (ΔPIP), as indicated. Both proteins were added ~5-10 folds of endogenous TRAIP in NPE and incubated for 15 minutes before they were used to drive DNA replication.

(**G**) Mock-depleted and FANCI-D2-double depleted egg extracts were blotted with indicated antibodies. Serial dilution of mock-depleted extract was used to assess the level of FANCI-D2 depletion.

(**H**) LacR-bound p[*lacO*$_{48}$] was replicated in mock-depleted or FANCI-D2-depleted egg extracts in the absence or presence of B1-CDK1. The depletion of FANCI-FANCD2 had no effect on ARP formation.

In (B), (D), (F) and (H), ARP, aberrant replication product; θ, theta structure; OC, open circle; SC, supercoil.

Figure S6, related to Figure 6.

(**A**) p[*lacO*$_{48}$], in the absence of LacR, was replicated in egg extracts used in Figures 6A and 6B. DNA replication was complete in 20 minutes. RI, replication intermediate; OC, open circle; SC, supercoil.

(**B**) A 3.1 kb plasmid (pJD152 in (Dewar et al., 2015)) was replicated in mock-depleted or TRAIP-depleted extracts in the presence or absence of p97-i (to trap terminated and

ubiquitylated CMGs on chromatin) followed by Buffer or B1-CDK1 treatment. Chromatin-bound proteins were recovered and blotted with indicated antibodies. Red brackets indicate the levels of MCM7 ubiquitylation. Note the dramatic smear of MCM7 ubiquitylation in the presence of B1-CDK1 in mock (compare lanes 6 and 2) and the shrinkage with TRAIP depletion (compare lanes 14 and 6).

(**C**) LacR-bound p[*lacO*$_{48}$] plasmid was replicated in mock-depleted or TRAIP-depleted egg extracts with or without recombinant rTRAIP^{WT} (~4-fold of endogenous TRAIP), or rTRAIP^{R18C} (~9-fold of endogenous TRAIP), and treated as schemed. Chromatin-bound proteins were recovered and blotted with the indicated antibodies.

(**D**) Worm embryos expressing GFP-CDC-45 and mCherry-HistoneH2B were subjected to the indicated RNAi treatment. The images correspond to metaphase of the first embryonic cell cycle, and the arrows indicate persistence of GFP-CDC-45 on condensed chromatin. Scale bar, 5 μm.

(**E**) Comparison of different CMG unloading pathways. Mitotic CMG unloading at single stalled fork (i) occurs when a single stalled CMG on ssDNA enters mitosis (or in environment with high mitotic CDK activity). TRAIP is activated by mitotic CDK to trigger CMG ubiquitylation. Mitotic termination (ii) occurs when CRL2^{Lrr1} is deficient (Sonneville et al., 2017). CMGs at terminated replication forks are ubiquitylated upon mitotic entry in a TRAIP-dependent manner. During interphase ICL repair (iii) (Wu et al., in revision), when two CMGs on ssDNA converge at ICL, TRAIP is activated, independent of CDK1 activity (data not shown) and promotes CMG ubiquitylation. During replication termination in interphase (iv), two CMGs bypass each other and translocate from ssDNA to dsDNA, triggering CRL2^{Lrr1}-dependent CMG ubiquitylation (Dewar et al.,

2015; Dewar et al., 2017; Sonneville et al., 2017). The cartoons highlight the requirement of E3 ubiquitin ligase activity rather than physical localization for CMG ubiquitylation. In contrast to $CRL2^{Lrr1}$ which is specifically recruited to replisome during interphase replication termination, TRAIP may travel with the replisome.

Figure S7. Related to Figure 7

When replication forks stall on either side of a hard-to-replicate region (e.g. a common fragile site), entry into mitosis causes CMG unloading and efficient fork breakage. Because CMG binds the leading strand template, we propose that CMG unloading leads to breakage of both stalled forks on the leading strand templates (left pathway). One intact sister chromatid is rapidly restored by gap filling (dashed blue line). The other chromatid is restored by alternative end joining of the two broken ends, yielding sister chromatid exchange and a deletion that encompasses the segment of unreplicated DNA. Template switching before end joining could generate duplications at the breakpoint. In contrast, if stalled forks are broken randomly (right pathway), unproductive outcomes will be frequent, including the formation of acentric and dicentric isochromosomes (shown). Furthermore, if only one fork is broken, acentric arms can be generated (not shown).

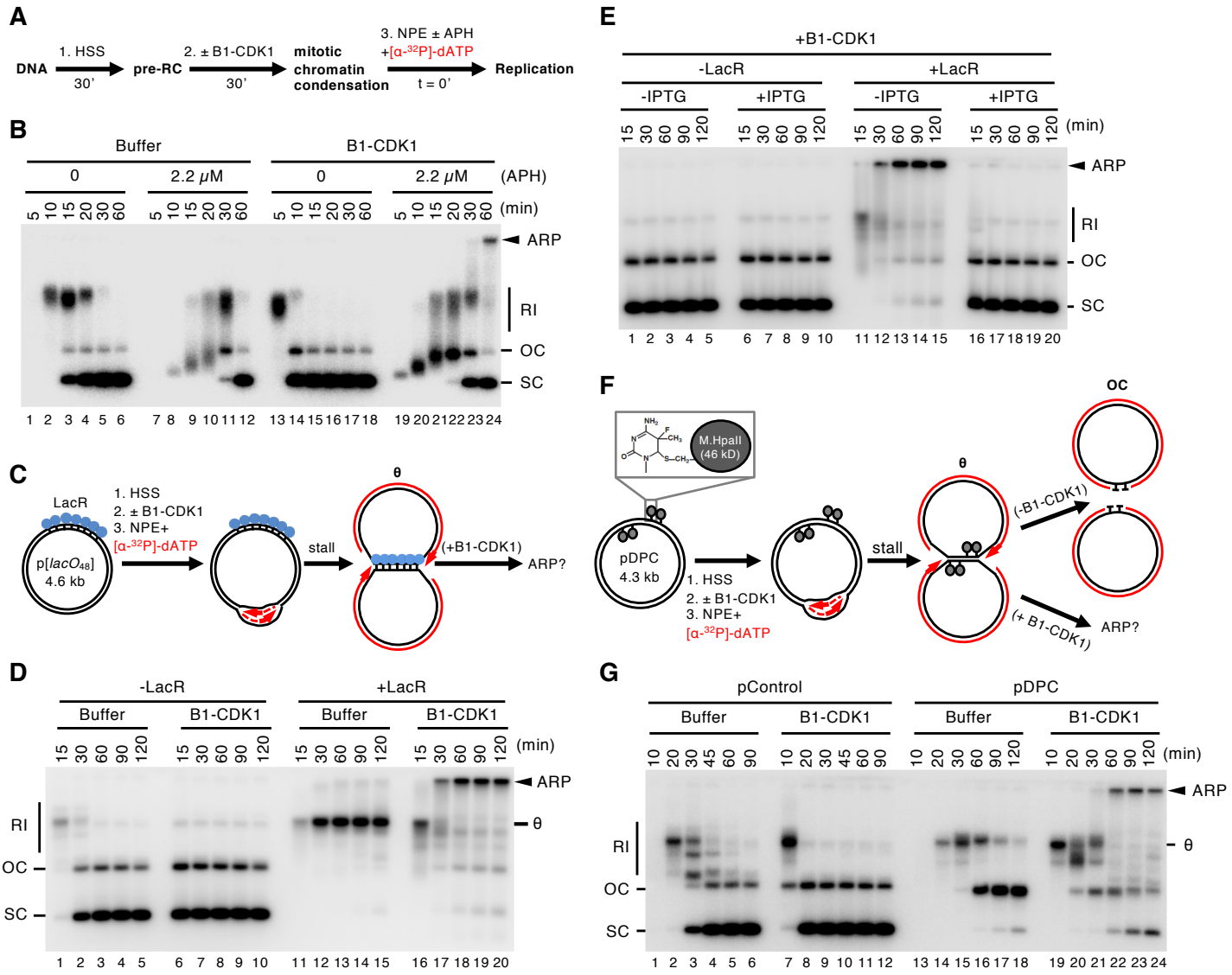
A
DNA
1. HSS
30'
pre-RC
2. ± B1-CDK1
30'
mitotic chromatin condensation
3. NPE ± APH
+[α-32P]-dATP
t = 0'
Replication
B
Buffer
B1-CDK1
0
2.2 μM
(APH)
(min)
ARP
RI
OC
SC
C
LacR
p[lacO48]
4.6 kb
1. HSS
2. ± B1-CDK1
3. NPE+
[α-32P]-dATP
stall
θ
(+B1-CDK1)
ARP?
D
-LacR
+LacR
Buffer
B1-CDK1
(min)
ARP
RI
θ
OC
SC
E
+B1-CDK1
-LacR
+LacR
-IPTG
+IPTG
(min)
ARP
RI
OC
SC
F
M.HpaII
(46 kD)
pDPC
4.3 kb
1. HSS
2. ± B1-CDK1
3. NPE+
[α-32P]-dATP
stall
θ
OC
(-B1-CDK1)
(+ B1-CDK1)
ARP?
G
pControl
pDPC
Buffer
B1-CDK1
(min)
ARP
RI
θ
OC
SC

Figure 1

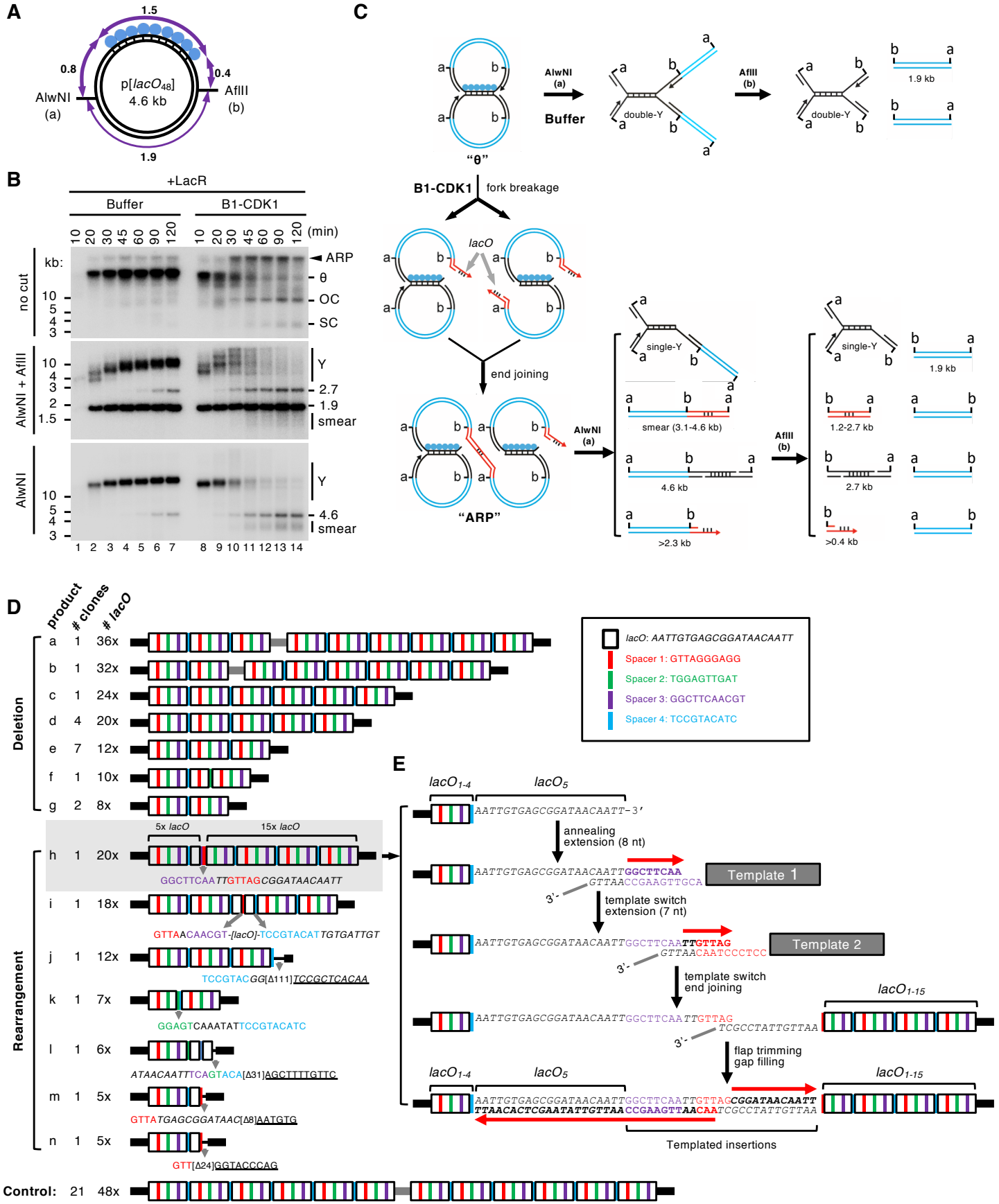
A
1.5
0.8
0.4
AlwNI
(a)
p[lacO48]
4.6 kb
AflII
(b)
1.9
B
+LacR
Buffer
B1-CDK1
10 20 30 45 60 90 120 10 20 30 45 60 90 120 (min)
kb:
no cut
AlwNI + AflII
AlwNI
ARP
θ
OC
SC
Y
2.7
1.9
smear
4.6
1 2 3 4 5 6 7 8 9 10 11 12 13 14
C
"θ"
AlwNI (a)
Buffer
double-Y
AflII (b)
1.9 kb
B1-CDK1
fork breakage
lacO
end joining
"ARP"
single-Y
smear (3.1-4.6 kb)
4.6 kb
>2.3 kb
1.2-2.7 kb
2.7 kb
>0.4 kb
D
product
clones
lacO
Deletion
a 1 36x
b 1 32x
c 1 24x
d 4 20x
e 7 12x
f 1 10x
g 2 8x
Rearrangement
h 1 20x
5x lacO
15x lacO
GGCTTCAATTGTTAGCGGATAACAATT
i 1 18x
GTTAACAACGT-[lacO]-TCCGTACATTGTGATTGT
j 1 12x
TCCGTACGG[Δ111]TCCGCTCACAA
k 1 7x
GGAGTCAAATATTCCGTACATC
l 1 6x
ATAACAATTTCAGTACA[Δ31]AGCTTTTGTTC
m 1 5x
GTTATGAGCGGATAAC[Δ8]AATGTG
n 1 5x
GTT[Δ24]GGTACCCAG
Control: 21 48x
lacO: AATTGTGAGCGGATAACAATT
Spacer 1: GTTAGGGAGG
Spacer 2: TGGAGTTGAT
Spacer 3: GGCTTCAACGT
Spacer 4: TCCGTACATC
E
lacO1-4
lacO5
AATTGTGAGCGGATAACAATT-3'
annealing
extension (8 nt)
AATTGTGAGCGGATAACAATTGGCTTCAA
GTTAACCGAAGTTGCA
Template 1
template switch
extension (7 nt)
AATTGTGAGCGGATAACAATTGGCTTCAATTGTTAG
GTTAACAATCCCTCC
Template 2
template switch
end joining
lacO1-15
AATTGTGAGCGGATAACAATTGGCTTCAATTGTTAG
TCGCCTATTGTTAA
flap trimming
gap filling
AATTGTGAGCGGATAACAATTGGCTTCAATTGTTAGCGGATAACAATT
TTAACACTCGAATATTGTTAACCGAAGTTAACAATCGCCTATTGTTAA
Templated insertions

Figure 2

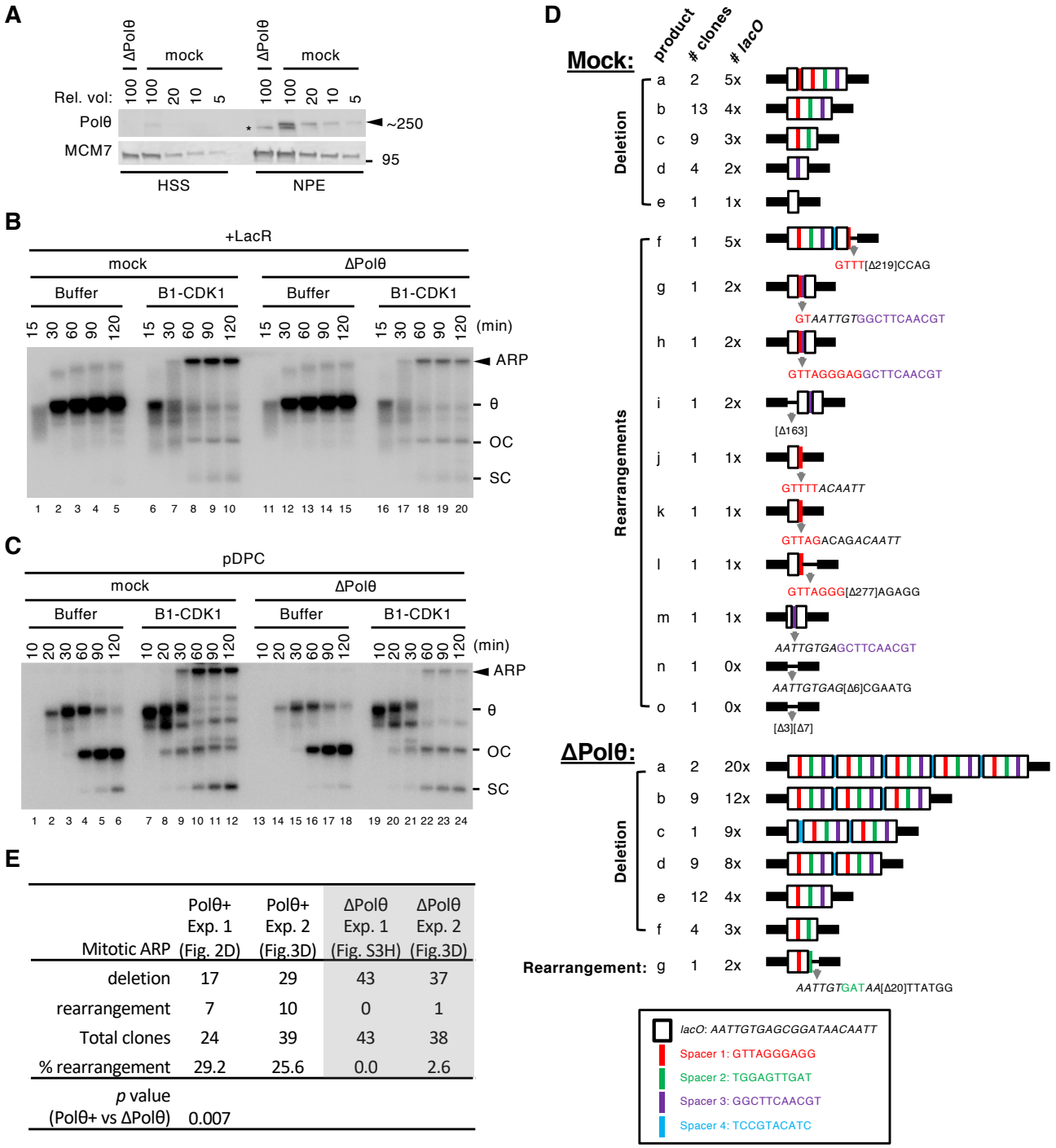

E

Mitotic ARP	Polθ+ Exp. 1 (Fig. 2D)	Polθ+ Exp. 2 (Fig.3D)	ΔPolθ Exp. 1 (Fig. S3H)	ΔPolθ Exp. 2 (Fig.3D)
deletion	17	29	43	37
rearrangement	7	10	0	1
Total clones	24	39	43	38
% rearrangement	29.2	25.6	0.0	2.6
p value (Polθ+ vs ΔPolθ)	0.007			

Figure 3

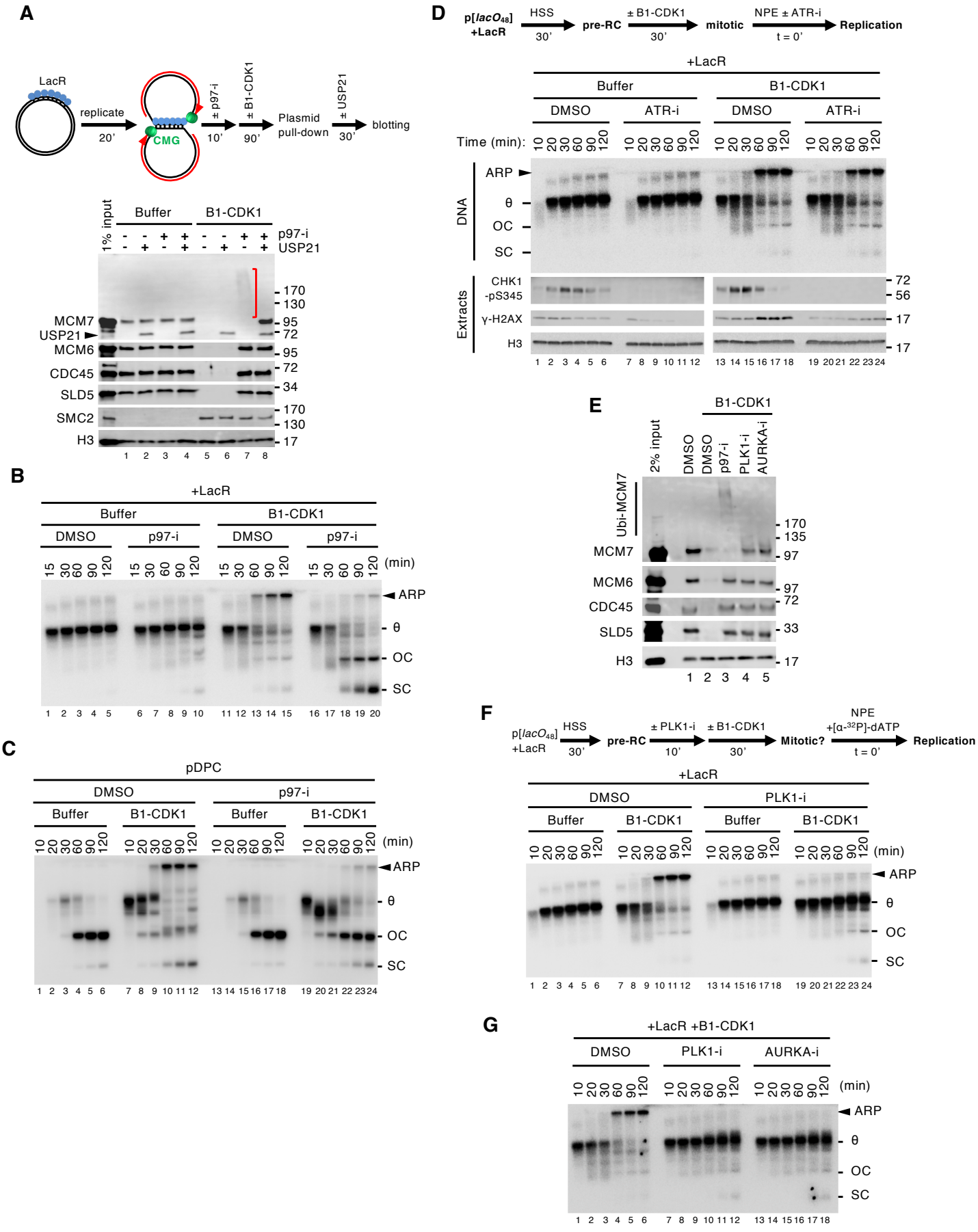
A
LacR
replicate
20'
CMG
± p97-i
10'
± B1-CDK1
90'
Plasmid pull-down
± USP21
30'
blotting
1% input
Buffer
B1-CDK1
p97-i
USP21
MCM7
USP21
MCM6
CDC45
SLD5
SMC2
H3
170
130
95
72
95
72
34
170
130
17
1 2 3 4 5 6 7 8
B
+LacR
Buffer
B1-CDK1
DMSO
p97-i
DMSO
p97-i
15 30 60 90 120 15 30 60 90 120 15 30 60 90 120 15 30 60 90 120
(min)
ARP
θ
OC
SC
1 2 3 4 5 6 7 8 9 10 11 12 13 14 15 16 17 18 19 20
C
pDPC
DMSO
p97-i
Buffer
B1-CDK1
Buffer
B1-CDK1
10 20 30 60 90 120 10 20 30 60 90 120 10 20 30 60 90 120 10 20 30 60 90 120
(min)
ARP
θ
OC
SC
1 2 3 4 5 6 7 8 9 10 11 12 13 14 15 16 17 18 19 20 21 22 23 24
D
p[lacO48] +LacR
HSS
30'
pre-RC
± B1-CDK1
30'
mitotic
NPE ± ATR-i
t = 0'
Replication
+LacR
Buffer
B1-CDK1
DMSO
ATR-i
DMSO
ATR-i
Time (min):
10 20 30 60 90 120 10 20 30 60 90 120 10 20 30 60 90 120 10 20 30 60 90 120
DNA
ARP
θ
OC
SC
Extracts
CHK1 -pS345
γ-H2AX
H3
72
56
17
17
1 2 3 4 5 6 7 8 9 10 11 12 13 14 15 16 17 18 19 20 21 22 23 24
E
B1-CDK1
2% input
DMSO
DMSO
p97-i
PLK1-i
AURKA-i
Ubi-MCM7
MCM7
MCM6
CDC45
SLD5
H3
170
135
97
97
72
33
17
1 2 3 4 5
F
p[lacO48] +LacR
HSS
30'
pre-RC
± PLK1-i
10'
± B1-CDK1
30'
Mitotic?
NPE +[α-32P]-dATP
t = 0'
Replication
+LacR
DMSO
PLK1-i
Buffer
B1-CDK1
Buffer
B1-CDK1
10 20 30 60 90 120 10 20 30 60 90 120 10 20 30 60 90 120 10 20 30 60 90 120
(min)
ARP
θ
OC
SC
1 2 3 4 5 6 7 8 9 10 11 12 13 14 15 16 17 18 19 20 21 22 23 24
G
+LacR +B1-CDK1
DMSO
PLK1-i
AURKA-i
10 20 30 60 90 120 10 20 30 60 90 120 10 20 30 60 90 120
(min)
ARP
θ
OC
SC
1 2 3 4 5 6 7 8 9 10 11 12 13 14 15 16 17 18

Figure 4

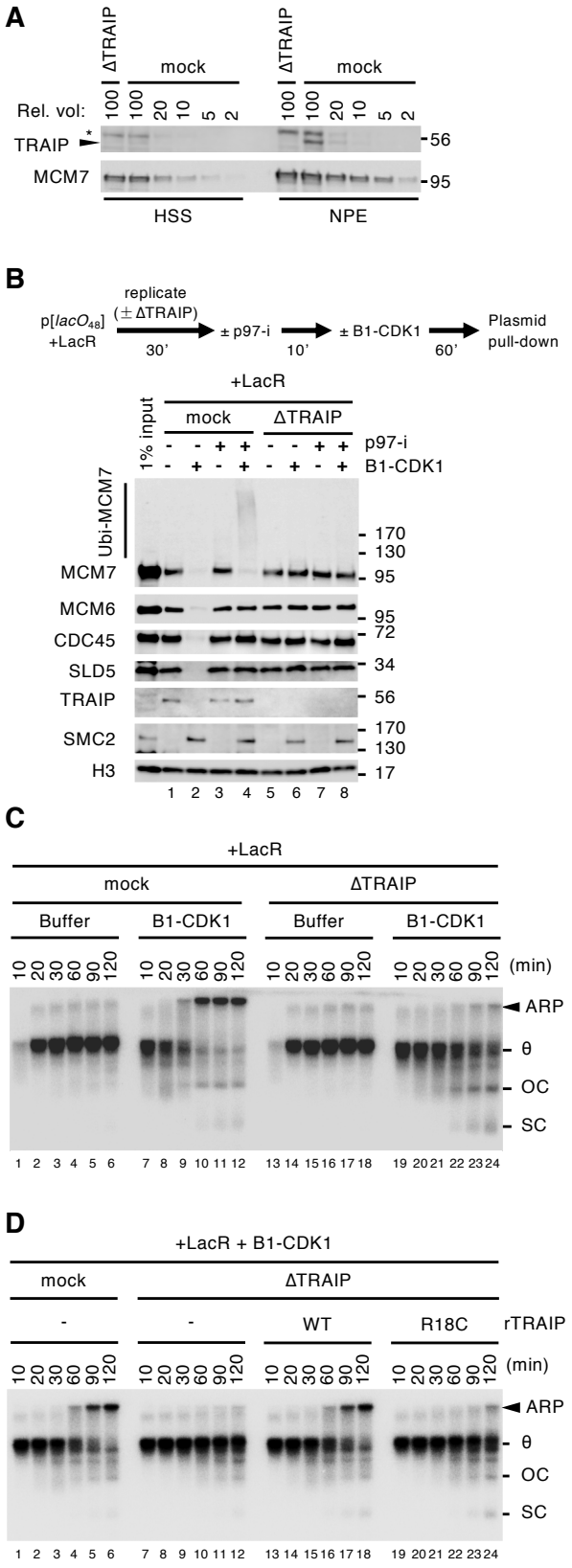
A
ΔTRAIP
mock
Rel. vol:
100
20
10
5
2
TRAIP
MCM7
56
95
HSS
NPE
B
p[lacO48]
+LacR
replicate
(± ΔTRAIP)
30'
± p97-i
10'
± B1-CDK1
60'
Plasmid
pull-down
+LacR
1% input
p97-i
B1-CDK1
Ubi-MCM7
MCM7
MCM6
CDC45
SLD5
TRAIP
SMC2
H3
170
130
95
72
34
17
1 2 3 4 5 6 7 8
C
+LacR
Buffer
B1-CDK1
(min)
ARP
θ
OC
SC
1 2 3 4 5 6 7 8 9 10 11 12 13 14 15 16 17 18 19 20 21 22 23 24
D
+LacR + B1-CDK1
WT
R18C
rTRAIP
ARP
θ
OC
SC
1 2 3 4 5 6 7 8 9 10 11 12 13 14 15 16 17 18 19 20 21 22 23 24

Figure 5

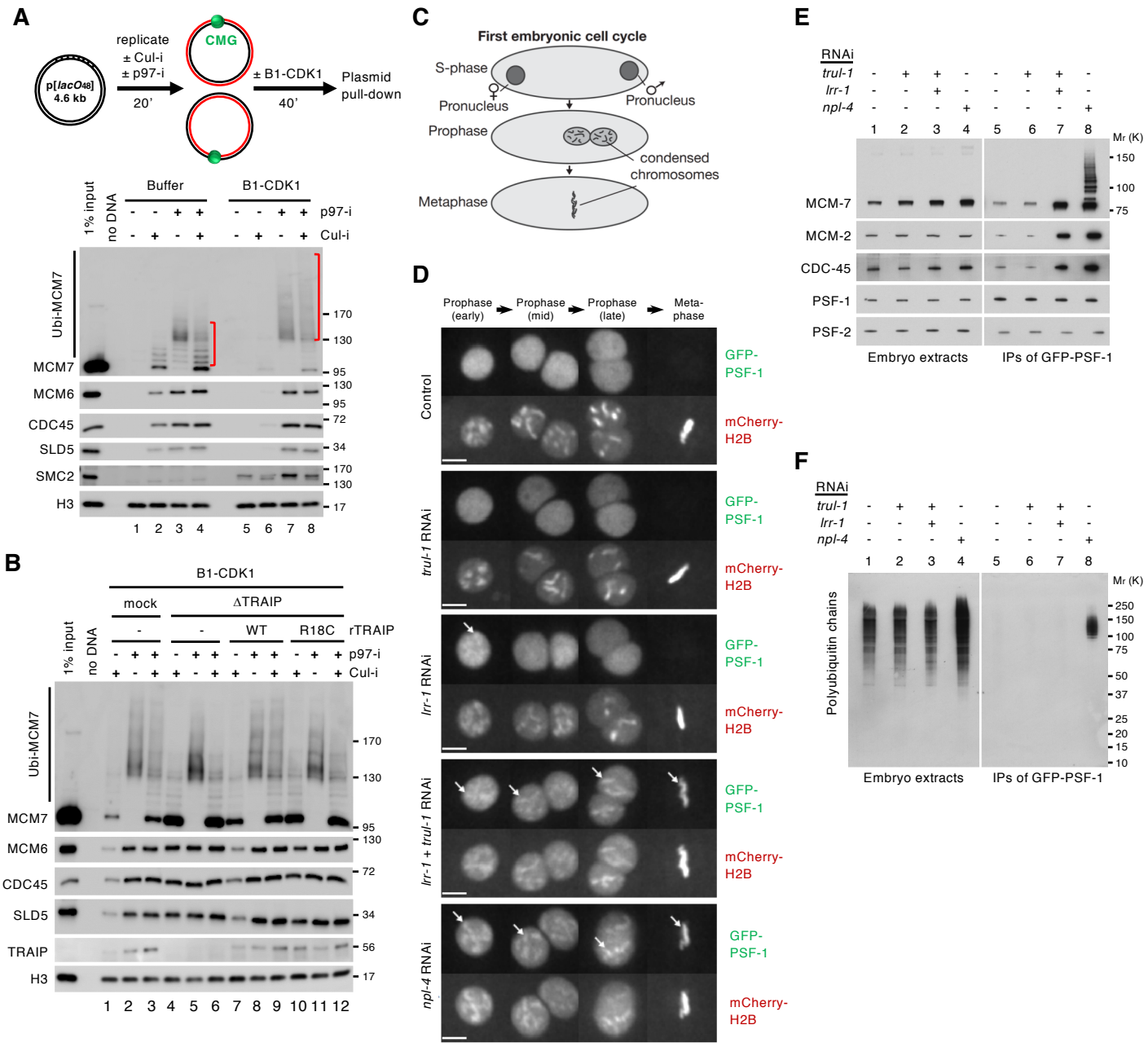
A
p[lacO48] 4.6 kb
replicate
± Cul-i
± p97-i
20'
CMG
± B1-CDK1
40'
Plasmid pull-down
1% input
no DNA
Buffer
B1-CDK1
p97-i
Cul-i
Ubi-MCM7
MCM7
MCM6
CDC45
SLD5
SMC2
H3
170
130
95
72
34
56
17
1 2 3 4 5 6 7 8
B
B1-CDK1
mock
ΔTRAIP
WT
R18C
rTRAIP
MCM7
MCM6
CDC45
SLD5
TRAIP
H3
1 2 3 4 5 6 7 8 9 10 11 12
C
First embryonic cell cycle
S-phase
Pronucleus
Prophase
condensed chromosomes
Metaphase
D
Prophase (early)
Prophase (mid)
Prophase (late)
Meta-phase
Control
trul-1 RNAi
lrr-1 RNAi
lrr-1 + trul-1 RNAi
npl-4 RNAi
GFP-PSF-1
mCherry-H2B
E
RNAi
trul-1
lrr-1
npl-4
MCM-7
MCM-2
CDC-45
PSF-1
PSF-2
Mr (K)
150
100
75
Embryo extracts
IPs of GFP-PSF-1
F
Polyubiquitin chains
250
150
100
75
50
37
25
20
15
10

Figure 6

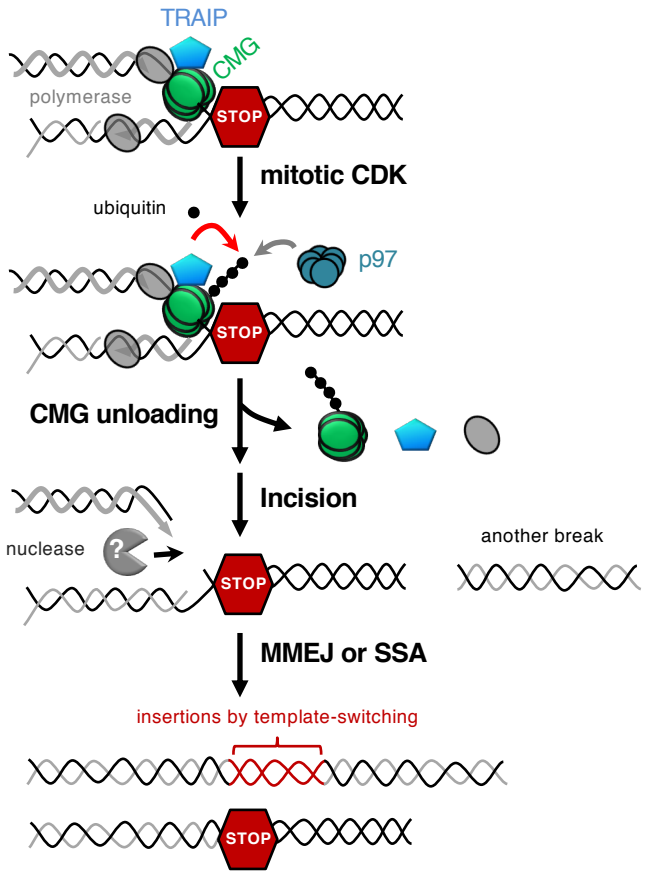
TRAIP
CMG
polymerase
STOP
mitotic CDK
ubiquitin
p97
STOP
CMG unloading
Incision
nuclease
?
STOP
another break
MMEJ or SSA
insertions by template-switching
STOP

Figure 7

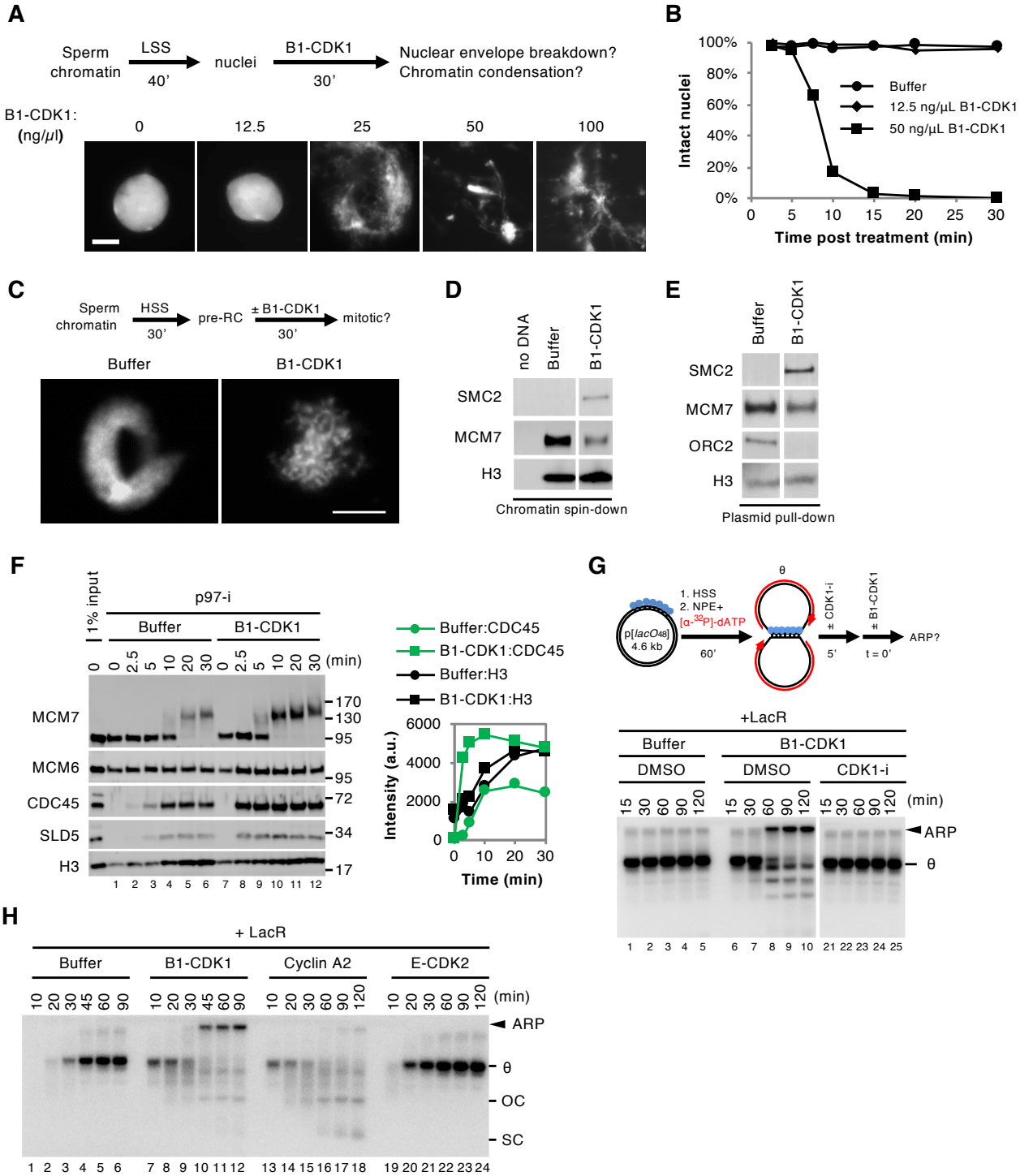
A
Sperm chromatin
LSS
40'
nuclei
B1-CDK1
30'
Nuclear envelope breakdown?
Chromatin condensation?
B1-CDK1: (ng/μl)
0
12.5
25
50
100
B
Intact nuclei
100%
80%
60%
40%
20%
0%
0
5
10
15
20
25
30
Time post treatment (min)
Buffer
12.5 ng/μL B1-CDK1
50 ng/μL B1-CDK1
C
Sperm chromatin
HSS
30'
pre-RC
± B1-CDK1
30'
mitotic?
Buffer
B1-CDK1
D
no DNA
Buffer
B1-CDK1
SMC2
MCM7
H3
Chromatin spin-down
E
Buffer
B1-CDK1
SMC2
MCM7
ORC2
H3
Plasmid pull-down
F
1% input
p97-i
Buffer
B1-CDK1
0 0 2.5 5 10 20 30 0 2.5 5 10 20 30 (min)
MCM7
MCM6
CDC45
SLD5
H3
170
130
95
95
72
34
17
1 2 3 4 5 6 7 8 9 10 11 12
Buffer:CDC45
B1-CDK1:CDC45
Buffer:H3
B1-CDK1:H3
Intensity (a.u.)
6000
4000
2000
0
0 10 20 30
Time (min)
G
θ
1. HSS
2. NPE+
[α-32P]-dATP
p[lacO48] 4.6 kb
60'
± CDK1-i
5'
± B1-CDK1
t = 0'
ARP?
+LacR
Buffer
B1-CDK1
DMSO
DMSO
CDK1-i
15 30 60 90 120 15 30 60 90 120 15 30 60 90 120 (min)
ARP
θ
1 2 3 4 5 6 7 8 9 10 21 22 23 24 25
H
+ LacR
Buffer
B1-CDK1
Cyclin A2
E-CDK2
10 20 30 45 60 90 10 20 30 45 60 90 10 20 30 60 90 120 10 20 30 60 90 120 (min)
ARP
θ
OC
SC
1 2 3 4 5 6 7 8 9 10 11 12 13 14 15 16 17 18 19 20 21 22 23 24

Figure S1

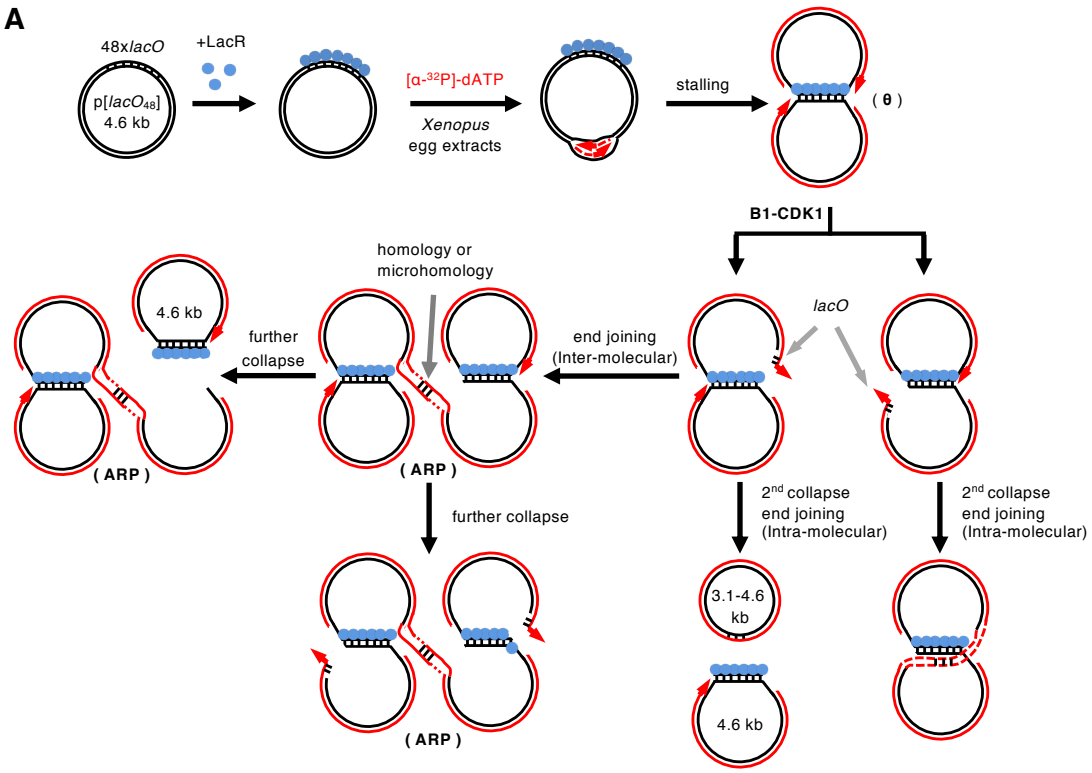

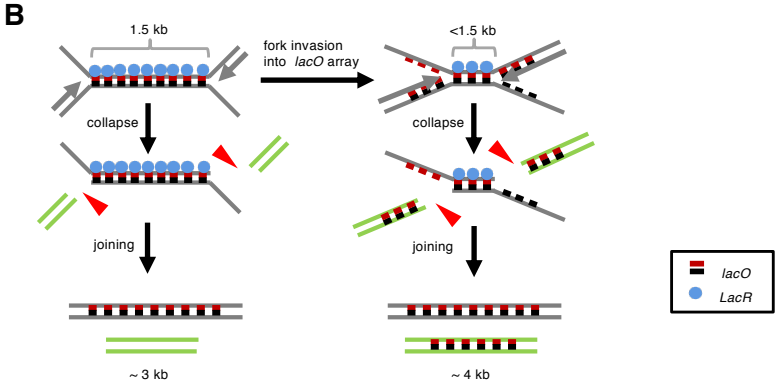

C

Forward primer

AAGGCGATTAAGTTGGGTAACGCCAGGGTTTTCCCAGTCACGACGTTGTAAAACGACGGCCAGTGAGCGCGCGTAATACGACTCACTA

TAGGGCGAATTGGAGCTCTCACACCTACAAGGGATGTACATC*AATTGTGAGCGGATAACAATT*GTTAGGGAGG*AATTGTGAGCGGATAACAATT*TGGAGTTGAT*AATTGTGAGCGGATAACAATT*

GGCTTCAACGT*AATTGTGAGCGGATAACAATT*TCCGTACATC*AATTGTGAGCGGATAACAATT*GTTAGGGAGG*AATTGTGAGCGGATAACAATT*TGGAGTTGAT*AATTGTGAGCGGATAACAATT*

GGCTTCAACGT*AATTGTGAGCGGATAACAATT*TCCGTACATC*AATTGTGAGCGGATAACAATT*GTTAGGGAGG*AATTGTGAGCGGATAACAATT*TGGAGTTGAT*AATTGTGAGCGGATAACAATT*

GGCTTCAACGT*AATTGTGAGCGGATAACAATT*TCCGTACATC*AATTGTGAGCGGATAACAATT*GTTAGGGAGG*AATTGTGAGCGGATAACAATT*TGGAGTTGAT*AATTGTGAGCGGATAACAATT*

GGCTTCAACGT*AATTGTGAGCGGATAACAATT*TCCGTACATC*AATTGTGAGCGGATAACAATT*GTTAGGGAGG*AATTGTGAGCGGATAACAATT*TGGAGTTGAT*AATTGTGAGCGGATAACAATT*

GGCTTCAACGT*AATTGTGAGCGGATAACAATT*TCCGTACATC*AATTGTGAGCGGATAACAATT*GTTAGGGAGG*AATTGTGAGCGGATAACAATT*TGGAGTTGAT*AATTGTGAGCGGATAACAATT*

GGCTTCAACGT*AATTGTGAGCGGATAACAATT*TCCGTACAGCATTCCGAAGCTAGAGTTGCTAGACTTGACTGCATTCGTACATC*AATTGTGAGCGGATAACAATT*GTTAGGGAGG*AATTGTGAG*

*CGGATAACAATT*TGGAGTTGAT*AATTGTGAGCGGATAACAATT*GGCTTCAACGT*AATTGTGAGCGGATAACAATT*TCCGTACATC*AATTGTGAGCGGATAACAATT*GTTAGGGAGG*AATTGTGAG*

*CGGATAACAATT*TGGAGTTGAT*AATTGTGAGCGGATAACAATT*GGCTTCAACGT*AATTGTGAGCGGATAACAATT*TCCGTACATC*AATTGTGAGCGGATAACAATT*GTTAGGGAGG*AATTGTGAG*

*CGGATAACAATT*TGGAGTTGAT*AATTGTGAGCGGATAACAATT*GGCTTCAACGT*AATTGTGAGCGGATAACAATT*TCCGTACATC*AATTGTGAGCGGATAACAATT*GTTAGGGAGG*AATTGTGAG*

*CGGATAACAATT*TGGAGTTGAT*AATTGTGAGCGGATAACAATT*GGCTTCAACGT*AATTGTGAGCGGATAACAATT*TCCGTACATC*AATTGTGAGCGGATAACAATT*GTTAGGGAGG*AATTGTGAG*

*CGGATAACAATT*TGGAGTTGAT*AATTGTGAGCGGATAACAATT*GGCTTCAACGT*AATTGTGAGCGGATAACAATT*GTTAGGGAGG*AATTGTGAG*

*CGGATAACAATT*TGGAGTTGAT*AATTGTGAGCGGATAACAATT*GGCTTCAACGT*AATTGTGAGCGGATAACAATT*TCCGTACGAATGGAACTTATGGTACCCAGCTTTTGTTCCCTTTAGTGAGG

GTTAATTGCGCGCTTGGCGTAA**TCATGGTCATAGCTGTTTCCTGTGTG**

Reverse primer

Figure S2

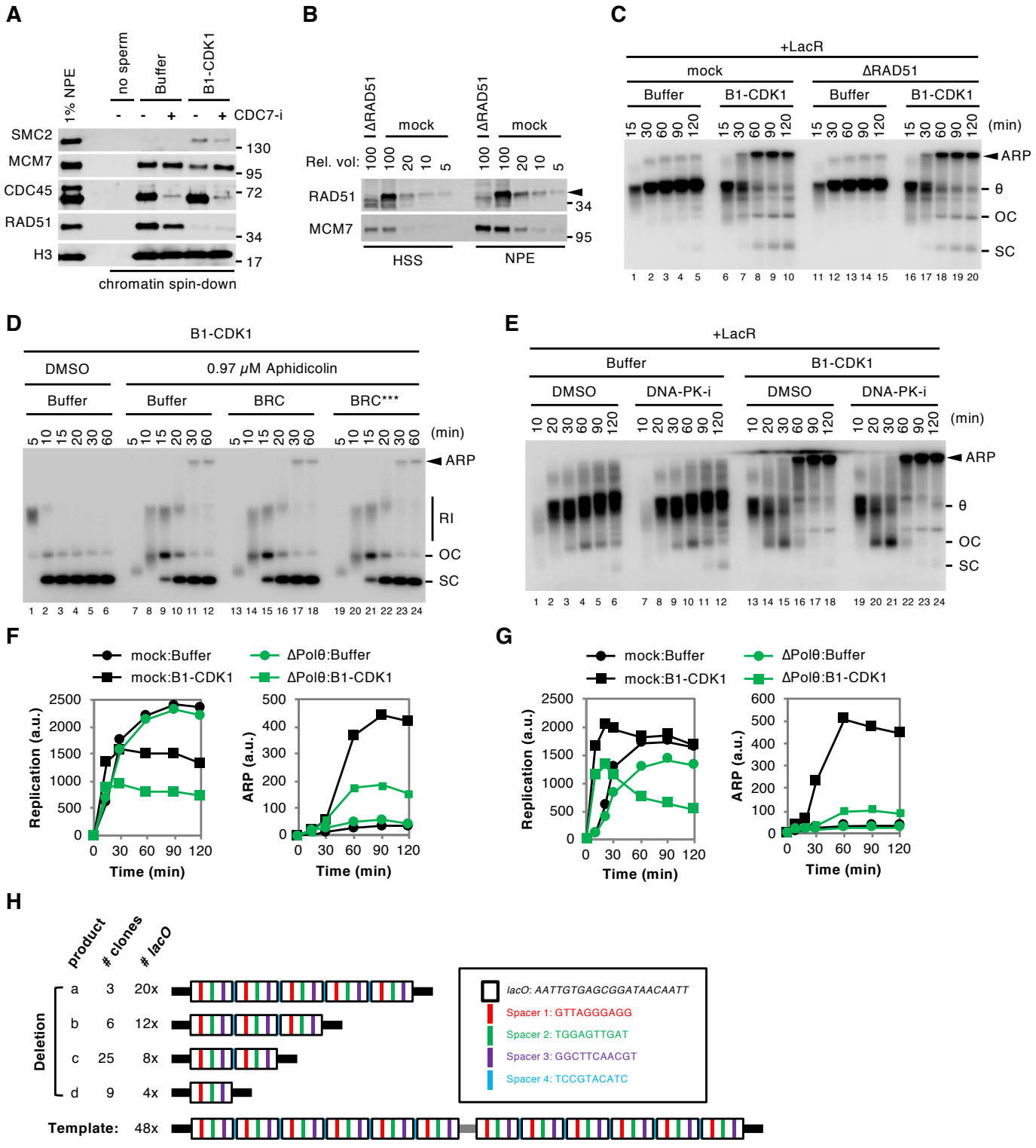
A
1% NPE
no sperm
Buffer
B1-CDK1
- - + - + CDC7-i
SMC2
MCM7
CDC45
RAD51
H3
130
95
72
34
17
chromatin spin-down
B
ΔRAD51
mock
ΔRAD51
mock
Rel. vol: 100 100 20 10 5 100 100 20 10 5
RAD51
MCM7
34
95
HSS
NPE
C
+LacR
mock
ΔRAD51
Buffer
B1-CDK1
Buffer
B1-CDK1
15 30 60 90 120 15 30 60 90 120 15 30 60 90 120 15 30 60 90 120
(min)
ARP
θ
OC
SC
1 2 3 4 5 6 7 8 9 10 11 12 13 14 15 16 17 18 19 20
D
B1-CDK1
DMSO
0.97 μM Aphidicolin
Buffer
Buffer
BRC
BRC***
5 10 15 20 30 60 5 10 15 20 30 60 5 10 15 20 30 60 5 10 15 20 30 60
(min)
ARP
RI
OC
SC
1 2 3 4 5 6 7 8 9 10 11 12 13 14 15 16 17 18 19 20 21 22 23 24
E
+LacR
Buffer
B1-CDK1
DMSO
DNA-PK-i
DMSO
DNA-PK-i
10 20 30 60 90 120 10 20 30 60 90 120 10 20 30 60 90 120 10 20 30 60 90 120
(min)
ARP
θ
OC
SC
1 2 3 4 5 6 7 8 9 10 11 12 13 14 15 16 17 18 19 20 21 22 23 24
F
mock:Buffer
mock:B1-CDK1
ΔPolθ:Buffer
ΔPolθ:B1-CDK1
Replication (a.u.)
0 500 1000 1500 2000 2500
Time (min)
0 30 60 90 120
ARP (a.u.)
0 100 200 300 400 500
Time (min)
0 30 60 90 120
G
mock:Buffer
mock:B1-CDK1
ΔPolθ:Buffer
ΔPolθ:B1-CDK1
Replication (a.u.)
0 500 1000 1500 2000 2500
Time (min)
0 30 60 90 120
ARP (a.u.)
0 100 200 300 400 500 600
Time (min)
0 30 60 90 120
H
product
clones
lacO
Deletion
a 3 20x
b 6 12x
c 25 8x
d 9 4x
Template: 48x
lacO: AATTGTGAGCGGATAACAATT
Spacer 1: GTTAGGGAGG
Spacer 2: TGGAGTTGAT
Spacer 3: GGCTTCAACGT
Spacer 4: TCCGTACATC

Figure S3

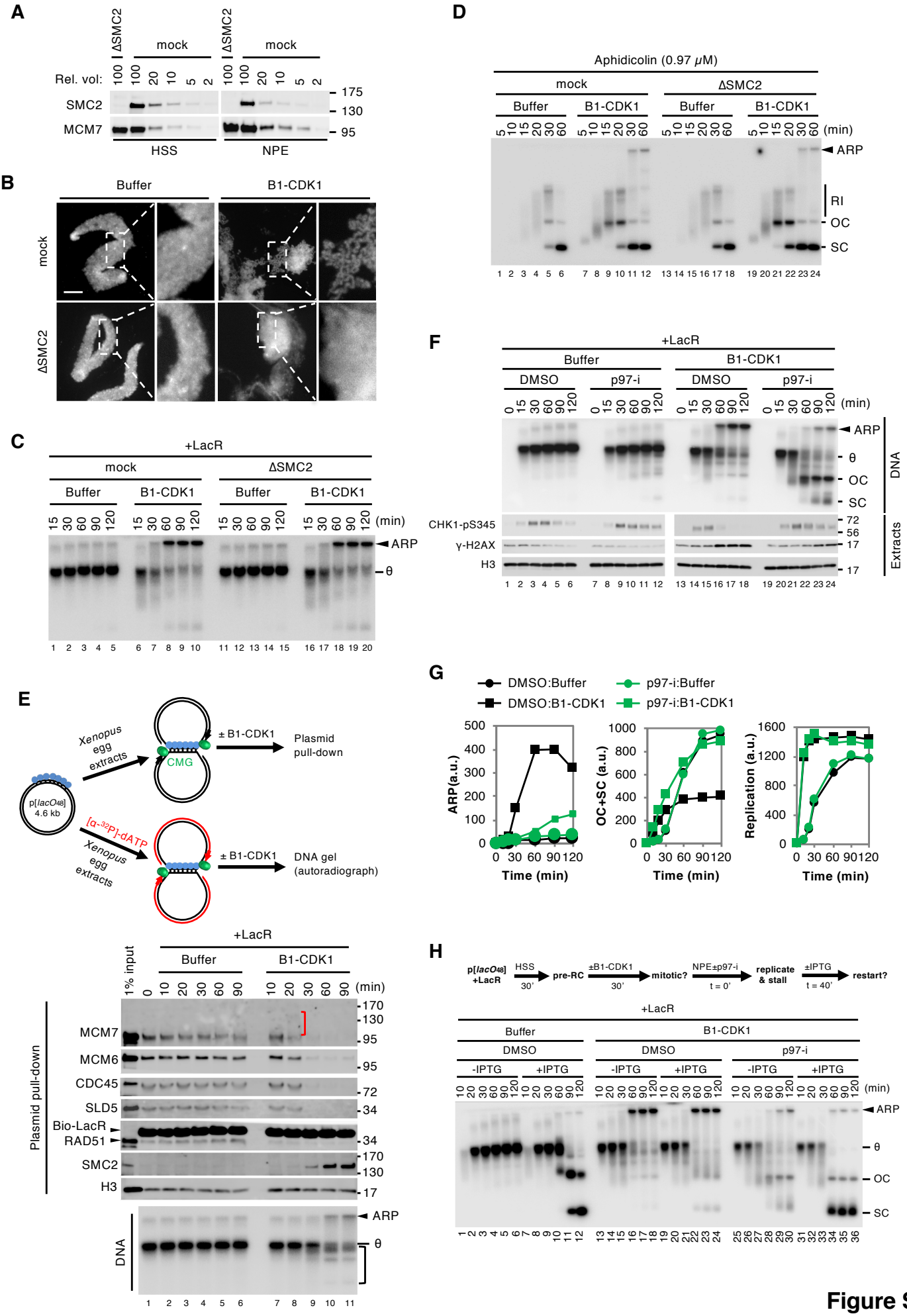
A
ΔSMC2
mock
ΔSMC2
mock
Rel. vol:
100 100 20 10 5 2 100 100 20 10 5 2
SMC2
MCM7
175
130
95
HSS
NPE
B
Buffer
B1-CDK1
mock
ΔSMC2
C
+LacR
mock
ΔSMC2
Buffer
B1-CDK1
Buffer
B1-CDK1
15 30 60 90 120 15 30 60 90 120 15 30 60 90 120 15 30 60 90 120 (min)
ARP
θ
1 2 3 4 5 6 7 8 9 10 11 12 13 14 15 16 17 18 19 20
D
Aphidicolin (0.97 μM)
mock
ΔSMC2
Buffer
B1-CDK1
Buffer
B1-CDK1
5 10 15 20 30 60 5 10 15 20 30 60 5 10 15 20 30 60 5 10 15 20 30 60 (min)
ARP
RI
OC
SC
1 2 3 4 5 6 7 8 9 10 11 12 13 14 15 16 17 18 19 20 21 22 23 24
E
Xenopus egg extracts
p[lacO48] 4.6 kb
CMG
± B1-CDK1
Plasmid pull-down
[α-32P]-dATP
Xenopus egg extracts
± B1-CDK1
DNA gel (autoradiograph)
+LacR
Buffer
B1-CDK1
1% input
0 10 20 30 60 90 10 20 30 60 90 (min)
Plasmid pull-down
MCM7
MCM6
CDC45
SLD5
Bio-LacR
RAD51
SMC2
H3
170
130
95
95
72
34
34
170
130
17
DNA
ARP
θ
1 2 3 4 5 6 7 8 9 10 11
F
+LacR
Buffer
B1-CDK1
DMSO
p97-i
DMSO
p97-i
0 15 30 60 90 120 0 15 30 60 90 120 0 15 30 60 90 120 0 15 30 60 90 120 (min)
ARP
θ
OC
SC
DNA
CHK1-pS345
γ-H2AX
H3
72
56
17
17
Extracts
1 2 3 4 5 6 7 8 9 10 11 12 13 14 15 16 17 18 19 20 21 22 23 24
G
DMSO:Buffer
DMSO:B1-CDK1
p97-i:Buffer
p97-i:B1-CDK1
ARP (a.u.)
OC+SC (a.u.)
Replication (a.u.)
Time (min)
Time (min)
Time (min)
H
p[lacO48] +LacR
HSS
30'
pre-RC
±B1-CDK1
30'
mitotic?
NPE±p97-i
t = 0'
replicate & stall
±IPTG
t = 40'
restart?
+LacR
Buffer
B1-CDK1
DMSO
DMSO
p97-i
-IPTG
+IPTG
-IPTG
+IPTG
-IPTG
+IPTG
10 20 30 60 90 120 10 20 30 60 90 120 10 20 30 60 90 120 10 20 30 60 90 120 10 20 30 60 90 120 10 20 30 60 90 120 (min)
ARP
θ
OC
SC
1 2 3 4 5 6 7 8 9 10 11 12 13 14 15 16 17 18 19 20 21 22 23 24 25 26 27 28 29 30 31 32 33 34 35 36

Figure S4

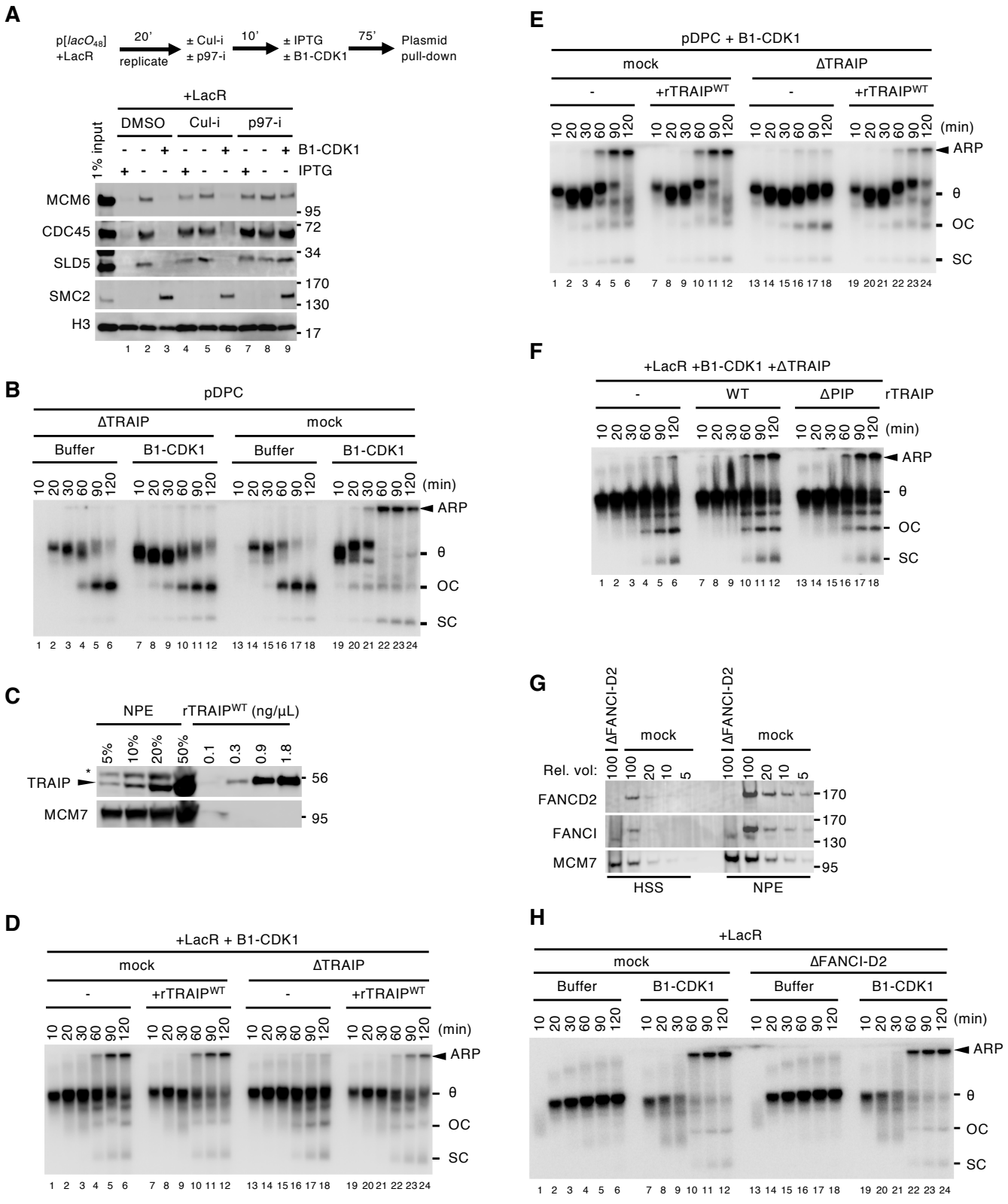
A
p[lacO48] +LacR
20'
replicate
± Cul-i ± p97-i
10'
± IPTG ± B1-CDK1
75'
Plasmid pull-down
+LacR
DMSO
Cul-i
p97-i
1% input
B1-CDK1
IPTG
MCM6
CDC45
SLD5
SMC2
H3
95
72
34
170
130
17
1 2 3 4 5 6 7 8 9
B
pDPC
ΔTRAIP
mock
Buffer
B1-CDK1
(min)
ARP
θ
OC
SC
1 2 3 4 5 6 7 8 9 10 11 12 13 14 15 16 17 18 19 20 21 22 23 24
C
NPE
rTRAIP^WT (ng/μL)
5%
10%
20%
50%
0.1
0.3
0.9
1.8
TRAIP
MCM7
56
95
D
+LacR + B1-CDK1
mock
ΔTRAIP
-
+rTRAIP^WT
(min)
ARP
θ
OC
SC
1 2 3 4 5 6 7 8 9 10 11 12 13 14 15 16 17 18 19 20 21 22 23 24
E
pDPC + B1-CDK1
mock
ΔTRAIP
-
+rTRAIP^WT
(min)
ARP
θ
OC
SC
1 2 3 4 5 6 7 8 9 10 11 12 13 14 15 16 17 18 19 20 21 22 23 24
F
+LacR +B1-CDK1 +ΔTRAIP
-
WT
ΔPIP
rTRAIP
(min)
ARP
θ
OC
SC
1 2 3 4 5 6 7 8 9 10 11 12 13 14 15 16 17 18
G
ΔFANCI-D2
mock
Rel. vol:
100
20
10
5
FANCD2
FANCI
MCM7
170
170
130
95
HSS
NPE
H
+LacR
mock
ΔFANCI-D2
Buffer
B1-CDK1
(min)
ARP
θ
OC
SC
1 2 3 4 5 6 7 8 9 10 11 12 13 14 15 16 17 18 19 20 21 22 23 24

Figure S5

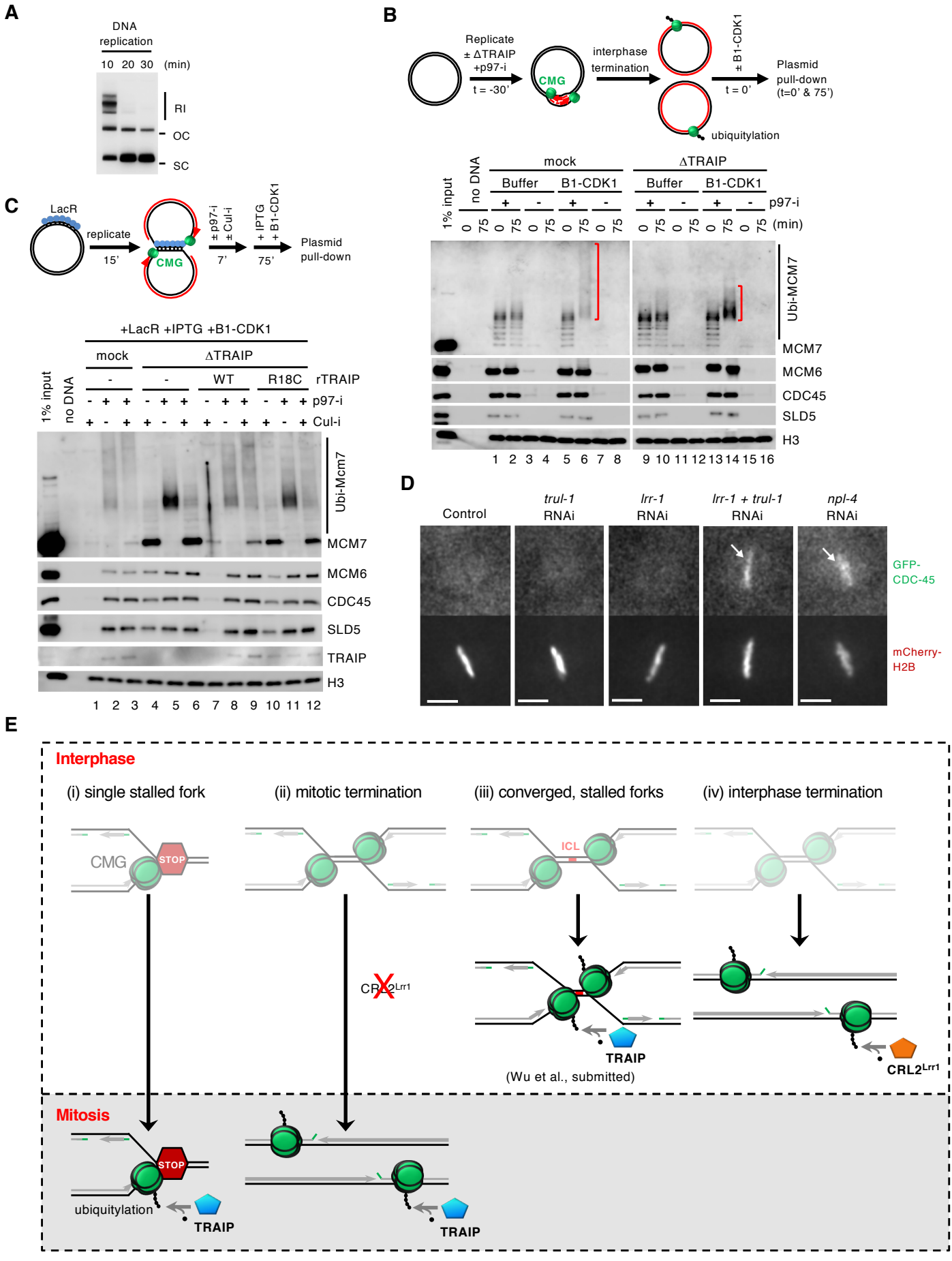
A
DNA replication
10 20 30 (min)
RI
OC
SC
B
Replicate
± ΔTRAIP
+p97-i
t = -30'
CMG
interphase termination
± B1-CDK1
t = 0'
Plasmid pull-down (t=0' & 75')
ubiquitylation
mock
ΔTRAIP
Buffer
B1-CDK1
1% input
no DNA
p97-i
(min)
Ubi-MCM7
MCM7
MCM6
CDC45
SLD5
H3
1 2 3 4 5 6 7 8 9 10 11 12 13 14 15 16
C
LacR
replicate
15'
CMG
± p97-i
± Cul-i
7'
+ IPTG
+ B1-CDK1
75'
Plasmid pull-down
+LacR +IPTG +B1-CDK1
mock
ΔTRAIP
WT
R18C
rTRAIP
p97-i
Cul-i
1% input
no DNA
Ubi-Mcm7
MCM7
MCM6
CDC45
SLD5
TRAIP
H3
1 2 3 4 5 6 7 8 9 10 11 12
D
Control
trul-1 RNAi
lrr-1 RNAi
lrr-1 + trul-1 RNAi
npl-4 RNAi
GFP-CDC-45
mCherry-H2B
E
Interphase
(i) single stalled fork
(ii) mitotic termination
(iii) converged, stalled forks
(iv) interphase termination
CMG
STOP
ICL
CRL2Lrr1
TRAIP
(Wu et al., submitted)
Mitosis
STOP
ubiquitylation
TRAIP
TRAIP
CRL2Lrr1

Figure S6

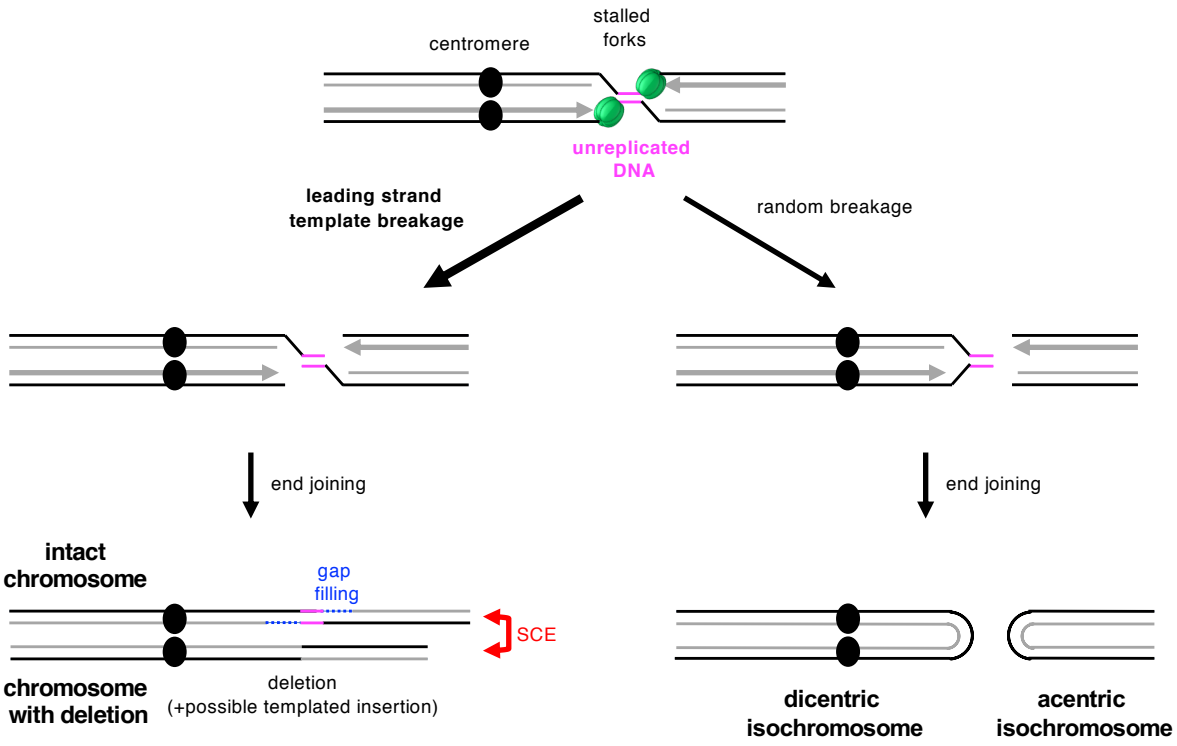
centromere
stalled forks
unreplicated DNA
leading strand template breakage
random breakage
end joining
end joining
intact chromosome
gap filling
SCE
chromosome with deletion
deletion
(+possible templated insertion)
dicentric isochromosome
acentric isochromosome

Figure S7

Ubiquitylation of the CMG helicase regulates vertebrate DNA repair

R. Alex Wu[1*], Daniel R. Semlow[1*], Ashley N. Kamimae-Lanning[2], Olga V. Kochenova[1], Michael R. Hodskinson[2], Ravindra Amunugama[1], Lin Deng[1,3,4], Claudia A. Mimoso[1], Ketan J. Patel[2,5] & Johannes C. Walter[1,6†]

[1] Department of Biological Chemistry and Molecular Pharmacology, Harvard Medical School, Boston, MA 02115, USA.
[2] MRC Laboratory of Molecular Biology, Cambridge Biomedical Campus, Cambridge CB2 0QH, UK.
[3] Department of Pediatric Oncology, Dana-Farber Cancer Institute, Boston, MA 02215, USA.
[4] Department of Cell Biology, Harvard Medical School, Boston, MA 02115, USA.
[5] Department of Medicine, University of Cambridge, Addenbrooke's Hospital, Cambridge CB2 0QQ, UK.
[6] Howard Hughes Medical Institute, Boston, MA 02115, USA.

[†] e-mail: Johannes_Walter@hms.harvard.edu
[*] These authors contributed equally to this work

Summary: Cells often use multiple pathways to repair the same DNA lesion, and elucidating how one pathway is prioritized over another is crucial to understand how cells maintain genome stability. DNA interstrand cross-links (ICLs) block DNA replication and transcription by covalently linking the Watson and Crick strands of DNA, and the cytotoxicity of ICLs underlies numerous chemotherapeutics. Replication fork collision with ICLs initiates two distinct repair pathways. The NEIL3 glycosylase can cleave the cross-link[1], but if this fails, the Fanconi anemia (FA) proteins incise the phosphodiester backbone surrounding the ICL, generating a DSB intermediate that is repaired by homologous recombination[2]. How cells prioritize the simple NEIL3 pathway over the FA pathway, which can cause genomic rearrangements, is unknown. Here we show that the E3 ubiquitin ligase TRAIP is a master regulator of both ICL repair pathways. Fork convergence at ICLs triggers TRAIP-dependent formation of ubiquitin chains on the replicative DNA helicase CMG (CDC45-MCM2-7-GINS). Short chains can recruit NEIL3 through direct ubiquitin binding, whereas longer chains are required for CMG unloading by the p97 ATPase, enabling the FA pathway. Our results identify replicative helicase ubiquitylation as a new signal that dictates DNA repair pathway choice and implicate TRAIP as an attractive target of cancer chemotherapy.

ICLs are formed by chemotherapeutics and endogenous reactive aldehydes[3,4]. The classic ICL repair pathway involves twenty-two "FANC" proteins, defects in which cause the human bone marrow failure and cancer predisposition syndrome, FA[5]. Using *Xenopus* egg extracts, we previously showed that the FA pathway is initiated by the convergence of two replication forks on an ICL, which triggers CMG helicase unloading by the p97 ATPase[1,2,6,7]. CMG unloading involves polyubiquitylation of CMG's MCM7 subunit[7], allowing fork reversal and ICL unhooking via

nucleolytic incisions that convert the ICL to a DNA double stranded break[2,8,9] (Fig. 1a, left branch). A second unhooking mechanism acts on a subset of ICLs[1] (Fig. 1a, right branch). In this pathway, the NEIL3 DNA glycosylase cleaves one of the two *N*-glycosyl bonds comprising the ICL, which avoids DSB formation. While both pathways are triggered by fork convergence, only the FA pathway requires CMG unloading[1]. In mammals, FANC gene mutations cause stronger phenotypes than mutations in NEIL3[10-13]. Therefore, while cells may first attempt the simpler NEIL3 pathway, they appear to rely more heavily on the versatile FA pathway for survival. Given the different mutagenic potentials of the FA and NEIL3 pathways, it is crucial to understand how cells govern the choice between these two mechanisms.

Another critical gap in our knowledge is the identity of the E3 ubiquitin ligase that ubiquitylates CMG at ICLs to activate CMG unloading and entry into the FA pathway. The RING E3 ligase TRAIP (TRAF-interacting protein) is essential for cell proliferation[14], and hypomorphic TRAIP mutations cause microcephalic primordial dwarfism[15]. Because TRAIP knock-down sensitizes cells to mitomycin C (MMC)[16] and TRAIP associates with ICL-containing chromatin[17], we asked whether TRAIP promotes CMG unloading at ICLs. To this end, *Xenopus* egg extracts (Extended Data Fig. 1a) were used to replicate a plasmid containing a site-specific cisplatin-ICL. In mock-depleted extract, forks converged on the ICL and stalled, generating a discrete "slow Figure 8" intermediate that was converted to a "fast Figure 8" species due to CMG unloading[8] (Fig. 1b, lanes 1-3, Extended Data Fig. 1b). Strikingly, depletion of TRAIP (Extended Data Fig. 2a) caused an accumulation of the slow Figure 8 intermediate (Fig. 1b, lanes 11-15), the same defect observed when CMG unloading was blocked with a p97 inhibitor[1] (p97i; Fig. 1b, lanes 6-10). Wild-type recombinant *Xenopus* TRAIP (rTRAIP^{WT}) (Extended Data Fig. 2b) restored fast Figure 8 formation (Fig. 1b, Extended Data Fig. 2c). In contrast, rTRAIP^{R18C} (Extended Data Fig. 2b),

which harbors a primordial dwarfism-associated RING-domain mutation[15] that compromises E3 ubiquitin ligase activity (Extended Data Fig. 2d), did not (Fig. 1b). Consistent with TRAIP-dependent CMG unloading, efficient loss of the CMG footprint at ICLs required the E3 ligase activity of TRAIP (Extended Data Fig. 2e, f). As shown in Fig. 1c, active TRAIP was required for dissociation of CDC45 and MCM7, two CMG subunits, from pICL^{Pt}. In addition, formation of ubiquitylated MCM7 was dependent on TRAIP (Fig. 1c). This effect was even more evident when CMG unloading was blocked with p97i (Fig. 1d). rTRAIP^{R18C} partially rescued MCM7 ubiquitylation (Fig. 1d, compare lanes 13-14 with 7-8), consistent with residual E3 ligase activity in this mutant (Extended Data Fig. 2d). Our previous conclusion that BRCA1 is required for CMG unloading[18] was due to inadvertent depletion of TRAIP with BRCA1 antiserum (Extended Data Fig. 3). Importantly, active TRAIP is required for replication fork reversal at an ICL (Fig. 1e), a likely prerequisite for incisions[8] (Fig. 1a), and for error-free repair of the lesion (Fig. 1f). Collectively, these results demonstrate that TRAIP is required for MCM7 ubiquitylation and CMG unloading in the FA ICL repair pathway.

Consistent with CMG unloading at ICLs requiring fork convergence[6], MCM7 ubiquitylation also depended on replication fork convergence (Fig. 2a). Thus, either TRAIP is recruited *de novo* when CMGs converge on an ICL, or it travels with the replisome but only ubiquitylates CMG upon fork convergence. In agreement with the latter scenario, TRAIP associated with undamaged pCTRL at levels similar to those seen on pICL (Fig. 2b, compare lanes 2 and 5), and in mammalian cells, TRAIP localizes to DNA replication forks in the absence of exogenous insults[15,16]. TRAIP lacking its conserved, C-terminal PIP box (TRAIP$^{\Delta PIP}$) still suppresses MMC hypersensitivity[16]. Similarly, recombinant *Xenopus* TRAIP$^{\Delta PIP}$ suppressed the accumulation of slow Figure 8 structures (Fig. 2c, Extended Data Fig. 3g). TRAIP therefore travels

with the replisome but ubiquitylates CMG only after fork convergence at an ICL, independently of its PIP box.

TRAIP does not participate in CMG unloading during replication termination (Extended Data Fig. 4a, b), which depends on formation of K48-linked ubiquitin chains by $CRL2^{LRR1}$ (Fig. 2d)[19,20]. Conversely, MCM7 ubiquitylation and CMG unloading at ICLs does not require $CRL2^{LRR1}$ (Extended Data Fig. 4a, c-e), and the chains formed by TRAIP in this context involve primarily K63-linkages, as determined by digestion with chain-specific deubiquitylating enzymes[21] (Fig. 2d). Thus, CMG unloading during ICL repair is mechanistically distinct from CMG unloading during replication termination and likely involves formation of K63-linked ubiquitin chains on CMG.

Unlike cisplatin-ICLs, psoralen-ICLs and AP-ICLs (formed between an abasic site in one strand and an adenosine in the other strand) are unhooked by NEIL3 independently of CMG unloading[1]. However, as shown in Extended Data Fig. 5a, MCM7 was ubiquitylated with similar kinetics when forks converged on an AP-ICL versus a cisplatin-ICL. We therefore asked whether AP-ICL repair requires TRAIP. In mock-depleted extract, Figure 8 intermediates generated when forks converge on an AP-ICL were converted directly into open circular and supercoiled products, reflecting NEIL3-dependent unhooking[1] (Fig. 3a; see Extended Data Fig. 5b for a schematic of $pICL^{AP}$ repair intermediates). Strikingly, unlike p97 inhibition (Extended Data Fig. 5c, lanes 27-30), immunodepletion of TRAIP caused a marked accumulation of slow Figure 8s and a strong reduction in open circular and supercoiled plasmids (Fig. 3a). Furthermore, TRAIP depletion greatly reduced AP-ICL repair (Fig. 3b). Addition of $rTRAIP^{WT}$ fully reversed these defects (Fig. 3a, b, Extended Data Fig. 5d). Surprisingly, $rTRAIP^{R18C}$ also mostly reversed these defects, suggesting that low levels of ubiquitylation support AP-ICL repair (Fig. 3a, b, Extended Data Fig.

5d). Thus, TRAIP performs a critical function during AP-ICL repair that is independent of CMG unloading.

We postulated that TRAIP-dependent MCM7 ubiquitylation recruits NEIL3 to converged forks. Because endogenous NEIL3 on chromatin was undetectable by immunoblotting, we supplemented extract with FLAG epitope-tagged recombinant NEIL3 (rNEIL3) and examined its chromatin binding using FLAG antibody. rNEIL3 recovery was abolished by geminin, demonstrating its binding was replication-dependent (Extended Data Fig. 5a). Interestingly, we detected more rNEIL3 on $pICL^{Pt}$ than on $pICL^{AP}$ (Extended Data Fig. 5a), likely because NEIL3 becomes trapped on chromatin when it cannot unhook the ICL (Extended Data Fig. 5e, f). Given this increased association of rNEIL3 with $pICL^{Pt}$, this plasmid was used for subsequent NEIL3 recruitment assays. Importantly, depletion of TRAIP strongly reduced the association of rNEIL3 with $pICL^{Pt}$ (Fig. 3c, lanes 1-8). Recombinant $TRAIP^{WT}$ fully rescued and $rTRAIP^{R18C}$ partially rescued this defect (Fig. 3c, Extended Data Fig. 5g). Our data indicate that TRAIP-dependent CMG ubiquitylation is required to recruit NEIL3 for ICL unhooking. Consistent with this model, delaying CMG unloading extends the window of time during which NEIL3 can unhook an AP-ICL (Extended Data Fig. 6).

NEIL3 contains an N-terminal glycosylase domain and three C-terminal zinc finger motifs[22] (Fig. 3d). NEIL3 lacking the entire C-terminal region ($rNEIL3^{\Delta 291}$) was active as a glycosylase (Extended Data Fig. 7a) but failed to unhook $pICL^{AP}$ (Fig. 3e) or bind pICL in extract (Fig. 3f), suggesting that one or more of the zinc fingers helps recruit NEIL3 to stalled forks. Using biolayer interferometry, we found that the NPL4-type zinc finger (NZF) of NEIL3 binds monoubiquitin dependent on a conserved TL motif (Extended Data Fig. 7b), as seen for other NZFs[23]. Importantly, $pICL^{AP}$ unhooking was reduced more than two-fold by a TL motif

substitution (rNEIL3$^{TL310-311LV}$) and four-fold by substitutions of zinc-coordinating cysteines in the NZF (rNEIL3$^{NZF\text{-}C\ to\ A}$; Fig. 3e, Extended Data Fig. 7c). Consistent with this observation, rNEIL3$^{NZF\text{-}C\ to\ A}$ and rNEIL3$^{TL310-311LV}$ bound poorly to pICL (Fig. 3f). The other two NEIL3 zinc fingers resemble the "GRF" zinc finger of the AP endonuclease APE2, which binds single-stranded (ss)DNA[24]. We found that GRF1 and GRF2 each bound specifically to ssDNA (Extended Data Fig. 8a, b), and point mutations that disrupt this binding compromised the association of NEIL3 with chromatin and its ability to support AP-ICL unhooking (Extended Data Fig. 8c-e). Our data suggest that NEIL3 is targeted to converged CMGs through cooperation of its NZF, which recognizes ubiquitylated MCM7, and its GRFs, which recognize ssDNA, possibly on the lagging strand template (Extended Data Fig. 8f).

In egg extracts, AP-ICLs and psoralen ICLs are processed almost exclusively by NEIL3, but in its absence, these lesions are unhooked by the FA pathway[1]. The question arises how the NEIL3 pathway is prioritized over the FA pathway. Interestingly, rTRAIP^{R18C}, which only forms short ubiquitin chains on MCM7 (Figs. 1c, 3c), had no detectable activity in cisplatin-ICL repair (Fig. 1b, e) while promoting robust AP-ICL repair (Fig. 3a, b). These results suggest that short ubiquitin chains might be sufficient to support the NEIL3 but not the FA pathway. Consistent with this idea, ubiquitin that lacks lysines and therefore cannot undergo polyubiquitylation (Ub^{NoK}) greatly stabilized the pICL^{Pt} slow Figure 8 species (indicative of defective p97-dependent CMG unloading) while having only a modest effect on pICL^{AP} slow Figure 8 disappearance, which reflects NEIL3 unhooking (Fig. 4a; see graphs for quantification). As expected, Ub^{NoK} reduced the length of ubiquitin chains formed on MCM7 (Fig. 4b). Consistent with its modest effect on AP-ICL unhooking, Ub^{NoK} did not affect recruitment of NEIL3 to chromatin (Fig. 4b). The data suggest that short ubiquitin chains on MCM7 are sufficient to recruit NEIL3. If the ICL cannot be

cleaved by NEIL3, as in the case of cisplatin-ICLs, the chains continue to grow, leading to activation of p97-dependent CMG unloading (Fig. 4c).

Our results establish TRAIP as a master regulator of ICL repair that prioritizes the NEIL3 pathway over the FA pathway. Consistent with redundancy between the FA and NEIL3 pathways in the repair of certain lesions, both must be eliminated in mammalian cells to observe hypersensitivity to psoralen-ICLs while removal of the FA pathway suffices to sensitize cells to cisplatin (Fig. 4d, Extended Data Fig. 9). In interphase, TRAIP ubiquitylates CMG only upon fork convergence, which avoids inadvertent CMG unloading from forks that have not completed synthesis. Given the extreme ICL sensitivity of cells lacking TRAIP[16], our data strongly imply that a significant number of ICL repair events in cells require CMG convergence, even though a single fork may be able to trigger repair[25]. The regulation of TRAIP is different in mitosis, where Cdk1-Cyclin B promotes TRAIP activity in the absence of fork convergence (Deng et al., submitted, Extended Data Fig. 10).

Patients expressing $TRAIP^{R18C}$ present with primordial dwarfism, which is caused by reduced cell proliferation[15]. We show that $TRAIP^{R18C}$ promotes residual ubiquitylation and robust unhooking by NEIL3. We propose that in vivo, $TRAIP^{R18C}$ suppresses the symptoms of Fanconi anemia by supporting the FA pathway, albeit with slower kinetics. Thus, endogenous ICLs may lead to a temporary G2 arrest, leading to reduced cell proliferation and dwarfism. Consistent with this model, cells from both FA and TRAIP patients exhibit slow progression through G2 in the absence of exogenous crosslinking agents[15,26], and FA patients often exhibit short stature[5].

References:

1 Semlow, D. R., Zhang, J., Budzowska, M., Drohat, A. C. & Walter, J. C. Replication-Dependent Unhooking of DNA Interstrand Cross-Links by the NEIL3 Glycosylase. *Cell* **167**, 498-511, doi:10.1016/j.cell.2016.09.008 (2016).

2 Raschle, M. *et al.* Mechanism of replication-coupled DNA interstrand crosslink repair. *Cell* **134**, 969-980 (2008).

3 Deans, A. J. & West, S. C. DNA interstrand crosslink repair and cancer. *Nat Rev Cancer* **11**, 467-480, doi:10.1038/nrc3088 (2011).

4 Price, N. E., Catalano, M. J., Liu, S., Wang, Y. & Gates, K. S. Chemical and structural characterization of interstrand cross-links formed between abasic sites and adenine residues in duplex DNA. *Nucleic Acids Res* **43**, 3434-3441, doi:10.1093/nar/gkv174 (2015).

5 Kottemann, M. C. & Smogorzewska, A. Fanconi anaemia and the repair of Watson and Crick DNA crosslinks. *Nature* **493**, 356-363, doi:10.1038/nature11863 (2013).

6 Zhang, J. *et al.* DNA interstrand cross-link repair requires replication-fork convergence. *Nat Struct Mol Biol* **22**, 242-247, doi:10.1038/nsmb.2956 (2015).

7 Fullbright, G., Rycenga, H. B., Gruber, J. D. & Long, D. T. p97 Promotes a Conserved Mechanism of Helicase Unloading during DNA Cross-Link Repair. *Mol Cell Biol* **36**, 2983-2994, doi:10.1128/MCB.00434-16 (2016).

8 Amunugama, R. *et al.* Replication Fork Reversal During DNA Interstrand Crosslink Repair Requires CMG Unloading. *Cell Rep* **23**, 3419-3428 (2018).

9 Knipscheer, P. *et al.* The Fanconi anemia pathway promotes replication-dependent DNA interstrand cross-link repair. *Science* **326**, 1698-1701 (2009).

10 Massaad, M. J. *et al.* Deficiency of base excision repair enzyme NEIL3 drives increased predisposition to autoimmunity. *J Clin Invest* **126**, 4219-4236, doi:10.1172/JCI85647 (2016).

11 Parmar, K., D'Andrea, A. & Niedernhofer, L. J. Mouse models of Fanconi anemia. *Mutat Res* **668**, 133-140, doi:10.1016/j.mrfmmm.2009.03.015 (2009).

12 Sejersted, Y. *et al.* Endonuclease VIII-like 3 (Neil3) DNA glycosylase promotes neurogenesis induced by hypoxia-ischemia. *Proc Natl Acad Sci U S A* **108**, 18802-18807, doi:10.1073/pnas.1106880108 (2011).

13 Torisu, K., Tsuchimoto, D., Ohnishi, Y. & Nakabeppu, Y. Hematopoietic tissue-specific expression of mouse Neil3 for endonuclease VIII-like protein. *J Biochem* **138**, 763-772, doi:10.1093/jb/mvi168 (2005).

14 Chapard, C., Hohl, D. & Huber, M. The role of the TRAF-interacting protein in proliferation and differentiation. *Exp Dermatol* **21**, 321-326, doi:10.1111/j.1600-0625.2012.01477.x (2012).

15 Harley, M. E. *et al.* TRAIP promotes DNA damage response during genome replication and is mutated in primordial dwarfism. *Nat Genet* **48**, 36-43, doi:10.1038/ng.3451 (2016).

16 Hoffmann, S. *et al.* TRAIP is a PCNA-binding ubiquitin ligase that protects genome stability after replication stress. *J Cell Biol* **212**, 63-75, doi:10.1083/jcb.201506071 (2016).

17 Raschle, M. *et al.* DNA repair. Proteomics reveals dynamic assembly of repair complexes during bypass of DNA cross-links. *Science* **348**, 1253671, doi:10.1126/science.1253671 (2015).

18 Long, D. T., Joukov, V., Budzowska, M. & Walter, J. C. BRCA1 promotes unloading of the CMG helicase from a stalled DNA replication fork. *Mol Cell* **56**, 174-185, doi:10.1016/j.molcel.2014.08.012 (2014).
19 Moreno, S. P., Bailey, R., Campion, N., Herron, S. & Gambus, A. Polyubiquitylation drives replisome disassembly at the termination of DNA replication. *Science* **346**, 477-481, doi:10.1126/science.1253585 (2014).
20 Dewar, J. M., Low, E., Mann, M., Raschle, M. & Walter, J. C. CRL2(Lrr1) promotes unloading of the vertebrate replisome from chromatin during replication termination. *Genes Dev* **31**, 275-290, doi:10.1101/gad.291799.116 (2017).
21 Mevissen, T. E. *et al.* OTU deubiquitinases reveal mechanisms of linkage specificity and enable ubiquitin chain restriction analysis. *Cell* **154**, 169-184 (2013).
22 Liu, M. *et al.* Expression and purification of active mouse and human NEIL3 proteins. *Protein Expr Purif* **84**, 130-139, doi:10.1016/j.pep.2012.04.022 (2012).
23 Wang, B. *et al.* Structure and ubiquitin interactions of the conserved zinc finger domain of Npl4. *J Biol Chem* **278**, 20225-20234, doi:10.1074/jbc.M300459200 (2003).
24 Wallace, B. D. *et al.* APE2 Zf-GRF facilitates 3'-5' resection of DNA damage following oxidative stress. *Proc Natl Acad Sci U S A* **114**, 304-309, doi:10.1073/pnas.1610011114 (2017).
25 Huang, J. *et al.* The DNA Translocase FANCM/MHF Promotes Replication Traverse of DNA Interstrand Crosslinks. *Mol Cell* **52**, 434-446, doi:10.1016/j.molcel.2013.09.021 (2013).
26 Dutrillaux, B., Aurias, A., Dutrillaux, A. M., Buriot, D. & Prieur, M. The cell cycle of lymphocytes in Fanconi anemia. *Hum Genet* **62**, 327-332 (1982).

Acknowledgements:

We thank David Pellman and members of the Walter lab for comments on the manuscript. We thank Kelly Arnett of the Center for Macromolecular Interactions for help with BLI experiments. Work on ICL repair in the Walter laboratory is supported by NIH grant HL098316 and a gift from the Wiseman family. R.A.W. is supported by postdoctoral fellowship 131415-PF-17-168-01-DMC from the American Cancer Society. D.R.S. is supported by a Jane Coffin Childs postdoctoral fellowship. J.C.W is a Howard Hughes Medical Institute Investigator and an American Cancer Society Research Professor.

Author contributions:

R.A.W. identified TRAIP as the E3 ligase that ubiquitylates CMG and characterized the role of TRAIP in cisplatin-ICL repair. D.R.S. characterized the role of CMG ubiquitylation in AP-ICL repair and performed NEIL3 structure-function analysis. A.N.K.-L. and M.R.H. performed the experiments in Fig. 4d and Extended Data Fig. 9 under the supervision of K.J.P. O.V.K. performed the experiments in Fig. 1c, d and Extended Data Fig. 5a and c. R.A. performed EM analysis in Extended Data Fig. 1e. L.D. performed the experiment in Extended Data Fig. 10. C.A.M. assisted with the experiments in Extended Data Figs. 7b, 8a and b. J.C.W., R.A.W., and D.R.S. designed experiments, analyzed the data, and wrote the paper with input from the other authors.

Author information:

 The authors declare no competing financial interests. Correspondence and requests for materials should be addressed to J.C.W. (Johannes_Walter@hms.harvard.edu).

Fig. 1

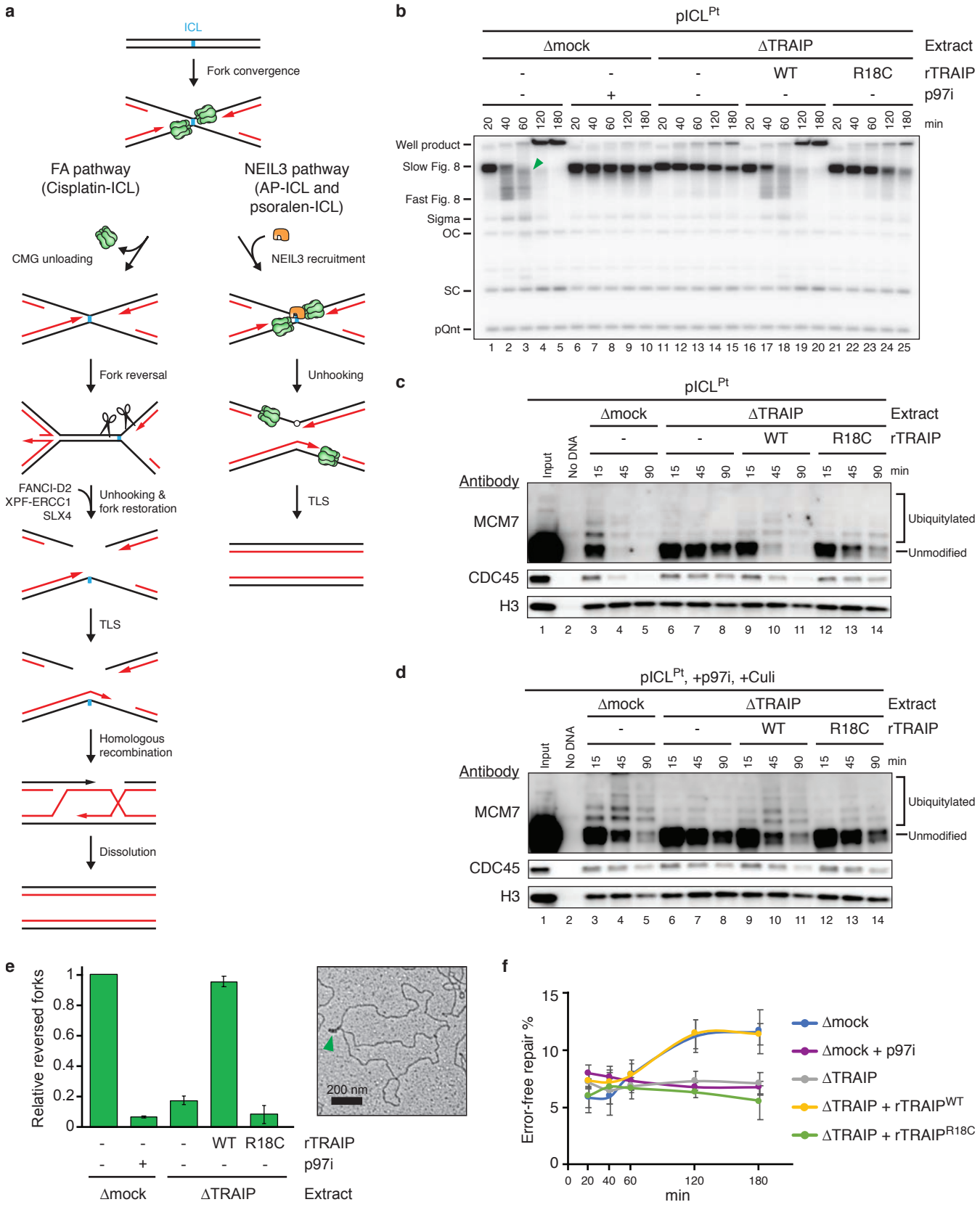
a
ICL
Fork convergence
FA pathway
(Cisplatin-ICL)
NEIL3 pathway
(AP-ICL and
psoralen-ICL)
CMG unloading
NEIL3 recruitment
Fork reversal
Unhooking
FANCI-D2
XPF-ERCC1
SLX4
Unhooking &
fork restoration
TLS
TLS
Homologous
recombination
Dissolution
b
pICL^Pt
Δmock
ΔTRAIP
Extract
rTRAIP
p97i
min
Well product
Slow Fig. 8
Fast Fig. 8
Sigma
OC
SC
pQnt
c
pICL^Pt
Antibody
MCM7
CDC45
H3
Input
No DNA
Ubiquitylated
Unmodified
d
pICL^Pt, +p97i, +Culi
e
Relative reversed forks
200 nm
f
Error-free repair %
Δmock
Δmock + p97i
ΔTRAIP
ΔTRAIP + rTRAIP^WT
ΔTRAIP + rTRAIP^R18C

Fig. 1 | CMG unloading at ICLs requires the E3 ubiquitin ligase TRAIP

a, Models of ICL repair by the FA (left branch) and NEIL3 (right branch) pathways. Black lines, parental DNA strands; Red lines, nascent strands; Cyan, ICL; TLS, translesion DNA synthesis.

b, $pICL^{Pt}$ was replicated in egg extracts containing [α-^{32}P]dATP. Replication intermediates were resolved on a native agarose gel and visualized by autoradiography. Recombinant $TRAIP^{WT}$, $rTRAIP^{R18C}$, and p97i were added as indicated. OC, open circular; SC, supercoiled; pQnt, undamaged control plasmid; Green arrowhead, reversed fork (see Extended Data Fig. 1b for discussion).

c and d, Analysis of proteins associated with $pICL^{Pt}$ during replication in the indicated extracts in the absence (**c**) or presence (**d**) of p97i and cullin ubiquitin ligase inhibitor (Culi), which was added to prevent confounding effects of cullin RING E3 ubiquitin ligases.

e, Left, $pICL^{Pt}$ was replicated for 90 minutes in the indicated extracts, and the relative abundance of reversed forks, as determined by electron microscopy, was quantified and graphed. Values were normalized to the mock-depleted extract. Error bars represent the range from two independent experiments. Right, representative electron micrograph of a reversed fork (green arrowhead) from TRAIP-depleted extract supplemented with $rTRAIP^{WT}$.

f, Error-free repair in the indicated extracts as measured by regeneration of a SapI restriction site. The ~7% basal SapI cutting is due to contaminating undamaged plasmid[9]. Error bars, standard error of the mean from three independent experiments.

Fig. 2

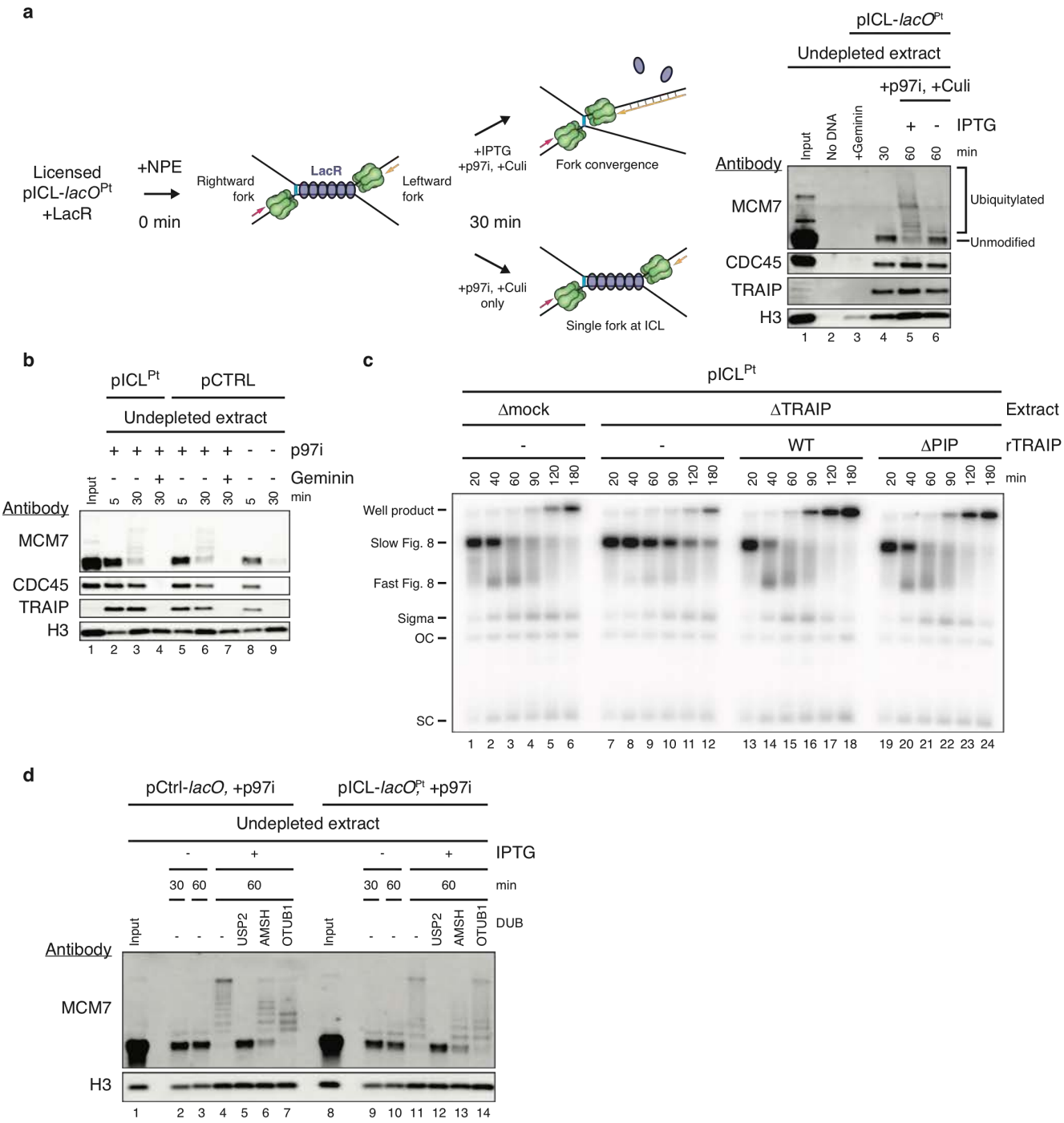
a
Licensed pICL-lacO^Pt +LacR
+NPE
0 min
Rightward fork
LacR
Leftward fork
+IPTG +p97i, +Culi
Fork convergence
30 min
+p97i, +Culi only
Single fork at ICL
pICL-lacO^Pt
Undepleted extract
+p97i, +Culi
Input
No DNA
+Geminin
IPTG
min
Antibody
MCM7
Ubiquitylated
Unmodified
CDC45
TRAIP
H3
b
pICL^Pt
pCTRL
Undepleted extract
p97i
Geminin
min
Antibody
MCM7
CDC45
TRAIP
H3
c
pICL^Pt
Δmock
ΔTRAIP
Extract
rTRAIP
WT
ΔPIP
min
Well product
Slow Fig. 8
Fast Fig. 8
Sigma
OC
SC
d
pCtrl-lacO, +p97i
pICL-lacO;^Pt +p97i
Undepleted extract
IPTG
min
DUB
Input
USP2
AMSH
OTUB1
Antibody
MCM7
H3

Fig. 2 | TRAIP travels with the fork and is activated upon fork convergence

a, Left, experimental scheme. Plasmid containing an ICL flanked by 48 copies of the *lac* operator (*lacO*) (pICL-*lacO*^{Pt}) was incubated with Lac repressor (LacR) prior to replication in egg extracts. After 30 min, IPTG addition dissociated LacR and allowed fork convergence. Right, at the indicated times, pICL-*lacO*^{Pt} was recovered and blotted for the indicated proteins. Culi suppressed CRL2^{LRR1}-dependent ubiquitylation.

b, Chromatin-associated proteins during replication of pICL^{Pt} or pCTRL in the presence or absence of the licensing inhibitor geminin and p97i.

c, pICL^{Pt} was replicated in the indicated extracts and analyzed as in Fig. 1b. TRAIP$^{\Delta PIP}$ comprises residues 1-455.

d, pCtrl-*lacO* and pICL-*lacO*^{Pt} were replicated and recovered as in (**a**). Samples were then treated with the DUBs USP2 (linkage non-specific), AMSH (K63-linkage specific), or OTUB1 (K48-linkage specific) and blotted for the indicated proteins.

Fig. 3

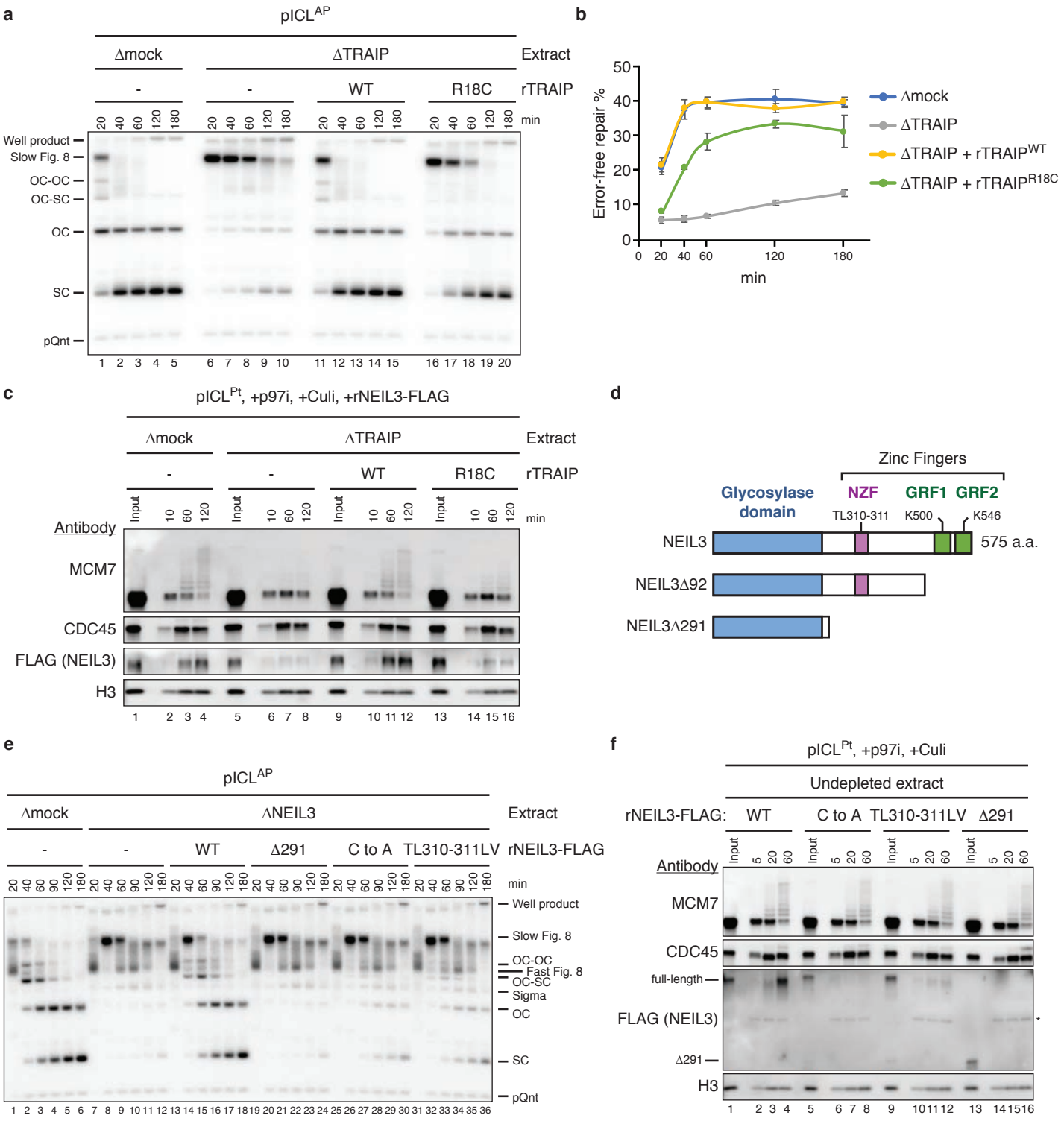
a
pICL^AP
Δmock
ΔTRAIP
Extract
-
-
WT
R18C
rTRAIP
min
Well product
Slow Fig. 8
OC-OC
OC-SC
OC
SC
pQnt
b
Error-free repair %
min
Δmock
ΔTRAIP
ΔTRAIP + rTRAIP^WT
ΔTRAIP + rTRAIP^R18C
c
pICL^Pt, +p97i, +Culi, +rNEIL3-FLAG
Antibody
MCM7
CDC45
FLAG (NEIL3)
H3
Input
d
Zinc Fingers
Glycosylase domain
NZF
GRF1
GRF2
TL310-311
K500
K546
NEIL3
575 a.a.
NEIL3Δ92
NEIL3Δ291
e
pICL^AP
ΔNEIL3
rNEIL3-FLAG
Δ291
C to A
TL310-311LV
Fast Fig. 8
Sigma
f
pICL^Pt, +p97i, +Culi
Undepleted extract
rNEIL3-FLAG:
full-length
Δ291

Fig. 3 | TRAIP promotes NEIL3-dependent ICL repair

a, pICL^{AP} was replicated in the indicated extracts and analyzed as in Fig. 1b.

b, Error-free repair of pICL^{AP} in the indicated extracts, quantified as in Fig. 1e. Error bars, standard error of the mean from three independent experiments.

c and f, Analysis of proteins associated with pICL^{Pt} during replication in the indicated extracts in the presence of p97i and Culi. A non-specifically detected protein is marked with an asterisk.

d, Schematic of WT and mutant *Xenopus* NEIL3 proteins.

e, pICL^{AP} was replicated in the indicated extracts and analyzed as in Fig. 1b.

Fig. 4

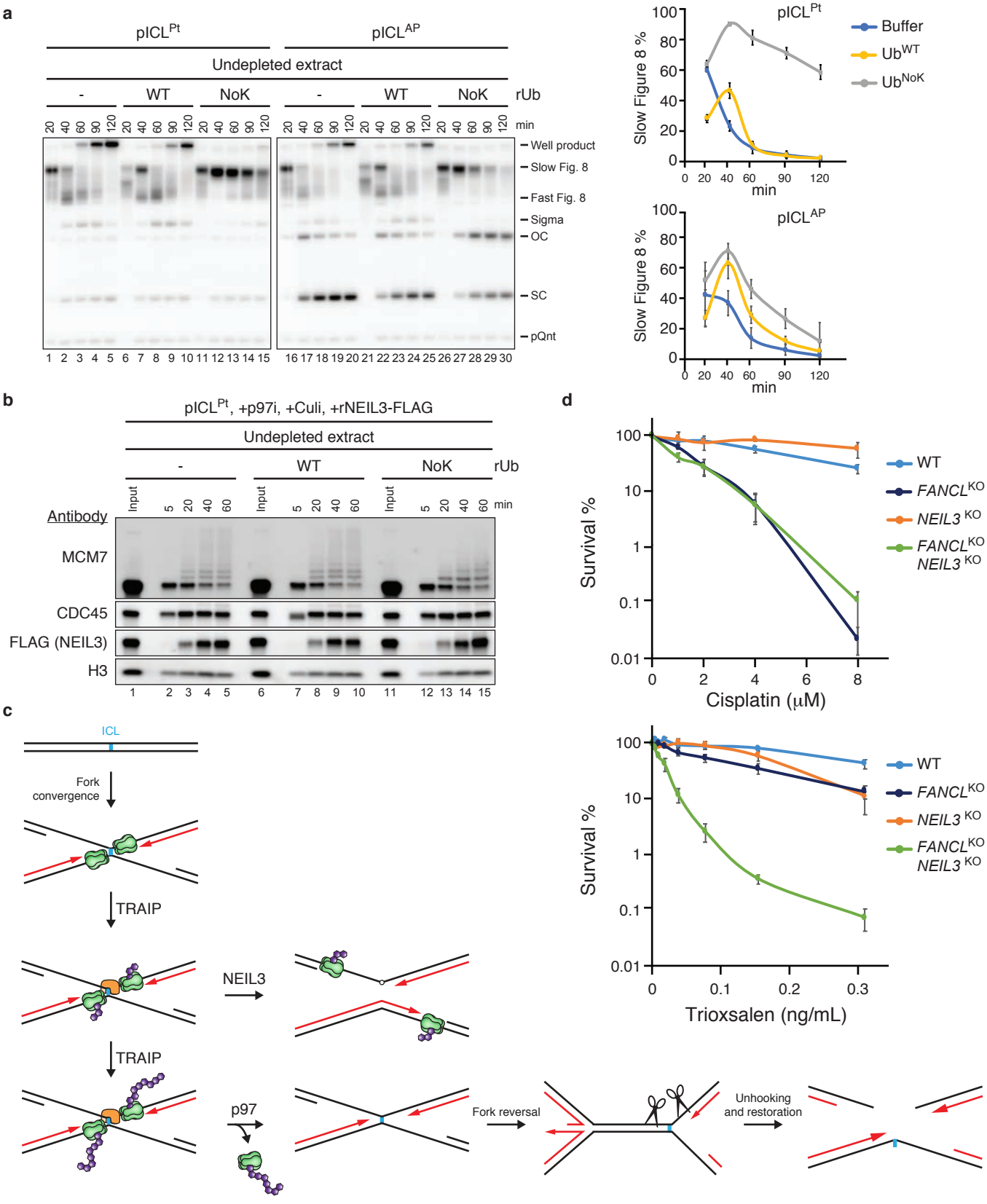
a
pICL^Pt
pICL^AP
Undepleted extract
-
WT
NoK
rUb
min
Well product
Slow Fig. 8
Fast Fig. 8
Sigma
OC
SC
pQnt
Slow Figure 8 %
Buffer
Ub^WT
Ub^NoK
b
pICL^Pt, +p97i, +Culi, +rNEIL3-FLAG
Antibody
MCM7
CDC45
FLAG (NEIL3)
H3
Input
c
ICL
Fork convergence
TRAIP
NEIL3
p97
Fork reversal
Unhooking and restoration
d
Survival %
Cisplatin (μM)
Trioxsalen (ng/mL)
WT
FANCL^KO
NEIL3 ^KO
FANCL^KO NEIL3 ^KO

Fig 4 | MCM7 ubiquitin chain length influences ICL repair pathway choice

a, Left, replication of $pICL^{Pt}$ or $pICL^{AP}$ in the presence of buffer, Ub^{WT}, or Ub^{NoK} was analyzed as in Fig. 1b. Right, quantification of slow Figure 8 structures as a percentage of total replication products. Note that Ub^{WT} and Ub^{NoK} delayed replication by ~20 minutes. Error bars, standard error of the mean from three independent experiments.

b, Proteins associated with $pICL^{Pt}$ during replication in the presence of p97i and Culi and Ub^{WT} or Ub^{NoK}, as indicated.

c, Model for hierarchical activation of the NEIL3 and FA pathways by TRAIP. Green, CMG helicase; purple, ubiquitin; orange, NEIL3.

d, Clonogenic survival of wild-type, *FANCL*, *NEIL3*, or *FANCL*/*NEIL3* CRISPR knockout HAP1 cells after exposure to cisplatin (top) or trioxsalen and UV-A irradiation (bottom). Error bars, standard error of the mean from at least three independent experiments.

Methods:

All experiments were performed at least twice, with a representative result shown.

Preparation of pICL

Preparations of the following plasmids containing site-specific crosslinks were performed as previously described: pICL$^{Pt;\ 2}$, pICL-*lacO*$^{Pt;\ 6}$, and pICL^{AP} and pICL-*lacO*$^{AP;\ 1}$. Briefly, purified cisplatin- or AP-crosslinked oligonucleotide duplexes comprising Pt_Top and PT_Bottom or AP_Top and AP_Bottom, respectively, were ligated into a parental plasmid linearized with BbsI, and the resulting supercoiled plasmid was isolated by cesium chloride gradient.

***Xenopus* Egg Extracts and DNA Replication**

Xenopus egg extracts were prepared essentially as described[27]. For DNA replication, plasmids were licensed by incubation in high-speed supernatant (HSS) of egg cytoplasm at room temperature for 30 min at a final concentration of 7.5 ng pICL/µl extract (for replication intermediate and nascent strand analyses) or 15 ng pICL/µl extract (for plasmid pull-down and electron microscopy analyses) and, where indicated, 0.375 ng pQnt/µl extract. For reactions using pICL-*lacO* plasmids with a pre-assembled LacR array, the plasmid was incubated for 1 hr at room temperature with purified biotinylated LacR[28] at a final concentration of 14 µM prior to licensing as described above. To inhibit licensing, geminin was added to HSS at a final concentration of 10 µM and incubated for 10 min at room temperature prior to addition of DNA. Replication was initiated by addition of two volumes of nucleoplasmic egg extract (NPE). In all figures except Extended Data Fig. 10, the addition of NPE corresponds to the 0 min time point. For nascent strand radiolabeling, reactions were supplemented with trace amounts of [α-^{32}P]dATP. Where indicated, reactions were supplemented with 200 µM NMS-873 p97 inhibitor (Sigma), 200 µM MLN4924 cullin RING ligase inhibitor (Active Biochem), 111 µM RO-3306 CDK1 inhibitor (EMD

343 Millipore), and/or 100 μM recombinant His_6-tagged ubiquitin (Boston Biochem). Reactions were
344 supplemented with approximately 30 to 50 nM recombinant NEIL3-FLAG and 50 to 500 nM
345 recombinant TRAIP, where indicated.

346 **Antibodies and Immunodepletions**

347 Rabbit polyclonal antibodies raised against the following *X. laevis* proteins were previously
348 described: BRCA1[29], CDC45[30], CUL2, LRR1, and TRAIP[20], MCM6 and NEIL3[1], MCM7[30].
349 Rabbit polyclonal FLAG antibody raised against FLAG peptide was prepared by New England
350 Peptide. Rabbit polyclonal antibody raised against human FANCD2 was previously described[31].
351 Histone H3 antibody 9715 was purchased from Cell Signaling, histidine tag antibody AD1.1.10
352 was purchased from Bio-Rad, human NEIL3 antibody 11621-1-AP was purchased from
353 ProteinTech Europe, ubiquitin antibody sc-8017 was purchased from Santa Cruz Biotechnology,
354 and vinculin V284 antibody 05-386 was purchased from EMD Millipore. Immunodepletions of
355 BRCA1[18] and LRR1[20] were performed as previously described. For TRAIP depletions, 2.5
356 volumes of 1 mg/mL protein A Sepharose-purified antibodies against TRAIP were gently rotated
357 with 1 volume of protein A Sepharose beads overnight at 4°C. Five volumes of egg extract were
358 depleted by three rounds of gentle rotation with one volume of antibody-bound beads for 1 hr at
359 4°C. For NEIL3 depletions, 2.5 volumes of 1 mg/mL affinity-purified antibodies against NEIL3
360 were gently rotated with 1 volume of protein A Sepharose beads overnight at 4°C. Five volumes
361 of egg extract were depleted by three rounds of gentle rotation with one volume of antibody-bound
362 beads for 20 min at room temperature. For FANCD2 and NEIL3 double depletion, 3 volumes of
363 1 mg/mL affinity-purified antibodies against NEIL3 were gently rotated with 1 volume of protein
364 A Sepharose beads for 2 hr at 4°C. Three volumes FANCD2 anti-serum were then added to the
365 protein A Sepharose beads and incubation was continued at 4°C overnight. Five volumes of egg

366 extract were depleted by three rounds of gentle rotation with one volume of antibody-bound beads
367 for 20 min at room temperature.

368 **Replication Intermediate Analysis**

369 Replication reactions were stopped at the indicated time points with 10 volumes of Stop Solution
370 A (5% SDS, 80 mM Tris-HCl [pH 8], 0.13% phosphoric acid, 10% Ficoll, and 0.5% bromophenol
371 blue). The reactions were treated with 4 mg/ml Proteinase K (Roche) for 1 hr at 37°C and resolved
372 by 0.8% native agarose gel electrophoresis. The gels were then dried and visualized by
373 phosphorimaging on a Typhoon FLA 7000 (GE Healthcare).

374 **Nascent Strand Analysis**

375 Replication reactions were stopped at the indicated time points with 10 volumes of Stop Solution
376 B (0.5% SDS, 50 mM Tris-HCl [pH 7.5], and 25 mM EDTA [pH 8.0]). The reactions were treated
377 with 0.16 mg/ml RNase A for 1 hr at 37°C, followed by 0.75 mg/ml Proteinase K overnight at
378 room temperature. The reactions were then phenol/chloroform extracted, precipitated, and digested
379 with AflIII for 3 hr at 37°C. After addition of denaturing PAGE Gel Loading Buffer II (Life
380 Technologies), the radiolabeled nascent strands were resolved on a 7% denaturing polyacrylamide
381 gel, transferred to filter paper, dried, and visualized by phosphorimaging on a Typhoon FLA 7000
382 (GE Healthcare). Sequencing gel markers were generating using the Thermo Sequenase Cycle
383 Sequencing Kit (USB Corporation) with primer pICL_Seq that anneals with the pICL plasmids
384 149 nucleotides upstream of the crosslink.

385 **Plasmid Pull-down**

386 Plasmid pull-downs were performed essentially as described[32]. Briefly, streptavidin-coupled
387 magnetic beads (Invitrogen) were gently rotated with biotinylated LacR[28] for 40 min at room

temperature. The beads were washed three times with 20 mM HEPES-KOH (pH 7.7), 100 mM KCl, 5 mM $MgCl_2$, 250 mM sucrose, 0.25 mg/ml BSA, and 0.02% Tween-20, then resuspended in the same buffer. Replication reactions were mixed with the beads at the indicated times and gently rotated for 30 min at 4°C. The beads were washed three times with 20 mM HEPES-KOH (pH 7.7), 100 mM KCl, 5 mM $MgCl_2$, 0.25 mg/ml BSA, and 0.03% Tween-20, then resuspended in 2x Laemmli buffer for analysis by immunoblotting.

Ubiquitin linkage analysis

Analysis of ubiquitin chains on MCM7 was performed using UbiCrest deubiquitinase enzyme set (Boston Biochem). Plasmid pull downs were performed as described above, except that the beads were resuspended in 1x DUB reaction buffer and then incubated with 1x USP2, 2x GST-AMSH, or ~8 μM Otubain1 (OTUB1) for 2 h at 37 °C. Reactions were quenched with an equal volume 2x Laemmli buffer and analyzed by immunoblotting.

Immunoblotting

Samples were resolved on Mini-PROTEAN or Criterion TGX precast gels (Bio-Rad) and transferred to PVDF membranes (Perkin Elmer). Membranes were blocked in 5% nonfat milk in 1x PBST for 60 min at room temperature, then incubated with antibody diluted in 1x PBST containing 1% BSA overnight at 4°C. After extensive washing in 1x PBST at room temperature, the membranes were incubated with goat anti-rabbit horseradish peroxidase-conjugated antibodies (Jackson ImmunoResearch) diluted in 5% nonfat milk in 1x PBST for 1 hr at room temperature. Membranes were washed extensively in 1x PBST, briefly incubated with HyGLO chemiluminescent HRP antibody detection reagent (Denville), and imaged using an Amersham Imager 600 (GE Healthcare).

410 **Error-Free Repair Assay**

411 The error-free repair assay was performed as previously described[33]. Briefly, replication reactions
412 were stopped at the indicated time points with 10 volumes of Stop Solution B. The reactions were
413 treated with 0.16 mg/ml RNase A for 1 hr at 37°C, followed by 0.75 mg/ml Proteinase K overnight
414 at room temperature. The reactions were then phenol/chloroform extracted, precipitated, and
415 digested with HincII or HincII and SapI for 3 hr at 37°C. After addition of 0.17 volumes of DNA
416 loading buffer (10 mM Tris-HCl [pH 7.5], 60% glycerol, and 0.5% bromophenol blue), the
417 digestion products were resolved by 0.8% native agarose gel electrophoresis, dried, and visualized
418 by phosphorimaging on a Typhoon FLA 7000 (GE Healthcare). Repair products were quantified
419 using ImageJ (NIH).

420 **Purification of Recombinant *Xenopus* NEIL3 and TRAIP**

421 *X. laevis* NEIL3 was purified as previously described[1]. Briefly, constructs for expression of
422 rNEIL3$^{\text{NZF-C to A}}$, rNEIL3$^{\text{TL310-311LV}}$, rNEIL3$^{\text{K500E}}$, rNEIL3$^{\text{K546E}}$, rNEIL3$^{\text{K500E K546E}}$, and rNEIL3$^{\Delta 92}$
423 were prepared by digesting Integrated DNA Technologies gene blocks encompassing the C-
424 terminal domain of NEIL3 (with FLAG epitope tag) and containing the indicated mutations with
425 BbvCI and XhoI and then ligating the fragments into similarly digested pFastBac1-NEIL3-FLAG[1].
426 The rNEIL3$^{\Delta 291}$ expression construct was prepared by PCR amplifying the NEIL3 glycosylase
427 domain from a *X. laevis* cDNA library (a gift from T.G.W. Graham) using primers NEIL3_291_A
428 and NEIL3_291_B. The fragment was then digested with EcoRI and XhoI and ligated into
429 similarly digested pFastBac1 (Thermo Fisher Scientific). All mutations and truncations were
430 confirmed by Sanger sequencing. Baculoviruses expressing rNEIL3 were then prepared using
431 the Bac-to-Bac system (Thermo Fisher Scientific) according to the manufacturer's protocols.
432 rNEIL3 protein was expressed in 250 ml suspension cultures of Sf9 insect cells (Expression

Systems) by infection with baculovirus expressing NEIL3-FLAG for 48 to 72 hr. Sf9 cells were collected and suspended in 10 ml NEIL3 Lysis Buffer (50 mM Tris-HCl [pH 7.5], 300 mM NaCl, 10% glycerol, 1x Roche EDTA-free cOmplete protease inhibitor cocktail, 0.5 mM PMSF, and 0.2% Triton X-100). Cells were lysed by sonication, and the soluble fraction was collected by spinning the lysate at 25,000 rpm in a Beckman SW41 rotor for 1 hr. The soluble lysate was incubated with 200 µl anti-FLAG M2 affinity resin (Sigma) for 90 min at 4°C. The resin was washed once with 10 ml Lysis Buffer, twice with NEIL3 Wash Buffer (50 mM Tris-HCl [pH 7.5], 300 mM NaCl, 10% glycerol, and 0.2% Triton X-100), and three times with Buffer A (50 mM Tris-HCl [pH 7.5], 300 mM NaCl, and 10% glycerol). NEIL3-FLAG protein was eluted from the resin with Buffer A containing 100 µg/ml 3x FLAG peptide (Sigma). Elution fractions containing NEIL3-FLAG protein were pooled and dialyzed against 50 mM HEPES-KOH (pH 7.0), 300 mM NaCl, 1 mM DTT, and 20% glycerol at 4°C for 12 hr and then dialyzed against 50 mM HEPES-KOH (pH 7.0), 150 mM NaCl, 1 mM DTT, and 15% glycerol at 4°C for 3 hr. Aliquots of protein were stored at −80°C. Constructs for expression of GST-TEV-NZF fusion proteins were prepared by PCR amplifying the NEIL3 NZF from pFastBac1-NEIL3-FLAG and pFastBac1-NEIL3$^{TL310-311LV}$-FLAG using primers NEIL3_NZF_A and NEIL3_NZF_B. The pGEX-6P-1 backbone (with GST-TEV tag) was PCR amplified from pGEX-6P-1-GST-TEV-FLAG-UBXN7 with primers GST_A and GST_B. The resulting fragments were then assembled using the NEBuilder HiFi DNA assembly cloning kit (New England Biolabs) according to the manufacturer's instructions. Expression of GST-TEV-NZF proteins was induced in 1 L Rosetta 2 (DE3) pLysS cells (Novagen) with 0.5 mM IPTG for 3 hr at 37°C. Bacterial cell pellets were suspended in Buffer A (10 mM Sodium Phosphate [pH 7.4], 150 mM NaCl, 5 mM β-mercaptoethanol, 10 µM $ZnCl_2$ and 1x Roche cOmplete protease inhibitor cocktail) and sonicated. The soluble lysate was collected following

centrifugation at 25,000 rpm in SW40.1 rotor for 1 hr and bound to Glutathione Sepharose 4B (GE Healthcare) for 1.5 hr at 4°C. The bound resin was then washed five times with Buffer A and protein was eluted with Buffer B (50 mM Tris-HCl [pH 8.0], 150 mM NaCl, 10 μM $ZnCl_2$, 5 mM β-mercaptoethanol, and 20 mM glutathione). Fractions containing GST-TEV-NZF fusion proteins were dialyzed against 50 mM Tris-HCl (pH 8.0), 150 mM NaCl, 10 μM $ZnCl_2$, 5 mM β-mercaptoethanol, and 10% glycerol at 4°C and aliquots were stored at -80°C. Constructs for expression of MBP-TEV-GRF ZF fusion proteins were prepared by amplifying the NEIL3 GRF ZF1 or GRF ZF2 from pFastBac1-NEIL3-FLAG or pFastBac1-NEIL3$^{K500E\ K546E}$-FLAG using primers GRFZF1_A and GRFZF1_B or GRFZF2_A and GRFZF2_B, respectively. The MBP tag was PCR amplified using the primers MBP_A and MBP_B or MBP_A and MBP_C for GRF ZF1 and GRF ZF2 respectively. The pGEX-6P-1 backbone was PCR amplified from pGEX-6P-1-GST-TEV-FLAG-UBXN7 with primers pGEX_A and pGEX_B. The resulting fragments were then assembled using the NEBuilder HiFi DNA assembly cloning kit (New England Biolabs) according to the manufacturer's instructions. Expression of MBP-TEV-GRF ZF proteins was induced in 1 L Rosetta 2 (DE3) pLysS cells (Novagen) with 0.5 mM IPTG for 3 hr at 37°C. Bacterial cell pellets were suspended in Buffer C (20 mM Tris-HCl [pH 7.5], 300 mM NaCl, 1 mM DTT, and 1x Roche cOmplete protease inhibitor cocktail) and sonicated. The soluble lysate was collected following centrifugation at 25,000 rpm in a SW40.1 rotor for 1 hr and bound to amylose resin (New England Biolabs) for 1.5 hr at 4°C. The bound resin was then washed six times with Buffer C and protein was eluted with Buffer C containing 10 mM maltose. Fractions containing MBP-TEV-GRF ZF fusion proteins were dialyzed against 20 mM Tris-HCl (pH 8.0), 200 mM NaCl, 1 mM DTT, and 10% glycerol at 4°C and aliquots were stored at -80°C.

The *X. laevis* TRAIP ORF was PCR amplified from a *X. laevis* cDNA library (a gift from T.G.W. Graham) using primers TRAIP_A and TRAIP_B. The amplified product was gel isolated, digested with BamHI, and ligated into pH_6-SUMO[34] linearized with BamHI. The R18C substitution was introduced by "around-the-horn" PCR[35] using primers R18C_A and R18C_B. pH_6-SUMO-TRAIP$^{\Delta PIP}$ (residues 1-455) was constructed by "around-the-horn" PCR using primers PIP_A and PIP_B. His_6-SUMO-TRAIP was expressed in Rosetta 2 (DE3) pLysS (Novagen) by induction with 0.1 mM IPTG overnight at 16°C in growth media supplemented with 50 μM $ZnSO_4$. Bacterial pellets were resuspended in TRAIP Lysis Buffer (20 mM HEPES-NaOH [pH 7.5], 400 mM sodium acetate, 10% glycerol, 20 mM imidazole, 10 μM $ZnSO_4$, 0.1% NP-40, 1 mM DTT, and 1x Roche cOmplete protease inhibitor cocktail). Following sonication, ammonium sulfate and polyethyleneimine were added to the lysate to final concentrations of 300 mM and 0.45%, respectively and incubated for 15 min at 4°C. The soluble fraction was collected after centrifugation at 40,000g for 45 min at 4°C, and precipitated with saturating ammonium sulfate. The precipitated fraction was collected after centrifugation at 40,000g for 45 min at 4°C, resuspended in Lysis Buffer, and then rotated with NiNTA resin (Qiagen) for 30 min at room temperature. The resin was washed three times with Wash Buffer (20 mM HEPES-NaOH [pH 7.5], 400 mM sodium acetate, 10% glycerol, 20 mM imidazole, 10 μ M $ZnSO_4$, 0.01% NP-40, 1 mM DTT, and 1x Roche cOmplete protease inhibitor cocktail). His_6-SUMO-TRAIP was eluted from the resin with Elution Buffer (20 mM HEPES-NaOH [pH 7.5], 400 mM sodium acetate, 10% glycerol, 250 mM imidazole, 0.01% NP-40, and 1 mM DTT). Elution fractions containing His_6-SUMO-TRAIP were pooled and dialyzed against Dialysis Buffer (20 mM HEPES-NaOH [pH 7.5], 400 mM sodium acetate, 10% glycerol, 120 mM imidazole, 0.01% NP-40, and 1 mM DTT) overnight at 4°C. With the exception of the proteins used in Fig. 2c and Extended Data Fig. 6, the

501 His_6-SUMO was simultaneously cleaved by addition of 0.03 mg/mL Ulp1 during dialysis.
502 Aliquots were flash frozen and stored at -80°C.

503 **Ubiquitin Ligase Activity Assay**

504 The ubiquitin ligase activity assay using an equimolar mixture of the E2 ubiquitin conjugating
505 enzymes UbcH5a, UbcH5b, and UbcH5c and recombinant $TRAIP^{WT}$ or $TRAIP^{R18C}$ at an
506 approximate final concentration of 70 nM was performed using the Enzo BML-UW9920
507 Ubiquitinylation Kit according to manufacturer's instructions (Enzo Life Sciences).

508 **Electron Microscopy**

509 Electron microscopy analysis of the replication intermediates was performed as previously
510 described[8]. Briefly, replication reactions were stopped at 90 min with 10 volumes of Stop Solution
511 C (100 mM Tris-HCl [pH 7.5], 6.7 mM $MgCl_2$, 1 mM EDTA [pH 8.0], and 1% SDS). The DNA
512 was crosslinked with trimethylpsoralen (Sigma) and irradiation with UV light at 365 nM prior to
513 protein extraction and DNA purification. Purified DNA was incubated with E. coli single-stranded
514 DNA binding protein (SSB), fixed with 0.3% glutaraldehyde, then purified by size-exclusion
515 chromatography. Eluted complexes were mounted onto grids, which were then subjected to rotary
516 shadowing with platinum and carbon coating using a Leica Ace600 coating system. Samples were
517 imaged using a JEOL 1200EX transmission electron microscope equipped with a 2k CCD camera
518 (Advanced Microscopy Techniques). After blinding the scorer to the conditions, reversed forks
519 were counted and expressed as a percentage of pre-incision structures, which was then normalized
520 to the mock-depleted condition.

521 **Electrophoretic Mobility Shift Assay**

MBP-TEV-GRF ZF fusion protein was incubated with 10 nM 5' end radiolabeled 25mer ssDNA (EMSA_Top) or dsDNA (EMSA_Top + EMSA_Bottom) in buffer containing 1 mM $MgCl_2$, 100 μM $ZnSO_4$, 10 mM Tris-HCl (pH 8.0), 50 mM NaCl, 0.2 mM TCEP, and 5% glycerol for 30 to 60 min at 4 °C. Binding reactions were separated on native 5% acrylamide (37.5:1), 45 mM Tris, 45 mM borate, 1 mM $MgCl_2$, 100 μM $ZnSO_4$ gels and visualized by phosphorimaging on a Typhoon FLA 7000 (GE Healthcare).

NEIL3 Glycosylase Assay

AP-ICLs between complementary DNA and DNA/RNA chimeric oligonucleotides AP_assay_A and AP_assay_B were cross-linked, RNase digested, and gel purified as described[1]. To monitor unhooking of AP-ICLs, 2.5 nM 5′ radiolabeled cross-linked substrate was incubated with 20 nM rNEIL3-FLAG in 20 mM HEPES-KOH (pH 7.0), 50 mM NaCl, 1 mM DTT, 0.1 mg/ml BSA at 37°C[36]. Reactions were quenched with 1 volume of 2x formamide buffer (86% formamide, 2x TBE, 20 mM EDTA [pH 8.0]), separated on a denaturing polyacrylamide and visualized by phosphorimaging on a Typhoon FLA 7000 (GE Healthcare).

Biolayer Interferometry

All measurements were obtained using an OctetRED384 instrument (Pall ForteBio). Samples in 0.2 mL BLI buffer (1x PBS, 0.1 mg/mL BSA, and 0.05% Tween 20) were dispensed into polypropylene 96-well black flat-bottom plates (Greiner Bio-One). GST-TEV-NZF or GST control protein (30 μg/mL) was captured on pre-wet anti-GST biosensors (Pall ForteBio). Biosensors were then transferred to wells containing BLI buffer to allow dissociation of non-specifically bound GST-TEV-NZF protein and establish a measurement base-line. Biosensors were next transferred to wells containing serial dilutions of monoubiquitin (Boston Biochem) to monitor association of ubiquitin with the immobilized GST-TEV-NZF protein. Finally, biosensors

were transferred to wells containing BLI buffer to monitor dissociation of ubiquitin from GST-TEV-NZF protein. For each ubiquitin concentration, the steady state ubiquitin binding response (R_{eq}) was determined from a five second window at the end of the association phase. R_{eq} values were subsequently corrected for non-specific binding of ubiquitin to the GST epitope by subtracting R_{eq} values obtained for the GST control protein. Steady-state responses were plotted as a function of ubiquitin concentration ([Ub]) and K_d was determined using the Prism software suite by fitting the data to the non-linear regression equation $R_{eq} = \frac{R_{max} \times [\mathrm{Ub}]}{[\mathrm{Ub}] + K_d}$ where R_{max} is the globally-constrained maximum association response.

Cell Lines

Wild-type and *NEIL3*^{KO} HAP1 near-haploid human cells were purchased from Horizon Discovery and cultured at 37˚C and 5% CO2 in IMDM (Gibco) supplemented with 10% fetal calf serum (Gibco) and penicillin/streptomycin (Gibco). *NEIL3*^{KO} cells were confirmed by immunoblotting against NEIL3. For targeting of *FANCL*, WT and *NEIL3*^{KO} cells were transfected with Turbofectin 8.0 (Origene) and the following plasmids: pX461, FANCL_left and FANCL_right CRISPR guides in U6 BsaI backbone, and *FANCL*-Puro targeting construct (Extended Data Fig. 13b). *FANCL* plasmids were obtained from the Wellcome Trust Sanger Institute. Two days post-transfection, 3.5 µg/mL puromycin (Gibco) was added, and two days later, cells were plated in 96-well plates with puromycin. After 14 days of incubation, individual clones were picked and analyzed for *FANCL* targeting using the SequalPrep Long PCR kit (Applied Biosystems) (see Supplementary Table 1 for primer sequences). Targeted clones were then plated with 100 ng/mL mitomycin C (Sigma) overnight and analyzed by immunoblotting for FANCD2. *FANCL* knockouts were identified by failure to ubiquitinate FANCD2. All cell lines were tested to be mycoplasma negative using the MycoAlert Mycoplasma Detection Kit (Lonza).

Colony Survival Assay

For the cisplatin colony survival assay (CSA), HAP1 cells were prepared at $2x10^5$ cells/mL. Cells and cisplatin (diluted in culture media) were mixed in 96-well blocks (Greiner Bio-One Masterblock) and foil seals (Bio-Rad Microseal 'F') were applied before culturing cells at 37˚C for 2 hr. Cells were then serially diluted in PBS using a multi-channel pipette to obtain 1:10 and 1:100 dilutions, and 100 µL of each of three concentrations were plated in duplicate in 24-well plates filled with 1.5 mL of culture media per well. Cells were cultured for 6 days before being stained with crystal violet[37] and colonies were quantified by a GelCount colony counter (Oxford Optronix).

For the trioxsalen CSA, cells were seeded in 24-well plates at $1.2x10^5$ cells per well 5 hr prior to adding trioxsalen (Sigma) and cultured for 1 hr. Cells were then exposed to 6 kJ/m^2 of UV-A light (365 nm, VL-6.L lamp) through the bottom of the tissue culture plate to photoactivate trioxsalen. The cells were washed twice with culture media, incubated at 37˚C for 10 min to offload unbound trioxsalen, then washed again and treated with 12 kJ/min/m^2 UV-A to convert trioxsalen monoadducts into ICLs[38,39]. Cells were then trypsinized, diluted, plated, cultured, and

References:

27 Lebofsky, R., Takahashi, T. & Walter, J. C. DNA replication in nucleus-free Xenopus egg extracts. *Methods Mol Biol* **521**, 229-252 (2009).

28 Dewar, J. M., Budzowska, M. & Walter, J. C. The mechanism of DNA replication termination in vertebrates. *Nature* **525**, 345-350, doi:10.1038/nature14887 (2015).

29 Joukov, V., Chen, J., Fox, E. A., Green, J. B. & Livingston, D. M. Functional communication between endogenous BRCA1 and its partner, BARD1, during Xenopus laevis development. *Proc Natl Acad Sci U S A* **98**, 12078-12083 (2001).

30 Walter, J. & Newport, J. Initiation of eukaryotic DNA replication: origin unwinding and sequential chromatin association of Cdc45, RPA, and DNA polymerase alpha. *Mol Cell* **5**, 617-627 (2000).

31 Rosado, I. V., Langevin, F., Crossan, G. P., Takata, M. & Patel, K. J. Formaldehyde catabolism is essential in cells deficient for the Fanconi anemia DNA-repair pathway. *Nat. Struct. Mol. Biol* **18**, 1432-1434, doi:10.1038/nsmb.2173 (2011).

32 Budzowska, M., Graham, T. G., Sobeck, A., Waga, S. & Walter, J. C. Regulation of the Rev1-pol zeta complex during bypass of a DNA interstrand cross-link. *EMBO J* **34**, 1971-1985, doi:10.15252/embj.201490878 (2015).
33 Knipscheer, P., Raschle, M., Scharer, O. D. & Walter, J. C. Replication-coupled DNA interstrand cross-link repair in Xenopus egg extracts. *Methods Mol Biol* **920**, 221-243, doi:10.1007/978-1-61779-998-3_16 (2012).
34 Graham, T. G., Walter, J. C. & Loparo, J. J. Two-Stage Synapsis of DNA Ends during Non-homologous End Joining. *Mol Cell* **61**, 850-858, doi:10.1016/j.molcel.2016.02.010 (2016).
35 Hemsley, A., Arnheim, N., Toney, M. D., Cortopassi, G. & Galas, D. J. A simple method for site-directed mutagenesis using the polymerase chain reaction. *Nucleic Acids Res* **17**, 6545-6551 (1989).
36 Liu, M. *et al.* The mouse ortholog of NEIL3 is a functional DNA glycosylase in vitro and in vivo. *Proc Natl Acad Sci U S A* **107**, 4925-4930, doi:10.1073/pnas.0908307107 (2010).
37 Franken, N. A., Rodermond, H. M., Stap, J., Haveman, J. & van Bree, C. Clonogenic assay of cells in vitro. *Nat Protoc* **1**, 2315-2319, doi:10.1038/nprot.2006.339 (2006).
38 Vos, J. M. & Hanawalt, P. C. Processing of psoralen adducts in an active human gene: repair and replication of DNA containing monoadducts and interstrand cross-links. *Cell* **50**, 789-799 (1987).
39 Derheimer, F. A., Hicks, J. K., Paulsen, M. T., Canman, C. E. & Ljungman, M. Psoralen-induced DNA interstrand cross-links block transcription and induce p53 in an ataxia-telangiectasia and rad3-related-dependent manner. *Mol Pharmacol* **75**, 599-607, doi:10.1124/mol.108.051698 (2009).

Extended Data Fig. 1

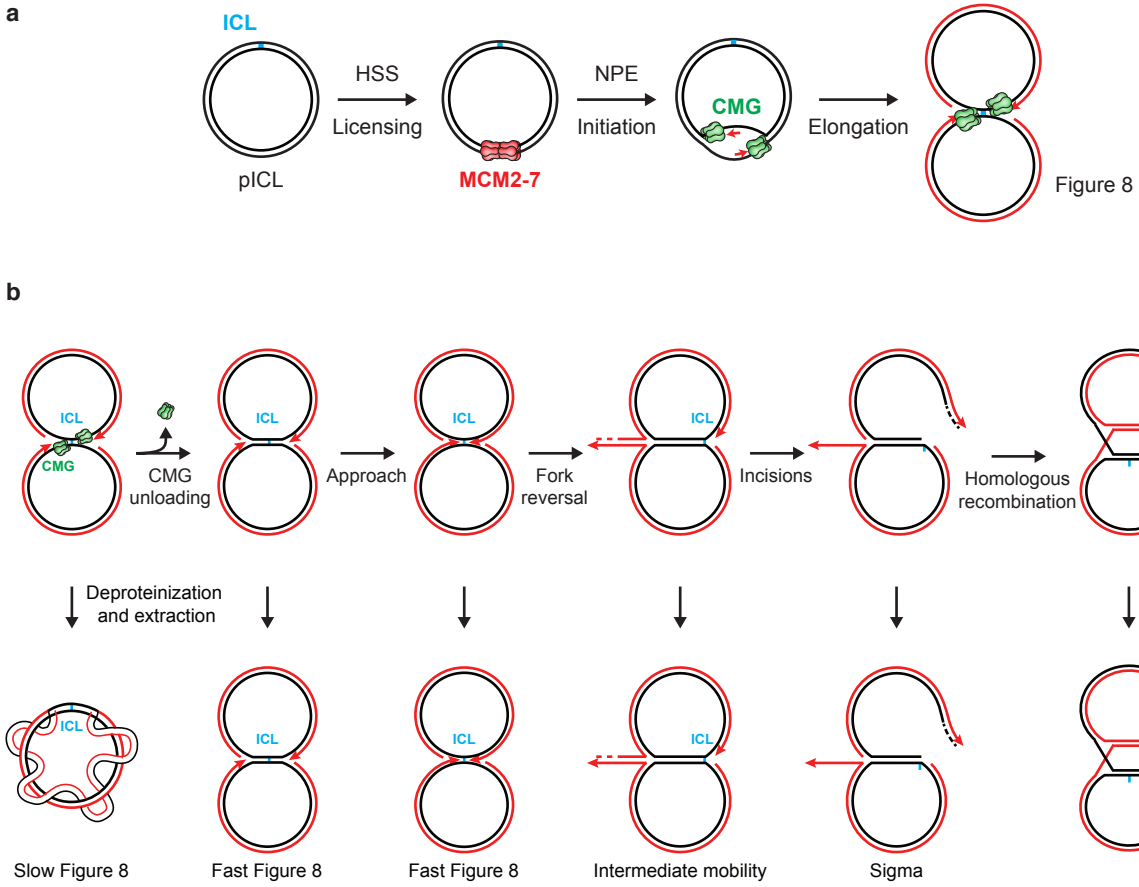

Extended Data Fig. 1 | DNA replication and cisplatin-ICL repair in Xenopus egg extracts

a, Schematic of pICL replication in the nucleus-free *Xenopus* egg extract system[40]. Incubation of the plasmid in HSS supports the recruitment of inactive MCM2-7 double hexamers (red hexamers; "Licensing"). Addition of NPE activates replication initiation, including the assembly of active CMG helicases (green hexamers), and elongation of nascent strands (red lines).

b, Intermediates generated during replication-coupled repair of a cisplatin-ICL. Top, progression through the incision-dependent Fanconi anemia repair pathway generates distinct intermediates resulting from fork convergence, CMG unloading, leading strand approach to the ICL, fork reversal, incisions, and repair of the double strand break by homologous recombination. Bottom, deproteinization of the DNA intermediates depicted along the top yields DNA structures that travel with characteristic mobilities during native agarose gel electrophoresis, as indicated along the side of the gel in Fig. 1b. The slow Figure 8 arises upon fork convergence on the ICL. Conversion of slow to fast Figure 8s results from CMG unloading and an accompanying change in plasmid topology[8]. Next, a species of intermediate mobility appears (Fig. 1b, green arrowhead), which represents reversed forks, as shown by electron microscopy[8]. Following XPF-dependent unhooking of the reversed structure[8,41], double-strand DNA break repair generates joining products that barely enter the gel[18] (Fig, 1b, Well product). Some of these species are resolved into monomeric, supercoiled plasmids that represent the final, fully repaired product (Fig. 1b, SC) that is sensitive to SapI digestion.

Extended Data Fig. 2

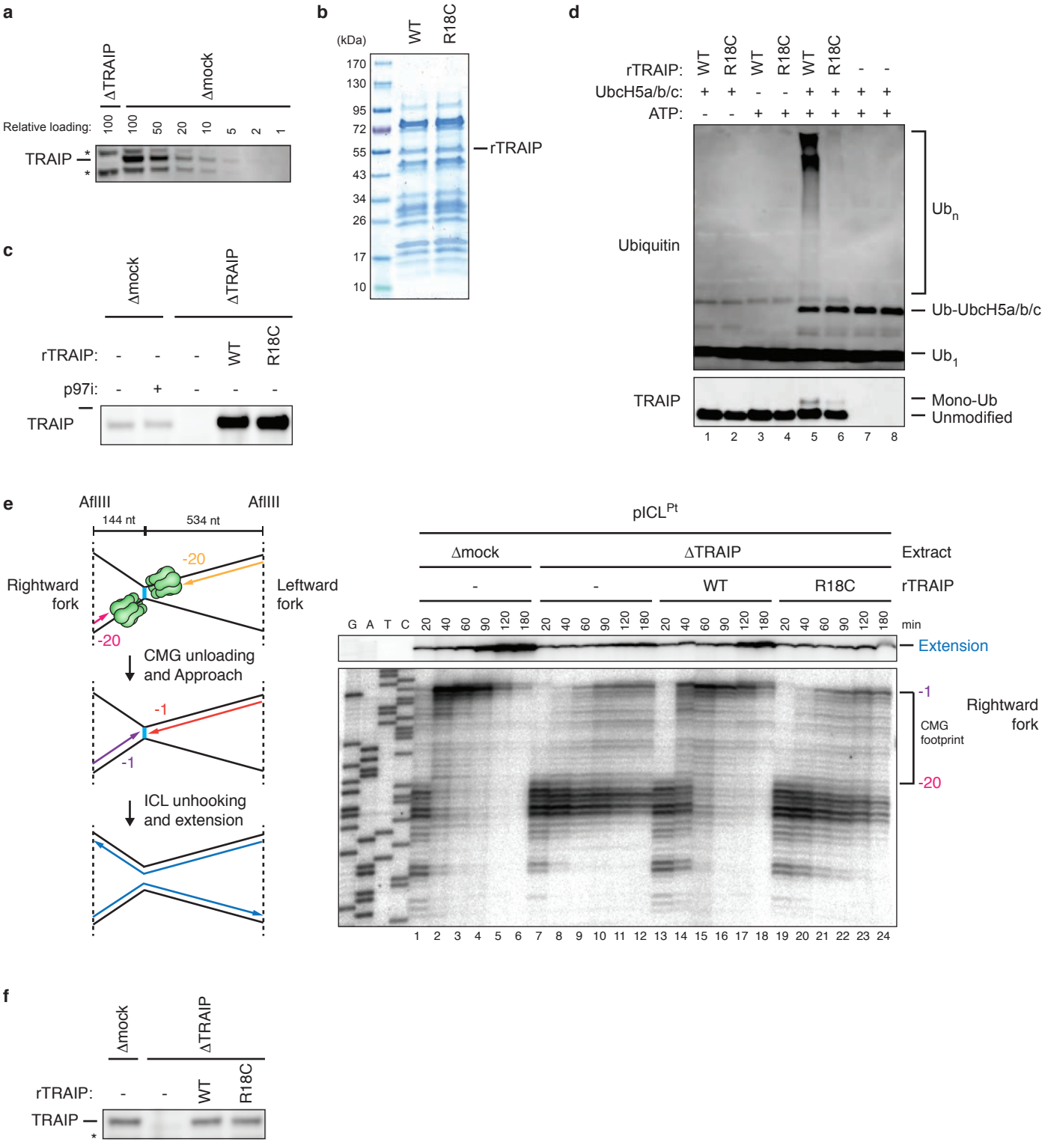

Extended Data Fig. 2 | Recombinant TRAIP supports the disappearance of the CMG footprint at cisplatin-ICLs

a, NPE immunodepleted of TRAIP was loaded alongside a dilution series of mock-depleted NPE and blotted for TRAIP. A relative loading amount of 100 corresponds to 2 µl of NPE. Non-specifically detected proteins are marked with asterisks.

b, Bacterially-expressed rTRAIP^{WT} and rTRAIP^{R18C}. The recombinant proteins were partially purified, resolved by SDS-PAGE, and visualized with Coomassie Brilliant Blue staining.

c, Mock- and TRAIP-depleted extracts supplemented with rTRAIP^{WT} or rTRAIP^{R18C} used in the replication reaction shown in Fig. 1b were analyzed as in **a**. The lack of non-specific bands may be due to shorter incubation with the TRAIP antibody.

d, Ubiquitin ligase activity of the rTRAIP shown in **b**. Recombinant TRAIP^{WT} or rTRAIP^{R18C} was combined with ubiquitin, E1, three E2s (UbcH5a, UbcH5b, and UbcH5c), and ATP as indicated. Polyubiquitin chain synthesis (top gel) and TRAIP autoubiquitylation (bottom gel) were detected by immunoblotting the reactions with ubiquitin and TRAIP antibody, respectively.

e, Left, schematic of nascent strands generated at ICLs. When forks converge on an ICL, nascent strands stall ~20 nt from the ICL on either side of the lesion due to the footprint of CMG (green hexamer). AflIII cuts 144 nt to the left of the ICL and 534 nt to the right of the ICL, generating characteristic products for the leftward and rightward leading strands upon fork convergence, CMG unloading, and leading strand extension. Right, nascent strand analysis of pICL^{Pt} replication in the indicated extracts. After replication with [α-^{32}P]dATP and AflIII digestion, nascent strands were extracted and resolved on a denaturing polyacrylamide gel alongside a sequencing ladder and visualized by autoradiography. Top, extension products. Bottom, nascent strands of the rightward fork. As seen previously[2,42], when replication forks converged on the ICL in mock-depleted egg

extracts, leading strands initially stalled 20-40 nucleotides (nt) from the lesion (lane 1) and then advanced to the -1 position (lanes 2-6), which depends on CMG dissociation[18,42]. In contrast, in TRAIP-depleted egg extracts, the -20 footprint persisted for three hours (lanes 7-12). The same defect was seen for the leftward fork (data not shown). This effect was rescued with rTRAIP^{WT} but not rTRAIP^{R18C} (lanes 13-24).

f, Mock- and TRAIP-depleted extracts supplemented with rTRAIP^{WT} or rTRAIP^{R18C} used in the replication reaction shown in **e** were analyzed as in **a**.

Extended Data Fig. 3

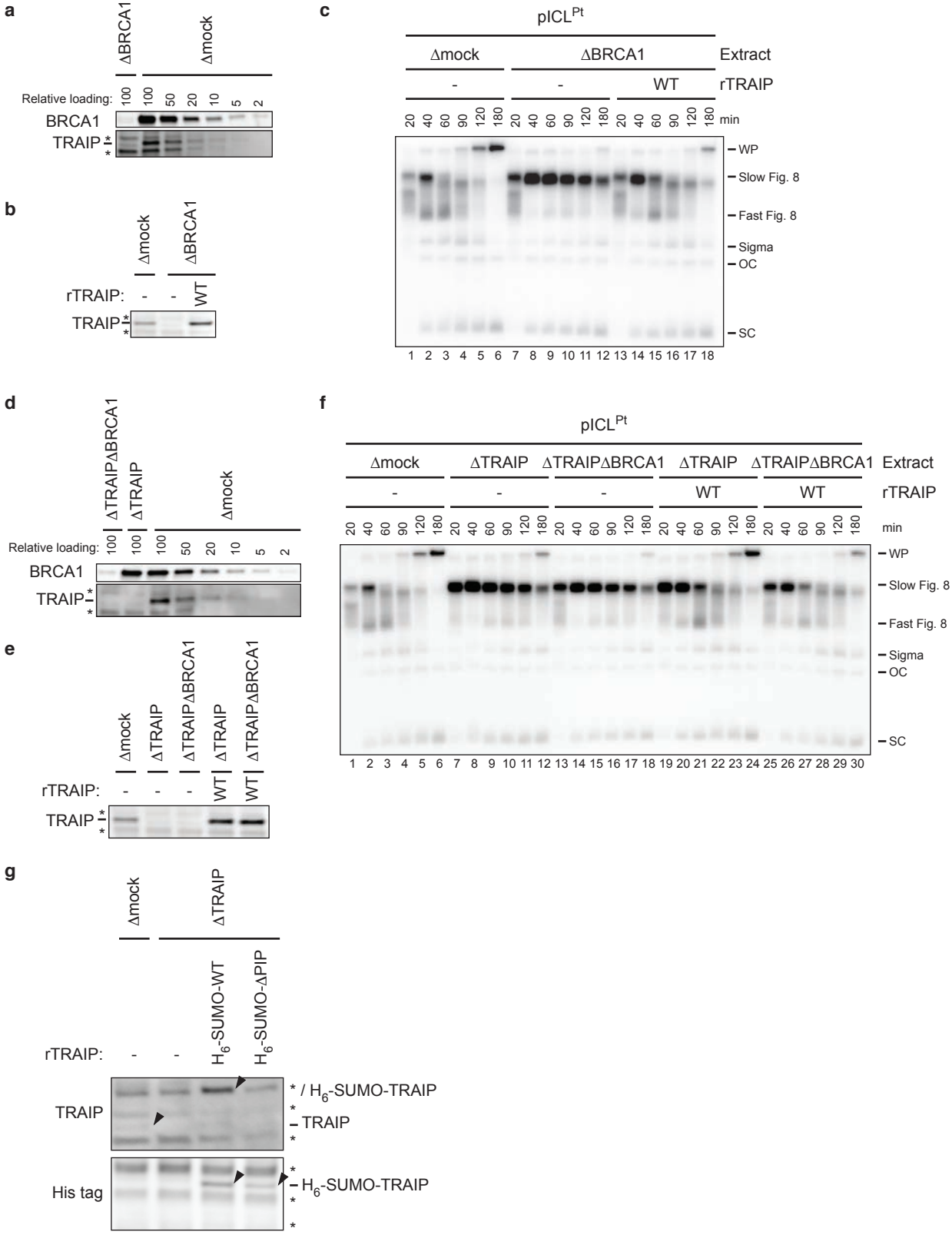

Extended Data Fig. 3 | BRCA1 and the TRAIP PIP box do not contribute to CMG unloading at ICLs

We previously showed that the immunodepletion of BRCA1 from egg extracts inhibits CMG unloading at ICLs, but this defect could not be rescued with recombinant BRCA1-BARD1 complex[7,18].

a, To test wheter TRAIP is co-depleted with BRCA1, NPE was immunodepleted of BRCA1, loaded alongside a dilution series of mock-depleted NPE, and blotted for BRCA1 and TRAIP. A relative loading amount of 100 corresponds to 2 µl of NPE. Non-specifically detected proteins are marked with asterisks. This analysis revealed that immunodepletion of BRCA1 co-depletes TRAIP from NPE.

b, Mock- or BRCA1-depleted extracts supplemented with $rTRAIP^{WT}$ were blotted for TRAIP.

c, $pICL^{Pt}$ was replicated in the indicated egg extracts with [α-^{32}P]dATP and analyzed as in Fig. 1b. $rTRAIP^{WT}$ suppressed the stabilization of the slow Figure 8 species seen in BRCA1-depleted extract, consistent with the restoration of CMG unloading.

d, To determine whether TRAIP-dependent CMG unloading is enhanced by BRCA1, NPE was immunodepleted of TRAIP or TRAIP and BRCA1. A dilution series of mock-depleted NPE was loaded alongside the depleted extracts, and extracts were blotted for BRCA1 and TRAIP. A relative loading amount of 100 corresponds to 2 µl of NPE.

e, Extracts in **d** were supplemented with $rTRAIP^{WT}$, as indicated, and blotted for TRAIP.

f, $pICL^{Pt}$ was replicated in the indicated egg extracts with [α-^{32}P]dATP and analyzed as in Fig. 1b. $rTRAIP^{WT}$ suppressed the accumulation of slow Figure 8s to a similar extent in the presence and absence of BRCA1 (lanes 19-30), indicating that BRCA1 is not needed to support TRAIP function.

Notably, we have observed that TRAIP is co-depleted with other proteins (data not shown), suggesting it interacts non-specifically with different antibodies.

g, Mock- and TRAIP-depleted egg extracts supplemented with His_6-SUMO-rTRAIP^{WT} or His_6-SUMO-rTRAIP$^{\Delta PIP}$, used in replication reaction shown in Fig. 2c, were blotted for TRAIP (top) or the His_6-tag (bottom). Black arrowheads, TRAIP-specific bands. His_6-SUMO-rTRAIP co-migrates with a non-specific band in the TRAIP blot. His_6-SUMO-rTRAIP$^{\Delta PIP}$ is not detectable by the TRAIP antibody because it lacks the C-terminal epitope used to generate the antibody. Blotting for the N-terminal His_6 tag detected both forms of rTRAIP. Non-specifically detected proteins are marked with asterisks.

Extended Data Fig. 4

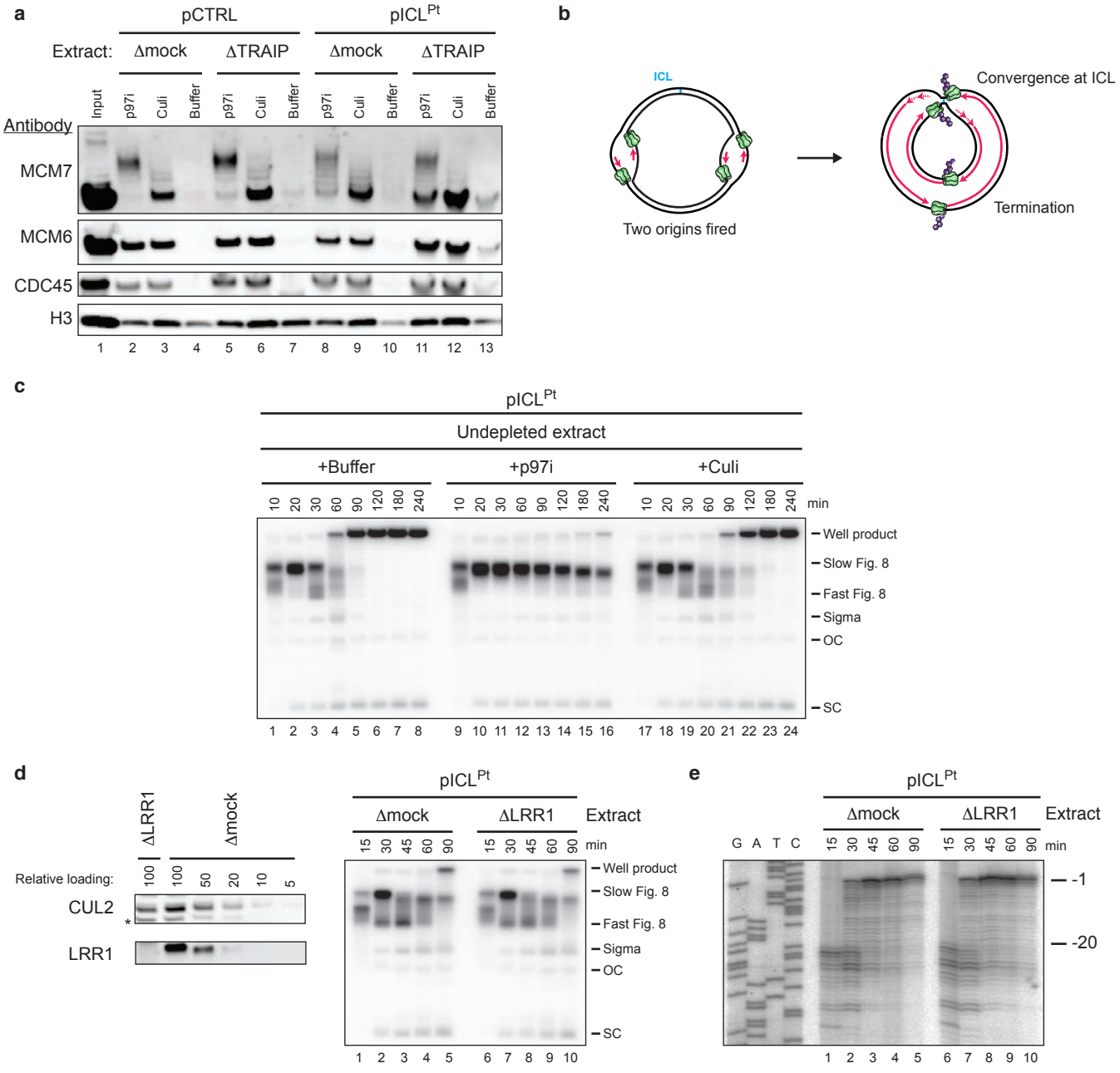

Extended Data Fig. 4 | TRAIP and CRL2^{LRR1} promote distinct CMG unloading pathways

a, To determine whether TRAIP is required for CMG unloading during replication termination, we analyzed proteins associated with pICL^{Pt} or pCTRL 60 min after replication initiation in mock- or TRAIP-depleted extracts containing p97i or Culi, as indicated. Chromatin was recovered and blotted for the indicated proteins. In the absence of TRAIP, CMG unloading from pICL^{Pt} was inhibited compared to the mock-depleted control (compare lanes 10 and 13), as shown in Fig. 1c. In contrast, CMG unloading from pCTRL was unaffected by TRAIP depletion (compare lanes 4 and 7). Similarly, in the presence of p97i, TRAIP was not required for MCM7 ubiquitylation on pCTRL (compare lanes 2 and 5), while it was essential for efficient MCM7 ubiquitylation on pICL^{Pt} (compare lanes 8 and 11, note the greater level of unmodified MCM7 in lane 11). The residual MCM7 ubiquitylation observed on pICL^{Pt} in the absence of TRAIP was likely the result of termination events that occurred elsewhere on the plasmid (see **b**).

b, If two origins fire on a single plasmid, one pair of replication forks converges at the ICL and undergoes TRAIP-dependent CMG unloading whereas a second pair undergoes normal replication termination where CMG unloading depends on CRL2^{LRR1}. Both pairs of CMGs (green) should undergo ubiquitylation (purple).

c, pICL^{Pt} was replicated in extract with p97i or Culi and analyzed as in Fig. 1b. Culi had no significant effect on the accumulation of fast Figure 8 structures, consistent with CRL2^{LRR1} being dispensable for CMG unloading at ICLs.

d, Left, to assess the effect of LRR1 depletion on CMG unloading, NPE was immunodepleted of LRR1, loaded alongside a dilution series of mock-depleted NPE, and blotted for LRR1 and CUL2. A relative loading amount of 100 corresponds to 2 µl of NPE. Non-specifically detected protein is marked with an asterisk. Right, pICL^{Pt} was replicated in mock- or LRR1-depleted egg extracts and

analyzed as in Fig. 1b. The absence of LRR1 had no effect on the formation of fast Figure 8 structures, supporting the idea that $CRL2^{LRR1}$ is dispensable for CMG unloading at ICLs.

e, Nascent strand analysis of $pICL^{Pt}$ replicating in mock- or LRR1-depleted extracts was performed as in Extended Data Fig. 2e. The CMG footprint disappeared with normal kinetics at the ICL in LRR1-depleted egg extract, consistent with $CRL2^{LRR1}$ not being required for CMG unloading at ICLs.

Extended Data Fig. 5

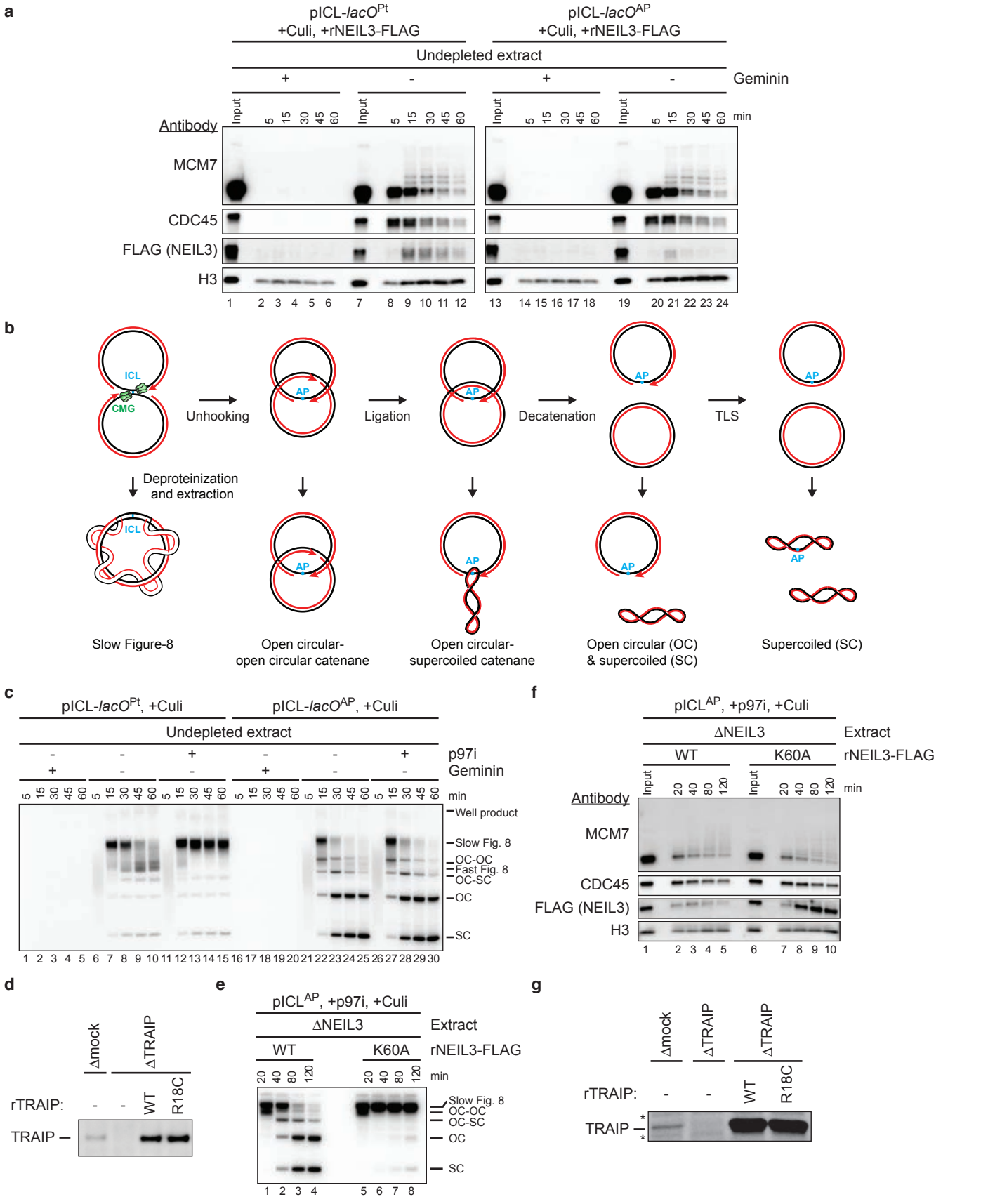

Extended Data Fig. 5 | AP-ICL repair by NEIL3 in *Xenopus* egg extracts

a, Analysis of chromatin-associated proteins during replication of pICL-*lacO*^{Pt} or pICL-*lacO*^{AP} in the indicated extract. At different times after replication initiation, chromatin was recovered and blotted for the indicated proteins.

b, Intermediates generated during replication-coupled repair of an AP-ICL. Top, progression through the NEIL3 repair pathway generates intermediates resulting from fork convergence, NEIL3-dependent *N*-glycosyl bond cleavage, nascent strand ligation, decatenation, and translesion synthesis (TLS). Bottom, deproteinization of the DNA intermediates depicted along the top yields DNA structures that travel with characteristic mobilities during native gel electrophoresis, as indicated alongside of the gel in Fig. 3a.

c, pICL-*lacO*^{Pt} and pICL-*lacO*^{AP} were replicated in extract supplemented with geminin, p97i, and Culi and analyzed as in Fig. 1b.

d and g, The extracts used in the replication reactions shown in Fig. 3, a (**d**) and c (**g**), were blotted for TRAIP. Non-specifically detected proteins are marked with asterisks. The lack of non-specific bands in **d** may be due to shorter incubation with the TRAIP antibody

e, pICL^{AP} was replicated with NEIL3-depleted extract supplemented with rNEIL3^{WT} or rNEIL3^{K60A}, p97i, and Culi, as indicated, and analyzed as in Fig. 1b. OC, open circular; SC, supercoiled.

f, Analysis of proteins associated with pICL^{AP} during replication with NEIL3-depleted extract supplemented with rNEIL3^{WT} or rNEIL3^{K60A}, p97i, and Culi. At the indicated times after replication initiation, chromatin was recovered and blotted for the indicated proteins. Consistent with NEIL3 dissociating rapidly after unhooking, catalytically inactive rNEIL3 (rNEIL3^{K60A}; **e**), was recovered more efficiently with pICL^{AP} than rNEIL3^{WT}.

Extended Data Fig. 6

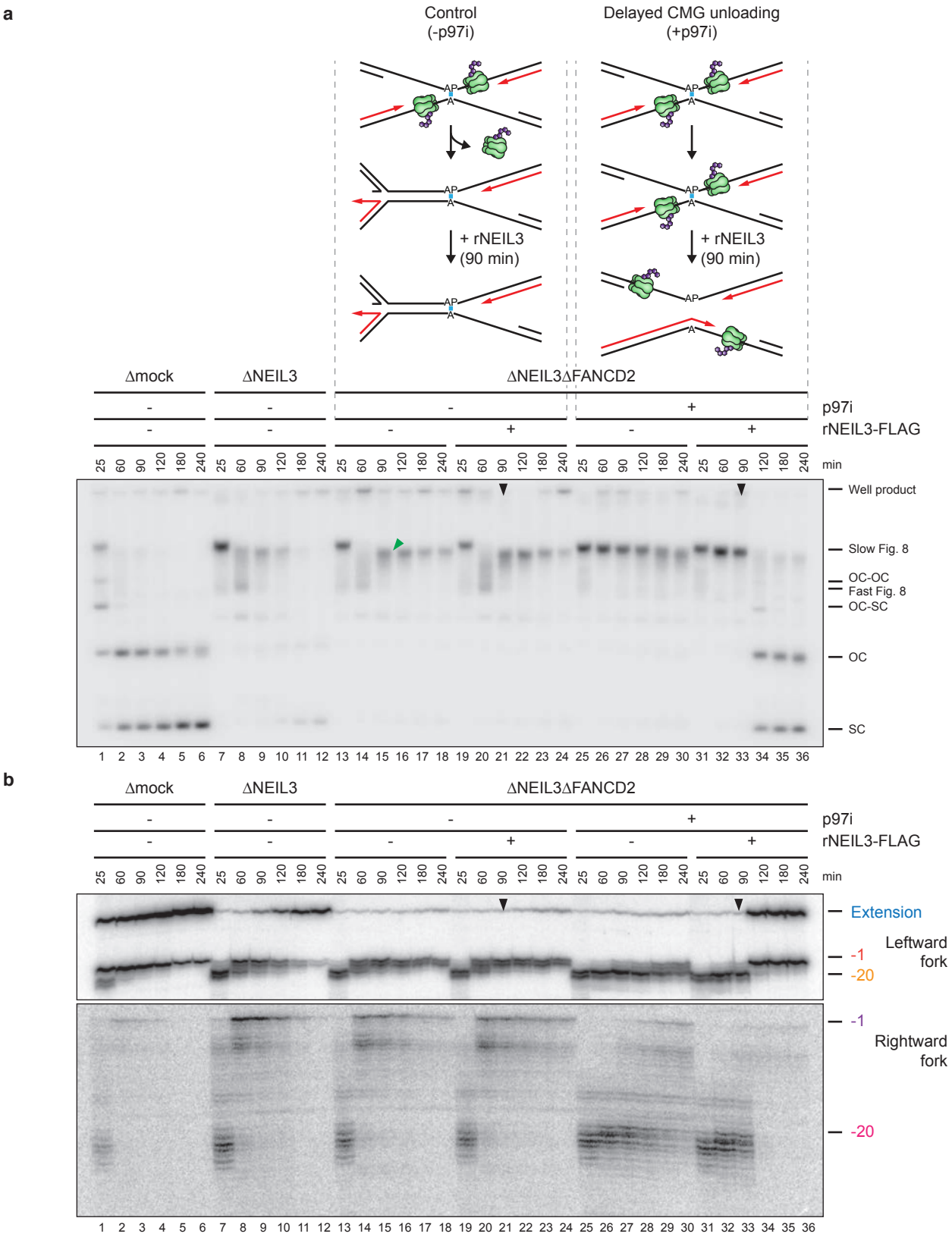

Extended Data Fig. 6 | ICL repair by NEIL3 requires CMG association with chromatin

If NEIL3 activity is coupled to ubiquitylated CMG, NEIL3 should only function before CMG has been unloaded. To test this prediction, we depleted egg extracts of NEIL3 and FANCD2 to block all unhooking events. At a late timepoint, we added back rNEIL3 to extract where CMG had previously been allowed to unload (-p97i), or extract where CMG unloading was prevented (+p97i). Our model predicts that rNEIL3 should function only in the latter setting.

a, Top, schematic illustrating late addition of rNEIL3 to NEIL3- and FANCD2-depleted egg extracts in the absence (left) or presence (right) of p97i. Bottom, replication of $pICL^{AP}$ in mock-, NEIL3-, or NEIL3- and FANCD2- depleted extracts in the presence of [α-^{32}P]dATP. Extracts were supplemented with p97i as indicated and rNEIL3 was added at 90 min as indicated (black arrowheads). Replication intermediates were resolved and visualized as in Fig. 1b. Depletion of NEIL3 and FANCD2 blocked all unhooking of the AP-ICL, resulting in an accumulation of reversed forks (lane 15, green arrowhead). Addition of rNEIL3 at 90 min. in the absence of p97i (after CMG unloading) failed to induce unhooking, based on the persistence of the reversed forks (lanes 21-24). In contrast, when CMG unloading was prevented with p97i (lanes 25-30; note the persistence of slow Figure 8 intermediates), late rNEIL3 addition led to efficient ICL unhooking, as seen from the rapid conversion of slow Figure 8s to open circular and supercoiled species (lanes 34-36).

b, To confirm the presence or absence CMG at the AP-ICL, DNA was recovered from the reactions described in **a** and subjected to nascent strand analysis as in Extended Data Fig. 2e. Top, extension products and nascent strands of the leftward fork. Bottom, nascent strands of the rightward fork. Black arrowheads, rNEIL3 addition. Depletion of NEIL3 and FANCD2 did not affect loss of the CMG footprint at -20 and caused persistence of nascent DNA strands at -1 (lanes 13-24), indicative

of failure to unhook the ICL. Late addition of NEIL3 failed to stimulate further nascent strand extension (lanes 21-24), indicating that unhooking did not occur. Treatment with p97i caused persistence of the CMG footprint at -20 (lanes 25-30), consistent with a retention of CMG at the ICL, and late addition of NEIL3 stimulated formation of full-length nascent strand extension products (lanes 34-36), indicative of efficient unhooking. Taken together, the data in **a** and **b** strongly suggest that NEIL3 activity is coupled to the presence of CMG at the site of the ICL, although we cannot rule out that NEIL3 activity is suppressed by downstream events, such as fork reversal, that depend on CMG unloading.

Extended Data Fig. 7

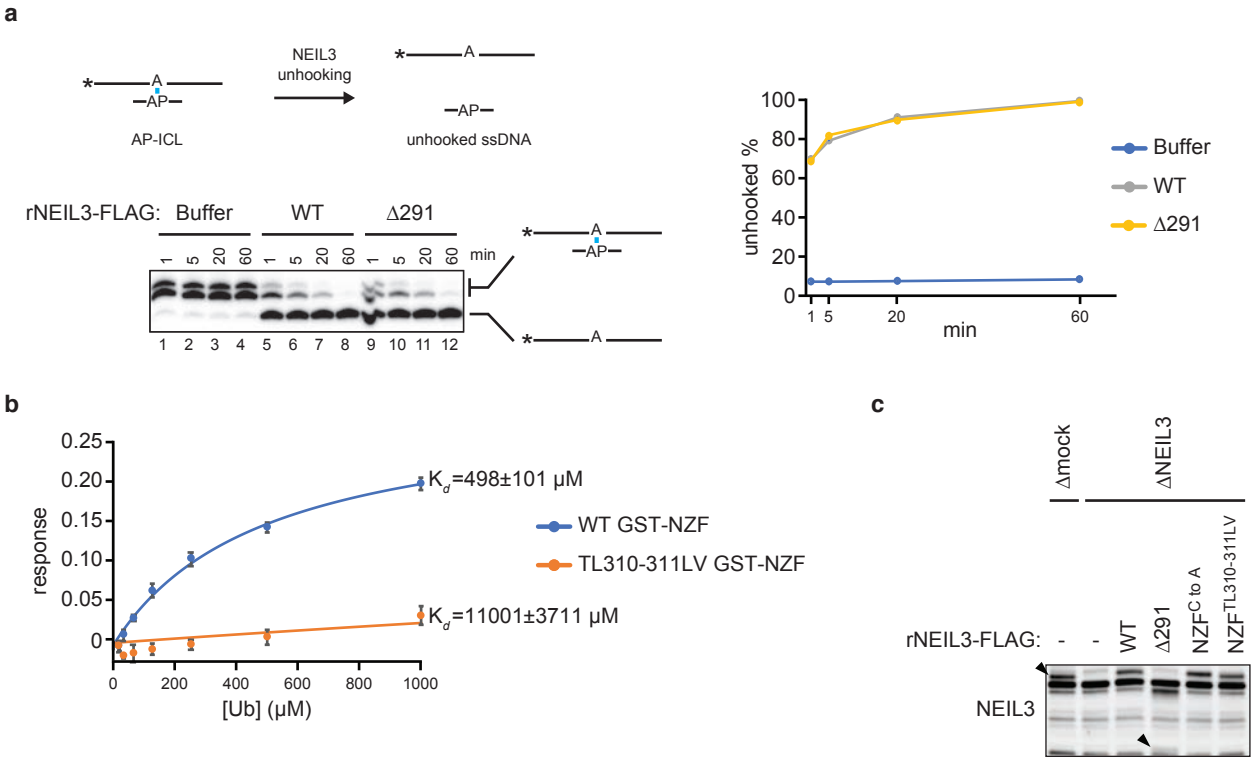

Extended Data Fig. 7 | The NZF domain of NEIL3 contributes to ubiquitin binding but not catalysis

a, Left, to determine whether rNEIL3$^{\Delta 291}$ is catalytically active, a model AP-ICL substrate comprising a synthetic 5'-radiolabeled 24mer oligonucleotide cross-linked to a ~3mer was mixed with rNEIL3$^{\Delta 291}$ or rNEIL3^{WT}. Cross-linked and unhooked species were resolved by denaturing polyacrylamide gel electrophoresis and visualized by autoradiography. Asterisks indicate the ^{32}P radiolabel. Note that the cross-linked species migrates as a doublet due to heterogeneity in the bottom strand following RNase digestion (see Methods for details). Right, quantification of unhooking. Equivalent results were obtained in three independent experiments, which show that rNEIL3$^{\Delta 291}$ retains full activity.

b, Interaction of the NEIL3 NPL4-type zinc finger (NZF; residues 300 to 328) with ubiquitin. GST-NEIL3 NZF fusion protein (WT or TL,LV substituted) was immobilized on a biosensor tip and monoubiquitin binding was measured by biolayer interferometry (BLI). The ubiquitin binding response was corrected for non-specific binding to GST and plotted as a function of ubiquitin concentration. Error bars represent standard error of the mean from three independent experiments.

c, Mock- and NEIL3-depleted extracts supplemented with wild-type or substituted rNEIL3, used in the replication reactions shown in Fig. 3e, were blotted for NEIL3. Black arrowheads, NEIL3-specific bands. rNEIL3$^{\Delta 291}$ is not efficiently detected by the NEIL3-specific primary antibody.

Extended Data Fig. 8

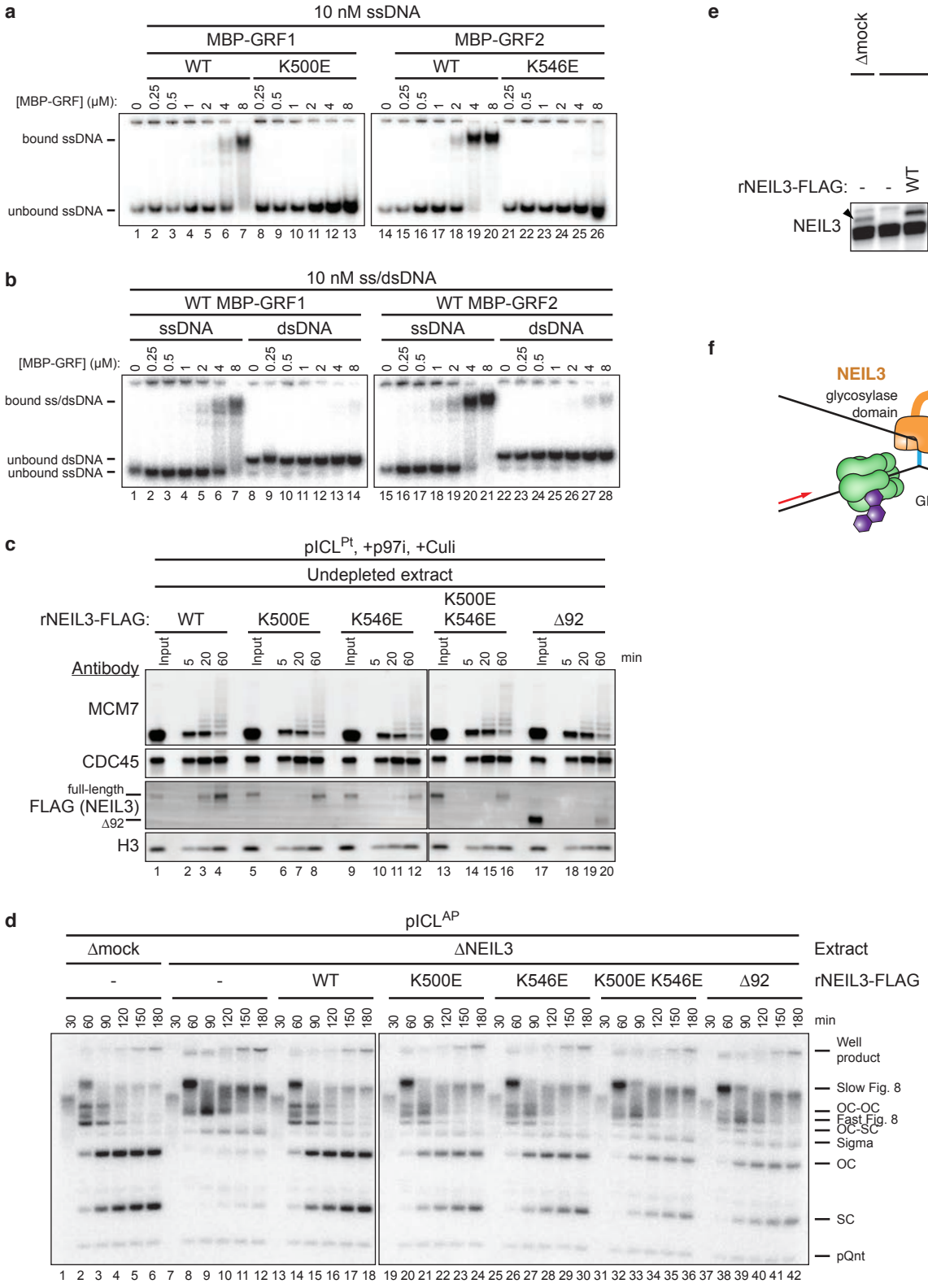

Extended Data Fig. 8 | The GRF domains of NEIL3 mediate interactions with ssDNA at the replication fork

a and b, To test whether the two GRF zinc fingers in NEIL3 interact with ssDNA, we expressed each individually and performed electrophoretic mobility shift assays. rMBP-NEIL3 GRF zinc finger fusion proteins (wild-type or substituted) were incubated with 5'-radiolabeled 25-mer ssDNA or dsDNA. Bound and unbound DNAs were resolved by native polyacrylamide gel electrophoresis and visualized by autoradiography. This analysis reveals that both GRF domains bind specifically to ssDNA.

c, Analysis of proteins associated with $pICL^{Pt}$ during replication in the presence of p97i and Culi. Extracts were supplemented with wild-type or substituted rNEIL3. At different times, chromatin was recovered and blotted for the indicated proteins. The individual GRF substitutions modestly affected recovery of rNEIL3 upon pICL pull-down while combination of the substitutions or deletion of both GRF zinc fingers strongly reduced rNEIL3 recovery, indicating that interactions mediated by the GRF zinc fingers promote recruitment of NEIL3 to an ICL.

d, $pICL^{AP}$ was replicated in mock- or NEIL3-depleted extracts supplemented with wild-type or mutated NEIL3 as indicated and analyzed as in Fig. 1b. pQnt, undamaged control plasmid. Relative to $rNEIL3^{WT}$, rNEIL3 with substitutions in either GRF zinc finger that abolish ssDNA binding (K500E and K546E) exhibited modest defects in $pICL^{AP}$ unhooking that were exacerbated when the substitutions were combined, indicating that interactions between the GRF zinc fingers and ssDNA contribute to ICL repair.

e, Mock- and NEIL3-depleted extracts supplemented with wild-type or substituted rNEIL3, used in the replication reactions shown in **d**, were blotted for NEIL3.

f, Model for recruitment of NEIL3 to chromatin by zinc finger-mediated interactions. Upon replication fork convergence at an ICL, TRAIP-dependent CMG ubiquitylation recruits NEIL3 through direct interactions between NEIL3's NZF domain and ubiquitin. Association of NEIL3 with chromatin is further enhanced by interactions between the tandem GRF zinc fingers and single stranded DNA, possibly on the lagging strand template.

Extended Data Fig. 9

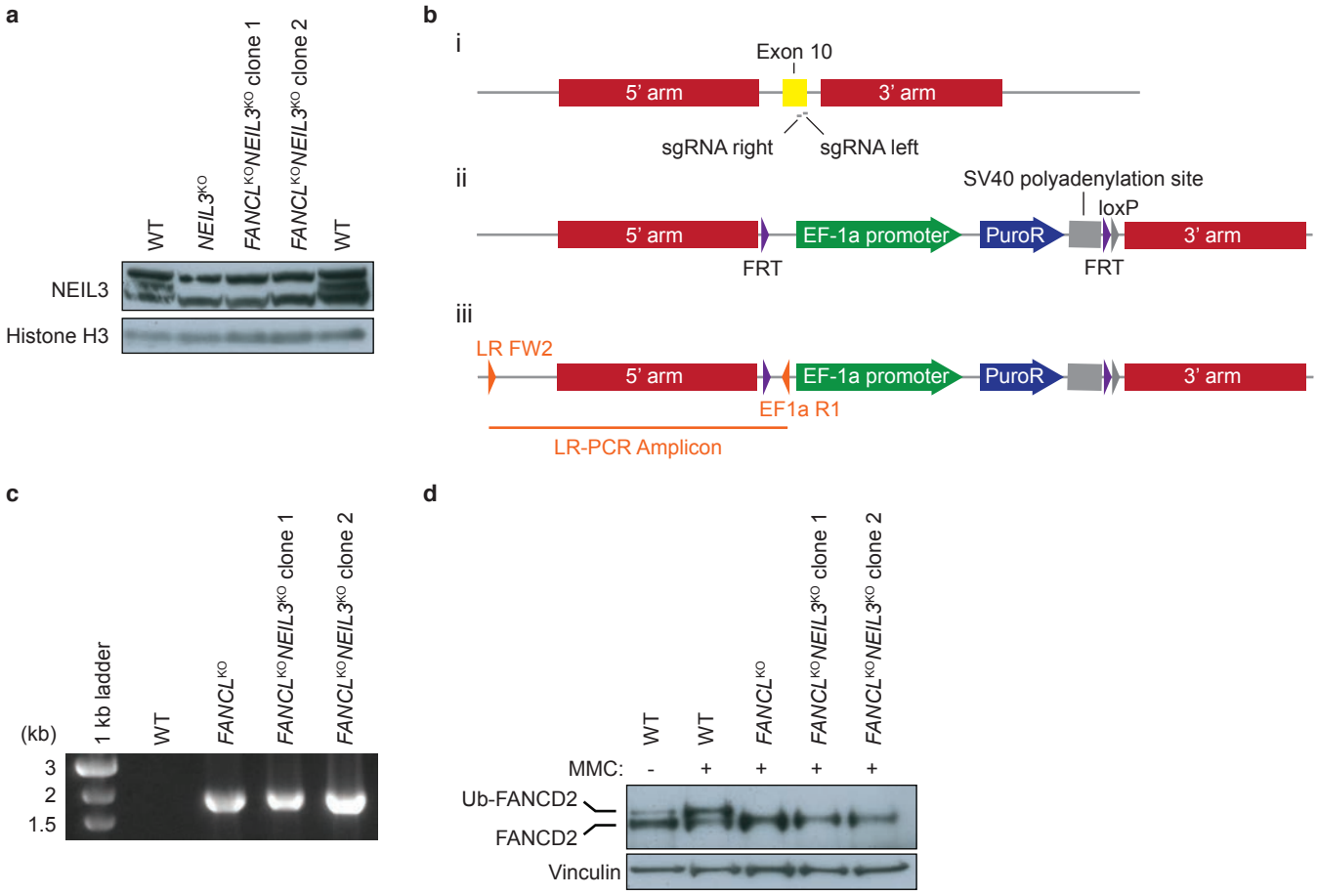

Extended Data Fig. 9 | CRISPR targeting and validation of HAP1 cells

a, Immunoblot analysis of NEIL3 expression in wild-type, *NEIL3*, and *FANCL*/*NEIL3* knockout HAP1 cell lines. Histone H3 was detected as a loading control.

b, Schematic of *FANCL* CRISPR targeting. (i) Human *FANCL* exon 10, sgRNA binding sites, and homology arm targets, (ii) *FANCL*-Puro targeting construct with homology arms flanking exon 10, (iii) Targeted *FANCL* allele with integrated puromycin resistance cassette.

c, Detection of the integrated puromycin resistance cassette in HAP1 cells by *FANCL* long-range PCR.

d, Analysis of FANCD2 ubiquitylation in mitomycin C (MMC)-treated wild-type, *FANCL*, and *FANCL*/*NEIL3* knockout HAP1 cell lines to confirm *FANCL* knockout. Vinculin was detected as a loading control. FANCL is the catalytic subunit of the FA core complex, which ubiquitylates FANCD2.

Extended Data Fig. 10

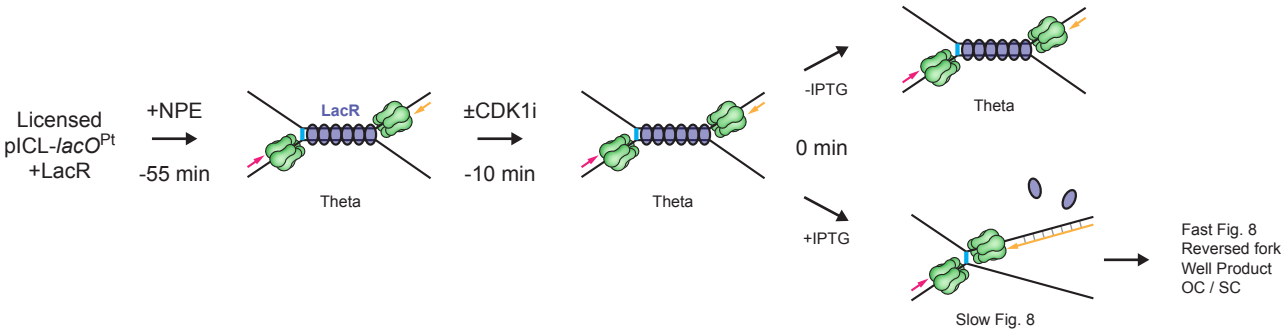

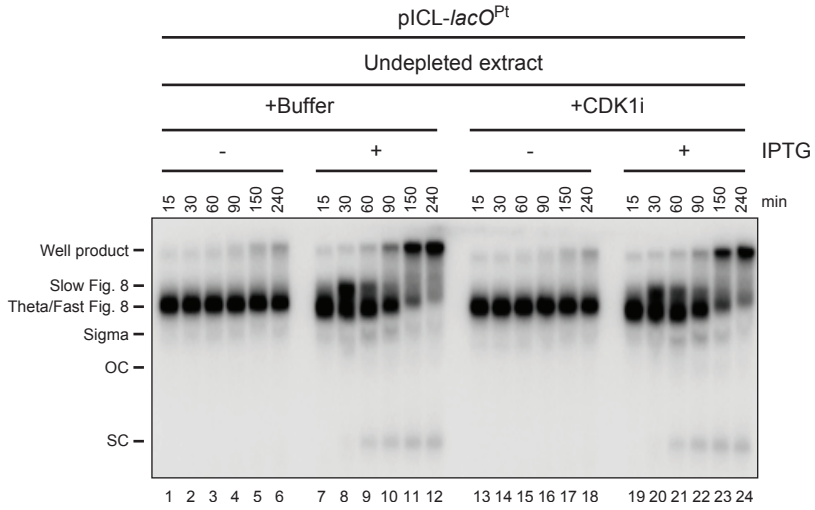

Extended Data Fig. 10 | ICL repair does not require M-CDK

In interphase egg extracts, TRAIP travels with DNA replication forks but ubiquitylates CMGs only when forks converge. In the presence of mitotic cyclin-dependent kinase (M-CDK), TRAIP is activated in the absence of fork convergence (Deng et al., *submitted*). We therefore wanted to know whether TRAIP-dependent CMG unloading in interphase egg extract depends on residual M-CDK activity. Top, the reaction scheme. Replication of pICL-*lacO*^{Pt} with a pre-assembled LacR array was initiated at -55 min. Forty-five min after initiation (-10 min), reactions were supplemented with buffer or the CDK1 inhibitor RO-3306 (CDK1i) and allowed to incubate for an additional 10 min. The LacR array was then released with addition of IPTG to trigger fork convergence and ICL repair (0 min). In a control, we added buffer instead of IPTG to retain the LacR array. CDK1i was added late to avoid inhibition of replication initiation. Bottom, at the indicated times after IPTG addition, samples were collected and analyzed as in Fig. 1B. Fork stalling at the boundaries of the LacR array leads to a theta structure. The conversion of theta to slow Figure 8, fast Figure 8 (co-migrating with theta), and well product in the presence of CDK1i implies that M-CDK is not required for CMG unloading or ICL repair. This demonstrates that TRAIP activation at ICLs does not depend on residual M-CDK activity. Therefore, TRAIP activation at converged forks and in mitosis are mechanistically distinct.

References:

40 Walter, J., Sun, L. & Newport, J. Regulated chromosomal DNA replication in the absence of a nucleus. *Mol Cell* **1**, 519-529 (1998).

41 Klein Douwel, D. *et al.* XPF-ERCC1 acts in Unhooking DNA interstrand crosslinks in cooperation with FANCD2 and FANCP/SLX4. *Mol Cell* **54**, 460-471, doi:10.1016/j.molcel.2014.03.015 (2014).

42 Fu, Y. V. *et al.* Selective Bypass of a Lagging Strand Roadblock by the Eukaryotic Replicative DNA Helicase. *Cell* **146**, 931-941, doi:10.1016/j.cell.2011.07.045 (2011).

Supplementary Table 1 | Oligonucleotide Sequences

Oligonucleotides for preparation of plCLs	
Name	Sequence (Cross-linked positions are indicated in bold)
Pt_Top	CCCTCTTCC**G**CTCTTCTTTC
Pt_Bottom	GCACGAAAGAAGA**G**CGGAAG
AP_Top	CCCTCTTCCGCTC**dU**TCTTTC
AP_Bottom	GCACGAAAG**A**AGAGCGGAAG

Oligonucleotides for preparation of AP-ICL glycosylase assay substrates	
Name	Sequence (Cross-linked positions are indicated in bold)
AP_assay_A	GCCATAGTAAG**A**AGAGCCGAATGC
AP_assay_B	rGrCrArUrUrCrGrGrCrUC**dU**TrCrUrUrArCrUrArUrGrGrC

Oligonucleotides for preparation of EMSA assay substrates	
Name	Sequence
EMSA_Top	AGACCGTGCCAGCCTAAATTTCAAT
EMSA_Bottom	ATTGAAATTTAGGCTGGCACGGTCT

Primer for preparation of Sequencing Ladder	
Name	Sequence
pICL_Seq	CATGTTTTACTAGCCAGATTTTTCCTCCTCTCCTG

Primers for preparation of Expression Vectors	
Name	Sequence
NEIL3_291_A	GCGCGCGGAATTCACCATGGTGGAGGGTCCGGGCTG
NEIL3_291_B	CCAGCCCTCGAGCGTCTACTTGTCGTCATCGTCTTTGTAGTCCCATCCAATAAGGCTATT
NEIL3_NZF_A	CTGGAAGTTCTGTTCCAGGG
NEIL3_NZF_B	TCACCGAAACGCGCGAGGCAGATCGTCAGTCAGTCACGATCTATGGTCTCAGAGTAAGAC
GST_A	ATCGTGACTGACTGACGATC
GST_B	CCCAGTGCTCTTCTTTGGGCCCCTGGAACAGAACTTCCAGATCCGATTTTGGAGGATGGT
GRFZF1_A	ACTGGTAACCCACAGTGCAG
GRFZF1_B	TCACCGAAACGCGCGAGGCAGATCGTCAGTCAGTCACGAT
GRFZF2_A	TTGCATTTCCCATTCTGCAA
GRFZF2_B	TCACCGAAACGCGCGAGGCAGATCGTCAGTCAGTCACGAT
MBP_A	ATGGGTTCTTCTCACCATCA
MBP_B	CACATGGAACATTGTGTGCACTGCACTGTGGGTTACCAGT
MBP_C	CAATACACCGTTTCCCATGGTTGCAGAATGGGAAATGCAA
pGEX_A	ATCGTGACTGACTGACGATC
pGEX_B	TAGAAGAACCATGGTGATGGTGATGGTGAGAAGAACCCATGAATACTGTTTCCTGTGTGA
TRAIP_A	ATTAGTACTGGATCCATGCCCATACGCGCCTACTGTACG
TRAIP_B	TCGTAGTAATGGATCCTTATTTCAAGAAGTCTTCGAGCCTGGGCTGG
R18C_A	ACACGTATTGTCGAAGAAGTCCGAGCAAATCGTAC
R18C_B	GATGTGGCCGCGATTACCTGTGGGC
PIP_A	GTTGGCAAGTGAGGAAGTACAAGCTGTG
PIP_B	TAAGGATCCGAGCTCCTCGAGTAATAAGCTTG

CRISPR Guide Sequences	
Name	Sequence
FANCL_left	CCTAATGCAATTCTGCGTGCTGT
FANCL_right	TTTTTCTGGCTCAAGTACCCAGG

Primers for PCR Clonal Analysis	
Name	Sequence
FANCL_LR_FW2	TGTCTACCCCCTAAGTTCGTTGA
EF1a_R1	GCGATCTCTGGGTTCTACGTTAGTG